CHAPTER-4

RESULTS AND DISCUSSIONS

This chapter contains results pertaining.

(a) Characterization of collected industrial wastewater.

(b) Characterization of the synthesized undoped, Fe doped and I doped TiO_2 nanoparticles (photocatalysts).

(c) Kinetic studies of photocatalytic degradation of dye (Direct Blue 199) with different light sources and photocatalytic reactors.

(d) Regeneration of used photocatalysts and determination of their activities.

(e) Comparison among undoped, Fe doped/I doped TiO_2 and P-25.

4.1 Characterization of wastewater

The collected industrial wastewater was characterized by the procedure given in section 3.2.1.1 to 3.2.1.7 and results are presented in Table 4.1.

Table 4.1 Characterization of wastewater*

Testing parameters	**Value of parameter (before treatment)**
pH	7.5
Conductivity	853 milli Siemens(ms/m)
λ_{max}	594 nm
BOD_5 at 20ºC	361 mg/l
COD	649 mg/l
Total dissolved solids	371mg/l
Total suspended solids	237mg/l
Temperature	31.2ºC
Dye content	221.6 ppm
Appearance	Blue

*The above parameters were investigated before applying any treatment on the wastewater except concentration of dye; it was calculated after the filtration with filter paper.

To know the functional group which were present in the industrial wastewater, FTIR of wastewater was done. The FTIR spectrum of the dye-loaded wastewater (Direct Blue 199) is shown in Fig 4.1. The absorption peaks at 3472.3, 2945.4, and 1577.6 cm^{-1} represent the –NH–NH_2– stretch, C–H stretch, and –N=N– stretch, respectively (Sreeja et al. 2013). The absorption peak at 1396.5 cm^{-1} reflects the alkane C–H deformation. Two absorption peaks at 1343.7 and 617.8 cm^{-1} represent the S=O and C–S stretching, respectively, and indicate that dye has a sulfur-containing compound. The peaks at 1577.6, 1136.4, and 617.8 cm^{-1} confirm the existence of the –SO_3Na group in the dye structure (Jadhav et al. 2012). The last peak of FTIR spectrum at 461.2 cm^{-1} reflects the Cu–N stretch of the dye compound.

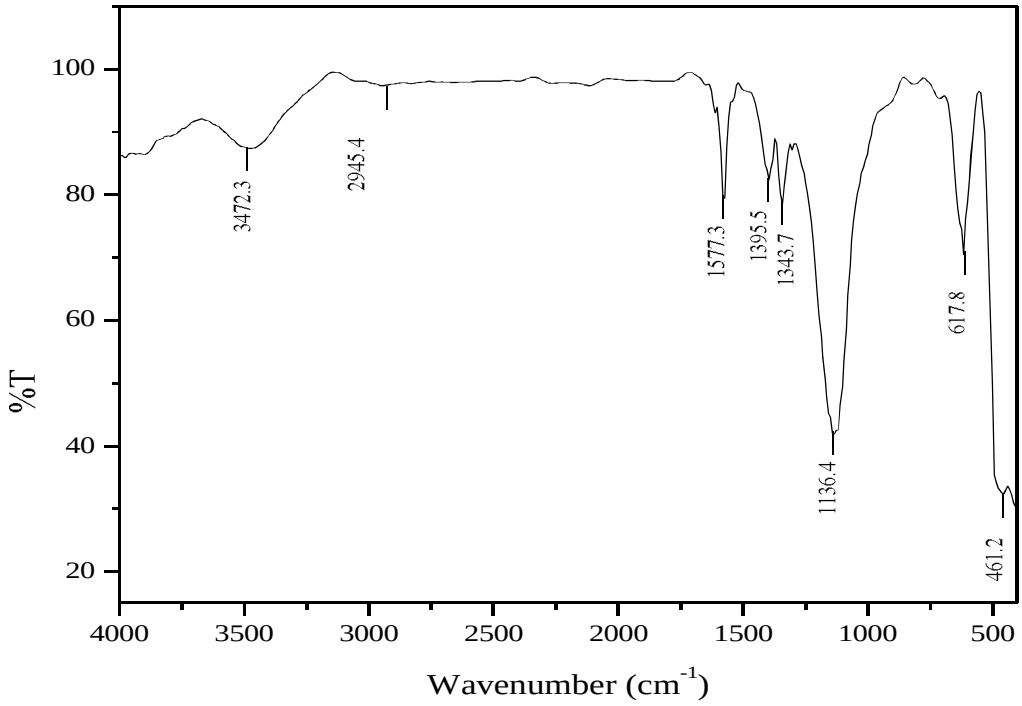

Fig 4.1 FT-IR analysis of collected wastewater.

Fe DOPED TiO_2

4.2 Characterization of Fe doped TiO_2 photocatalysts

Fe doped TiO_2 catalysts were prepared as per procedure given in section 3.2.3.1 to 3.2.4.1. These were characterized by XRD, DRS, FTIR, XPS, HR-TEM and EDX. The results and discussion are given below.

4.2.1 X-Ray Diffraction Analysis (XRD)

The phases and crystal structure of various undoped and Fe doped TiO_2 photocatalysts were determined by XRD analysis, which are shown in Figure 4.2. The XRD peaks show that the synthesized nanoparticles have only the anatase phase of TiO_2 with the tetragonal crystal structure (JCPDS number 21-1272). The anatase phase of TiO_2 has longer e^-/h^+ life than the rutile phase, which makes it more suitable for a charge carrier to participate in surface reactions (Luttrell et al.

2014). In the XRD analysis, no peaks of iron or iron compound was found at any concentration of Fe doping in TiO_2, which indicates that Fe^{3+} ions are successfully incorporated into the TiO_2 lattice without formation of iron oxide on the TiO_2 surface because Ti^{4+} and Fe^{3+} have approximately similar ionic radii (0.68 and 0.64 Å, respectively). Nasralla et al. (2013) reported the incorporation of Fe^{3+} ions into the TiO_2 lattice without formation of any other phase of TiO_2 except anatase in the synthesis of Fe-doped TiO_2 nanoparticles.

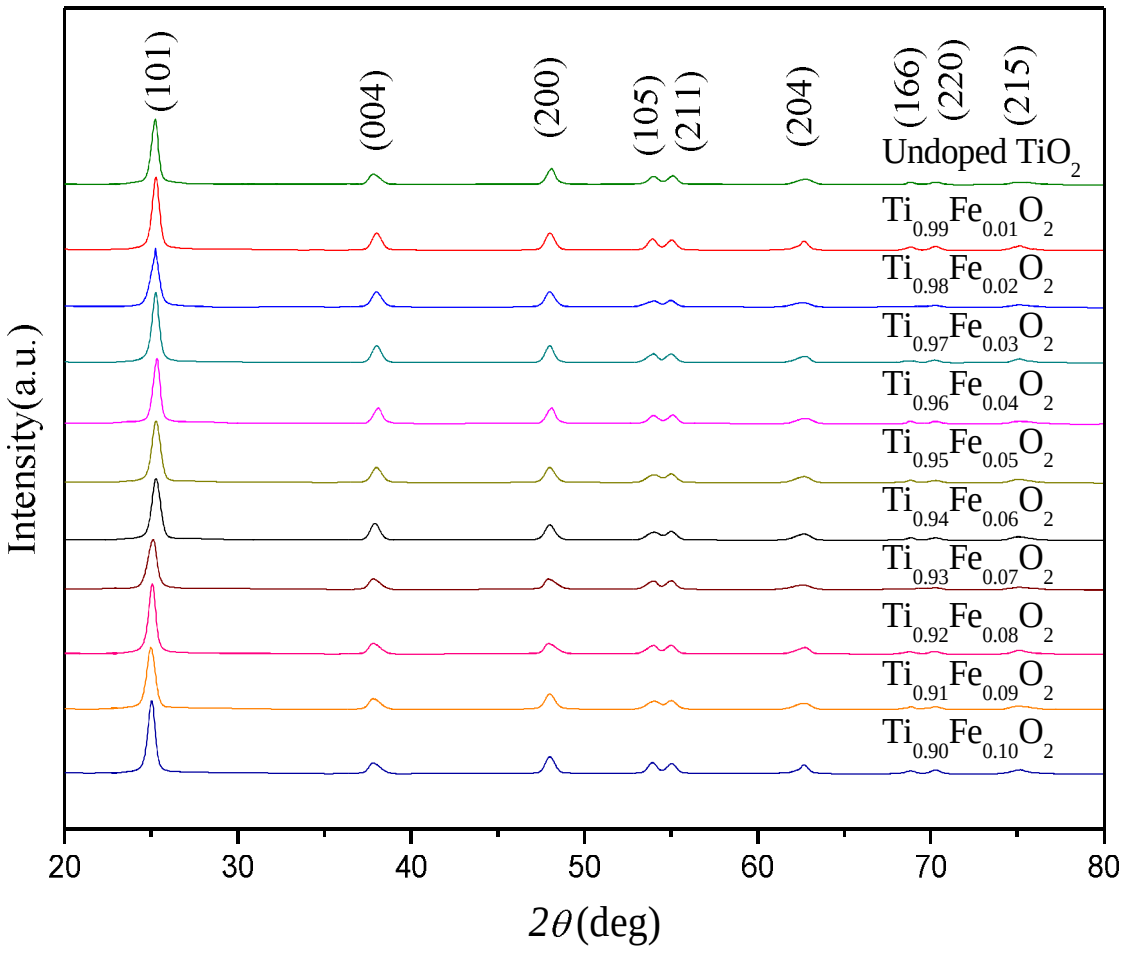

Fig 4.2. The XRD pattern of undoped and Fe doped (1-10%) TiO_2 photocatalyst.

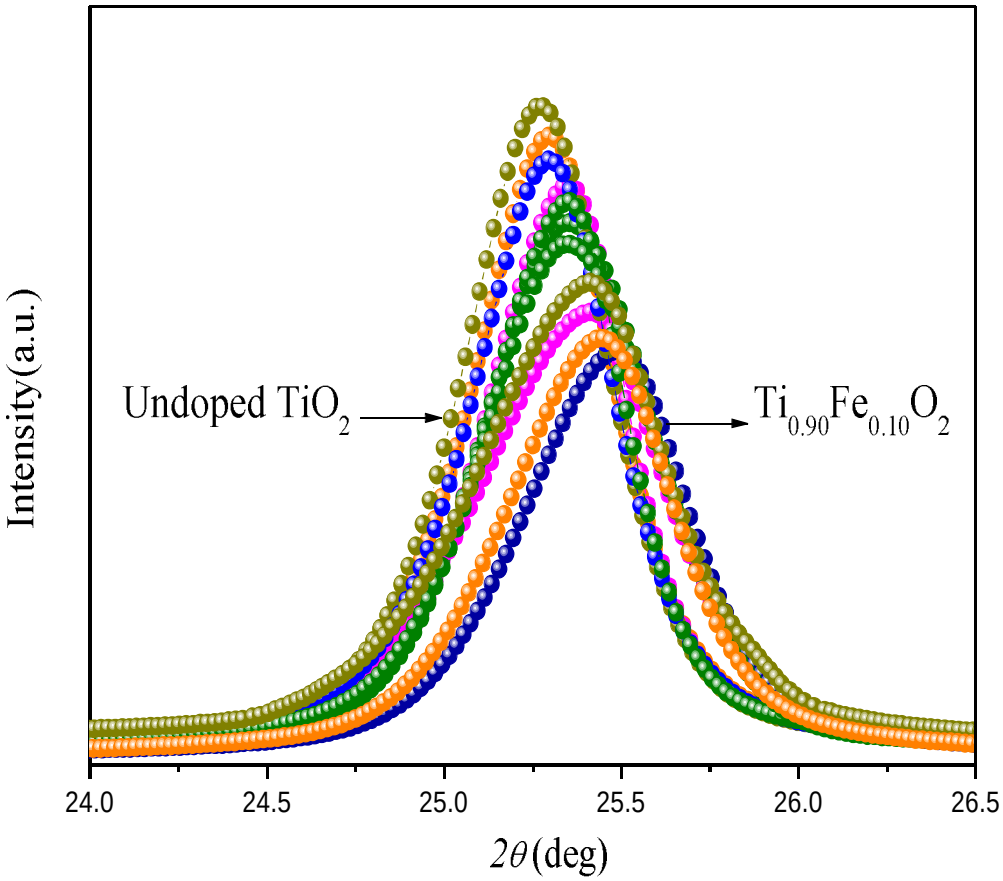

Fig 4.3. The intensity variation of the peak (101) and shifting of angle with doping.

From Fig 4.3, it was observed that with increasing the Fe concentration in TiO_2, the main peak (101) shifts toward the higher 2θ value with decrease in interplanar spacing. The main cause behind the peak shifting and reduction in interplanar spacing is the substitution of ions (Fe^{3+} for Ti^{4+}) because substitution of Fe^{3+} for Ti^{4+} creates oxygen vacancies (to maintain charge neutrality) that reduces interplanar spacing by increasing the 2θ value. Chaudhuri et al. (2012) reported the peak shifting (101) toward the higher 2θ value and reduction in interplanar spacing of synthesized Fe-doped TiO_2 in the XRD analysis. It is generally believed that crystallinity of a sample depends on the intensity of diffraction peaks. Fig 4.3 shows that the incorporation of Fe^{3+} at the Ti^{4+} site in TiO_2 will lead to a local disorder in

the crystal lattice of the TiO_2, which gives rise to relatively broader peaks in the doped compound than the undoped TiO_2. Li et al. (2008) studied the effects of Fe doping on TiO_2 and reported the decrease in crystallinity due to the Fe^{3+} ions. Fig 4.4 represents the variation of particles size with the Fe concentration.

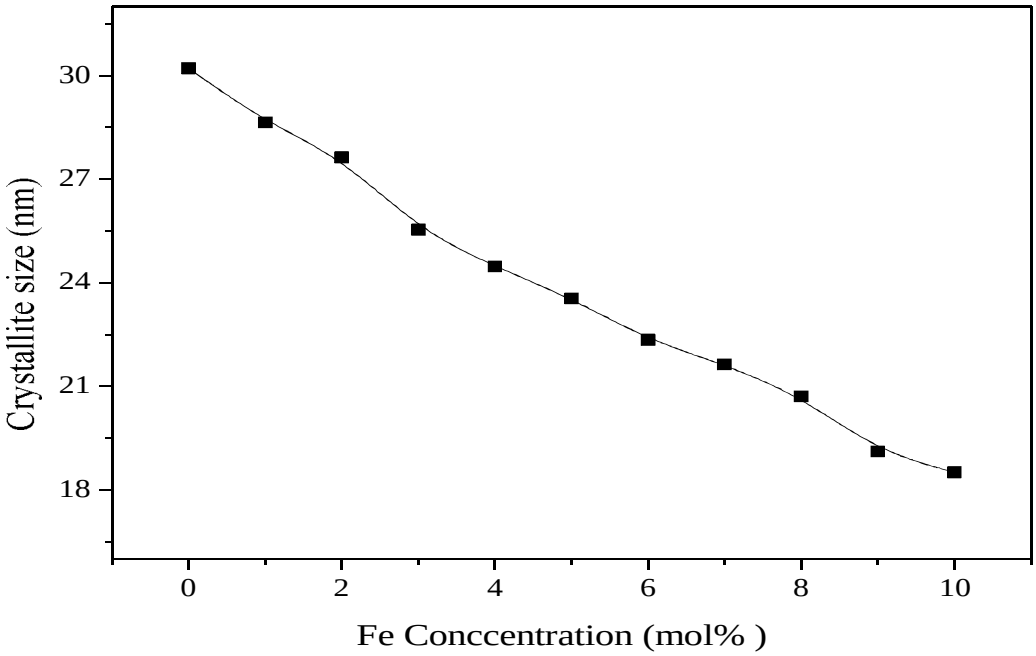

Fig 4.4. Effect of Fe concentration on crystallite size.

The average particle size of synthesized photocatalysts was calculated using Scherrer's formula (equation 3.4). Fig 4.4 indicates that the crystallite size of the photocatalyst decreases with increasing doping concentration because substitution of Fe^{3+} for Ti^{4+} distorts the lattice of the TiO_2, which restrained the crystal growth during heat treatment of Fe-doped TiO_2 photocatalyst. The synthesized photocatalysts have lower crystal size, which indicates that these have higher absorption of solar radiation for photoexcitation (Wu et al. 2015). Wen et al. (2012) reported that the Fe doping in TiO_2 restricts the crystal growth during the heat treatment. Yu et al. (2002) reported the addition of additives to TiO_2 and found that

additives obstruct the contact between TiO_2 particles because additives had a suppressive effect on the crystal growth that hinders the crystal growth during heat treatment.

4.2.2 UV-Vis Diffuse Reflectance Spectroscopy (DRS)

The DRS analysis of undoped and Fe doped TiO_2 photocatalysts were done to determine their band gap energy and these are shown in Fig 4.5 and Fig 4.6. The spectra of undoped and Fe doped TiO_2 was recorded in the range of 200-800 nm and shown in Fig 4.5. It was found that Fe doping in TiO_2 shifts its absorption band toward visible region. With the help of absorbance and wavelength data, the indirect band gap energies of undoped TiO_2 and Fe doped TiO_2 photocatalysts were determined from the $[F(R_\alpha)h\nu]^{1/2}$ *vs.* $h\nu$ plot and shown in Fig 4.6. The symbol $F(R_\alpha)$ is known as Kubelka-Munk function and can be known from the following equation (3.5).

$$F(R_\alpha) = (1 - R_\alpha)^2/2\, R_\alpha \qquad (3.5)$$

Where $R_\alpha = 10^{-A}$ is the reflectance coefficient of the sample and A is the absorbance of the corresponding samples.

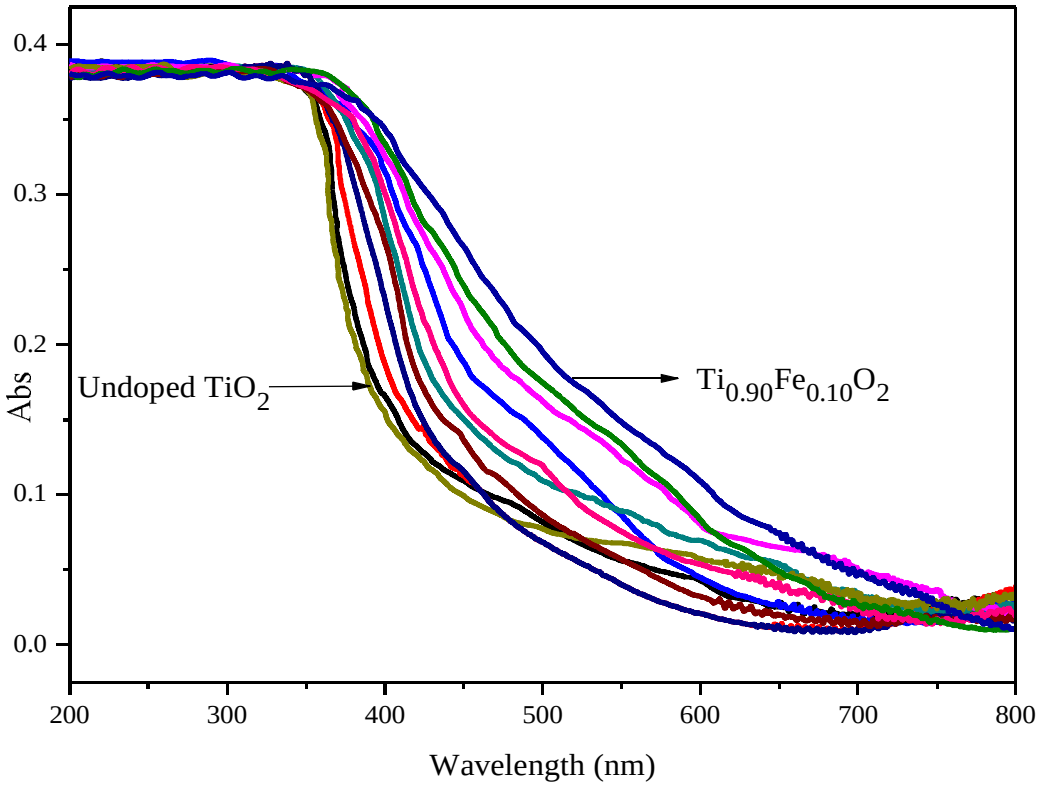

Fig 4.5. The UV-Vis diffuse spectra undoped and (1-10% Fe doped TiO_2).

The band gap energy of Fe doped TiO_2 photocatalysts are shifted to lower band gap energy side with increasing the Fe concentration in TiO_2 as shown in Fig 4.7. The band gap energy of prepared nanoparticles reduced from 3.19 to 2.0 eV. The band gap reduction is reported earlier, also with iron doping in TiO_2 (Li et al. 2008).

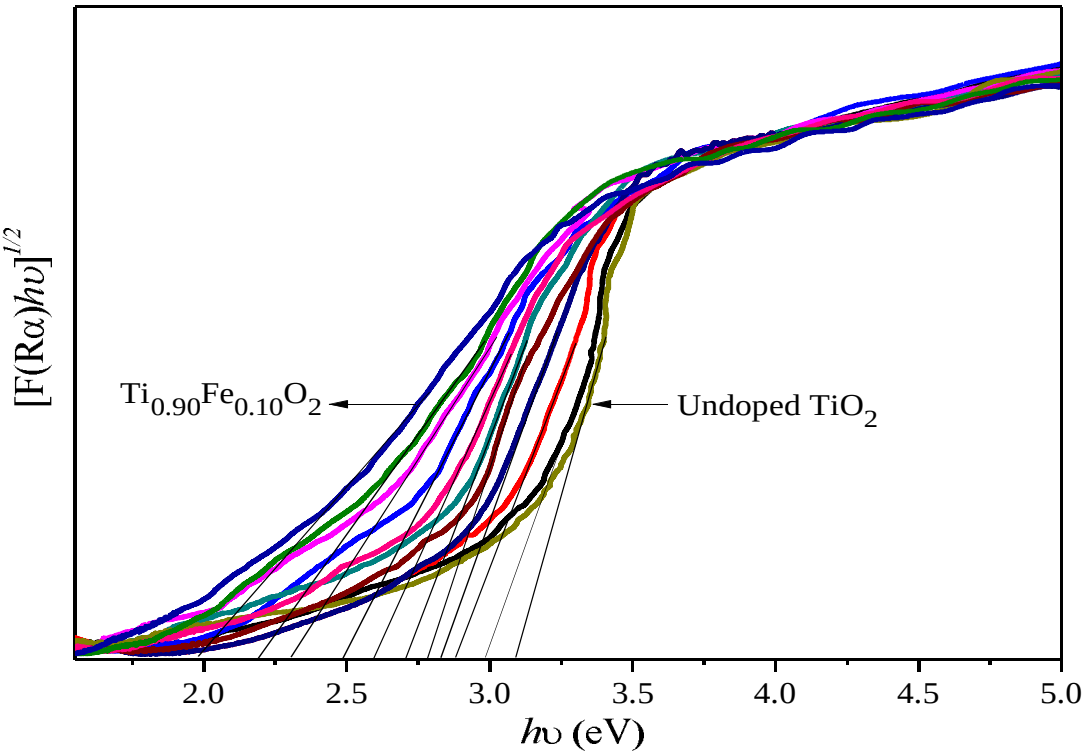

Fig 4.6. The plots of $[F(R\alpha)h\upsilon]^{1/2}$ vs. photon energy.

A significant shifting of absorption band from UV to the visible region was also achieved with doping of other metal ions such as V, Cr, Mn, Co, Ni, and Cu, etc. in TiO_2 structure (Anpo 1997; Anpo et al. 1998, 1999; Bougarrani et al. 2018). The transition of electrons from Fe 3d orbitals to TiO_2 conduction band is the main cause of the band gap shifting. The Fe^{3+} doping in TiO_2 introduces novel energy level (Fe^{3+}/Fe^{4+}) without modifying the TiO_2 valance band edge position which facilitate the electron transition from the Fe energy level (Fe^{3+}/Fe^{4+}) to the conduction band of TiO_2. The colour of photocatalysts changed from white to yellow with increase of the % Fe doping in TiO_2, similar to previous study (Cam Loc et al. 2010).

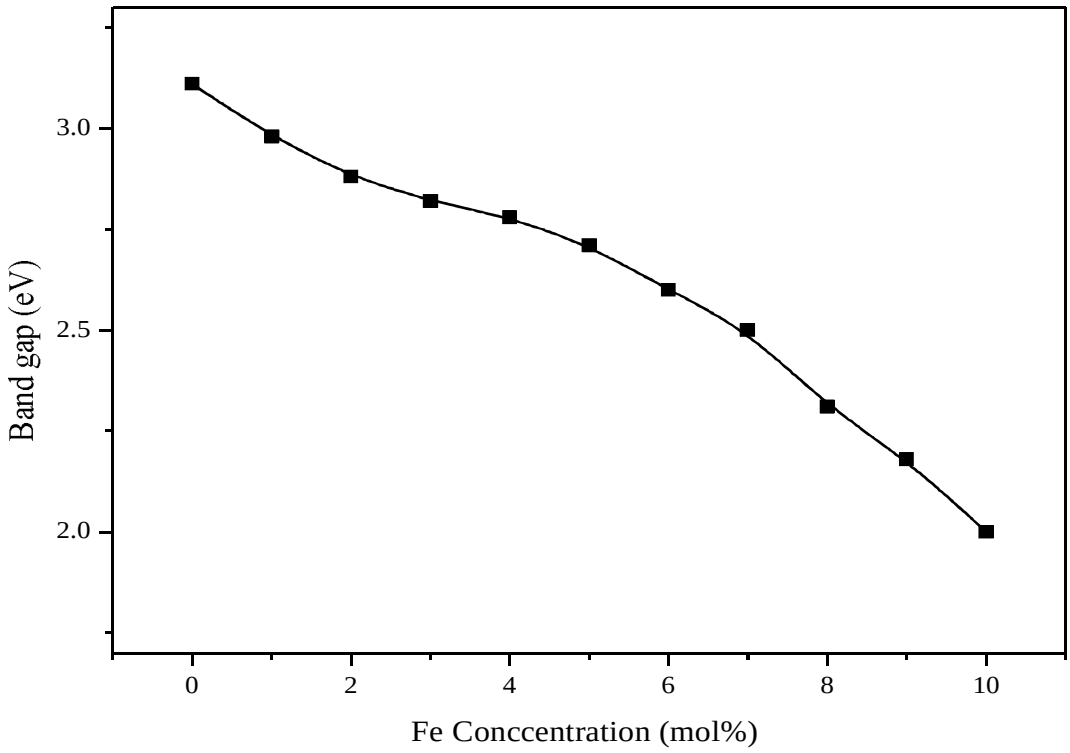

Fig 4.7. Variation of band gap energy with Fe concentration.

4.2.3 Fourier Transform Infrared Spectroscopy (FTIR)

The FTIR spectra of undoped and Fe doped TiO_2 photocatalysts are shown in Fig 4.8. The presence of various vibrational bands in undoped and Fe doped TiO_2 were identified by FTIR analysis. The weak transmittance bands between 3400-3150 cm^{-1} and 1650-1450 cm^{-1} represent the stretching vibration of the O-H groups and bending vibration of adsorbed water molecule respectively, which represents the coordination vacancies in the presence of water. The stretching and bending vibrations of O-H are in similar band range (Nagaveni et al. 2004; Lopez et al. 2002). The photocatalytic activity of the synthesized Fe doped TiO_2 nanoparticles may increase by the presence of the hydroxyl group (OH^-) since the OH^- group serves as the main scavenger of the photogenerated charge carrier, which leads to

the formation of a hydroxyl radical ($OH^{\bullet}$) required for the degradation of the dye (Ali et al. 2017).

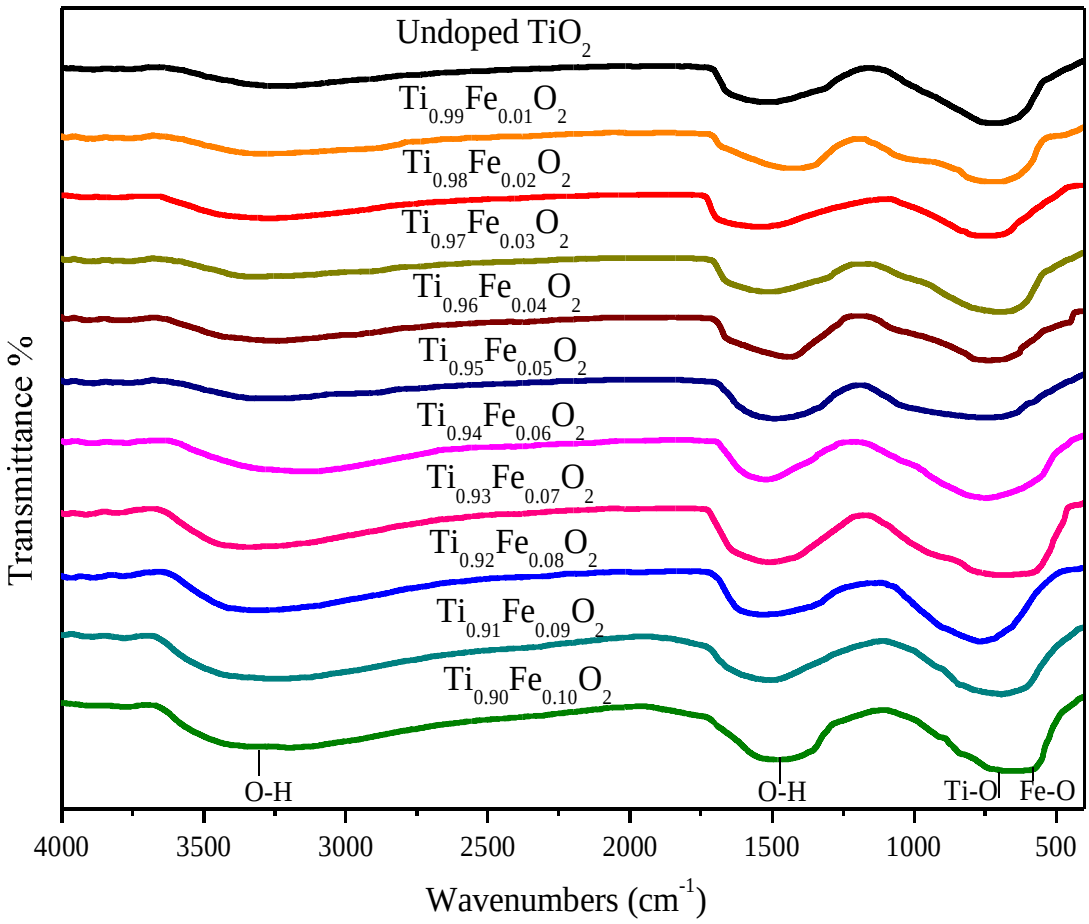

Fig 4.8. The FTIR spectrum of undoped and Fe doped (1-10%) TiO_2 photocatalyst.

In Fig 4.8, the transmittance band between 840-630 cm^{-1} shows Ti-O-Ti stretching, which have important role in enhancement of photocatalytic activity of Fe doped TiO_2 photocatalyst. TiO_2 anatase phase show strong FTIR absorption bands in the regions of 850-650 cm^{-1} (Reddy et al. 2001). The peak at 578 cm^{-1} represent the stretching vibration of Fe-O bond. Santosh et al. (2016) have reported stretching mode of the Fe-O bond at 575 cm^{-1}.

4.2.4 X-Ray Photoelectron Spectroscopy (XPS)

The XPS analysis was used to investigate the binding energies and chemical states of the elements (Ti, O and Fe) in the synthesized Fe doped TiO_2 nanomaterials and these are shown in Fig 4.9 (a-d) and Fig 4.10 (a-d). The XPS spectra are shown only for two best catalysts ($Ti_{0.96}Fe_{0.04}O_2$ and $Ti_{0.95}Fe_{0.05}O_2$) since theses catalysts showed higher activity in the photodegradation process. Fig 4.9 (a) and Fig 4.10 (a) show the wide XPS spectra of $Ti_{0.96}Fe_{0.04}O_2$ and $Ti_{0.95}Fe_{0.05}O_2$ photocatalysts respectively. The both wide XPS spectra of the catalysts reveal that the elements Ti, O, Fe and C are present in the sample. The XPS spectrum of Ti 2p region is shown in Fig 4.9 (b) and 4.10 (b). The peaks found in both spectra at 463.7 eV, 463.9 eV and 458.6 eV, 458.4 eV represent the Ti^{4+} 2p3/2 and Ti^{4+} 2p1/2 binding energy of titanium, however the other single peak in both spectra at 457.9 eV and 457.4 eV indicates the 3+ state of titanium (Zhang et al. 2011). The presence of both peaks (Ti^{4+} and Ti^{3+}) reveal that synthesized photocatalysts have both oxidation state of titania. Fig 4.9 (c) and 4.10 (c) show the O 1s region of the synthesized photocatalysts. XPS spectrum of O 1s region represents two kinds of O 1s peaks namely crystal lattice oxygen peak $O^{2-}_{lattice}$ in Ti-O-Ti and hydroxyl oxygen peak (OH^-) (Ren et al. 2013). The main peak $O^{2-}_{lattice}$ was found at about 529.2 eV and 529.6 eV in both spectra, these can be assigned as a metallic oxide peak. The peaks found in both spectra at 530.5 eV and 530.7 eV can be assigned as the hydroxyl peak (OH^-) resulting mainly from the chemisorbed water whereas the peak at 528.6 eV and 528.9 eV represent the Fe-O-Ti bond. Mathews et al. (2015) synthesized the Fe doped TiO_2 photocatalyst and reported the crystal lattice oxygen peak at 529.6 eV, hydroxyl oxygen peak at 531 eV and Fe-O-Ti at 529.45 eV which

are similar with present study. Theses hydroxyl ions have high tendency to react with other atoms or group to become stable (Xin et al. 2005).

The Fe 2p region of the synthesized photocatalyst is shown in Fig 4.9 (d) and Fig 4.10 (d). The spectra of Fe 2p region in both graph show that the peaks at 710.1 eV, 709.4 eV and 723.3 eV, 723.5 eV represent the 3+ binding energy of iron (Moulder and Chastain 1992) where the weak peak at 720.8 eV and 721.1 eV can be assigned as 2+ binding energy of iron (Xu et al. 2017). The radii of Ti^{4+} (0.68Å) and Fe^{3+} (0.64Å) are almost same so Fe^{3+} can penetrate into the TiO_2 structure and may exist in the form of Fe(III) and Fe-O-Ti within the TiO_2 lattices (Hung et al. 2008), which changes the electron density and acts as electrons-holes traps that creates a differences in electronegativity and enhances the photocatalytic activity of Fe doped TiO_2 photocatalysts (Hung et al. 2008). Khan and Swati (2016) found the both peaks of Fe^{3+} ions (Fe 2p1/2 and Fe 2p3/2) at 710.9 and 724.9 eV at almost same value as in present study.

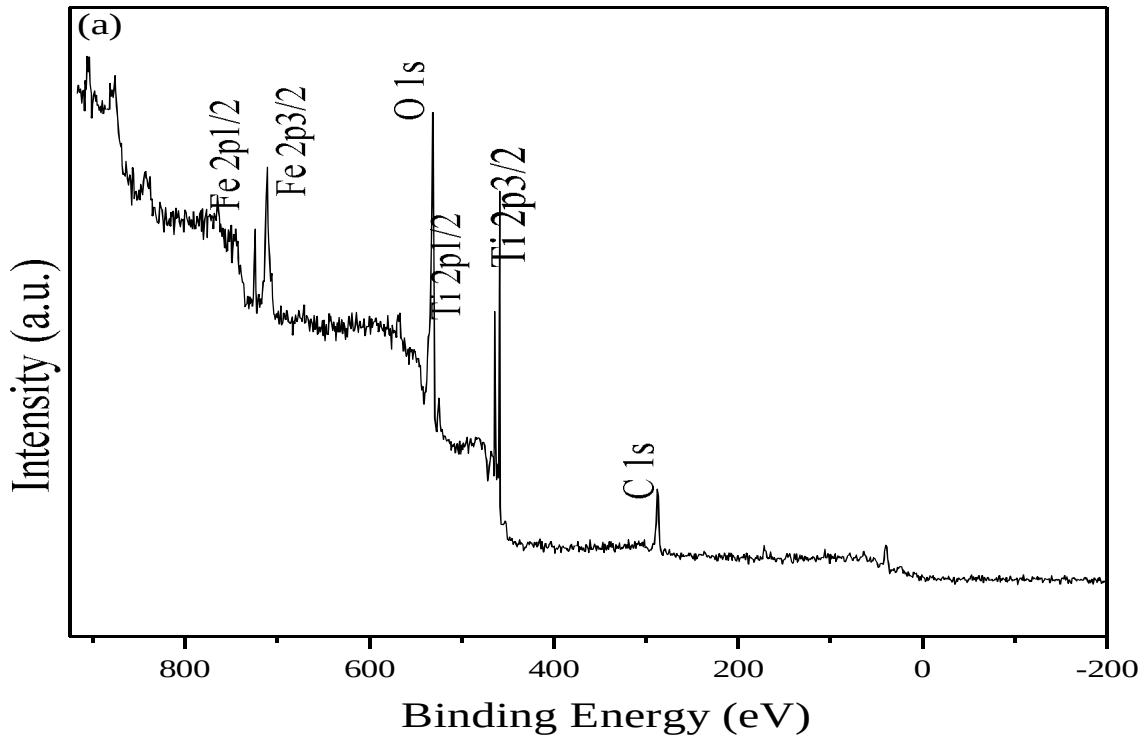
(a)
Fe 2p1/2
Fe 2p3/2
O 1s
Ti 2p1/2
Ti 2p3/2
C 1s
Intensity (a.u.)
800
600
400
200
0
-200
Binding Energy (eV)

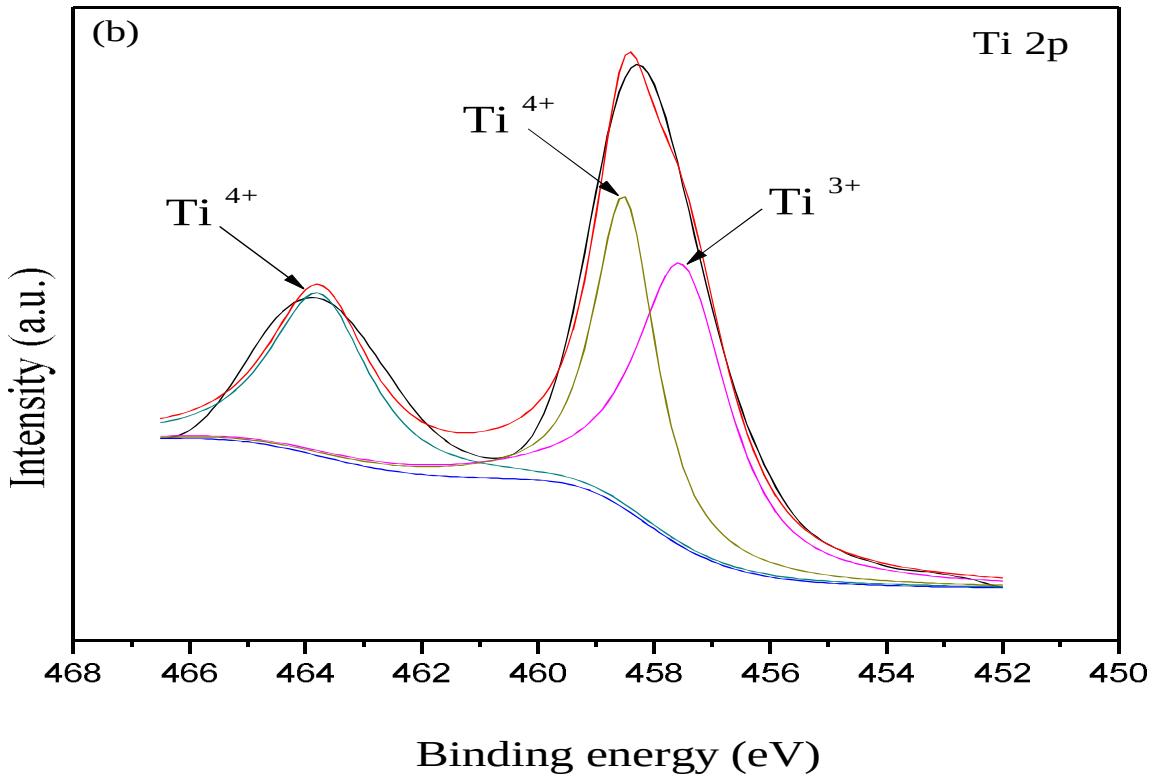
(b)
Ti 2p
Ti 4+
Ti 4+
Ti 3+
Intensity (a.u.)
468
466
464
462
460
458
456
454
452
450
Binding energy (eV)

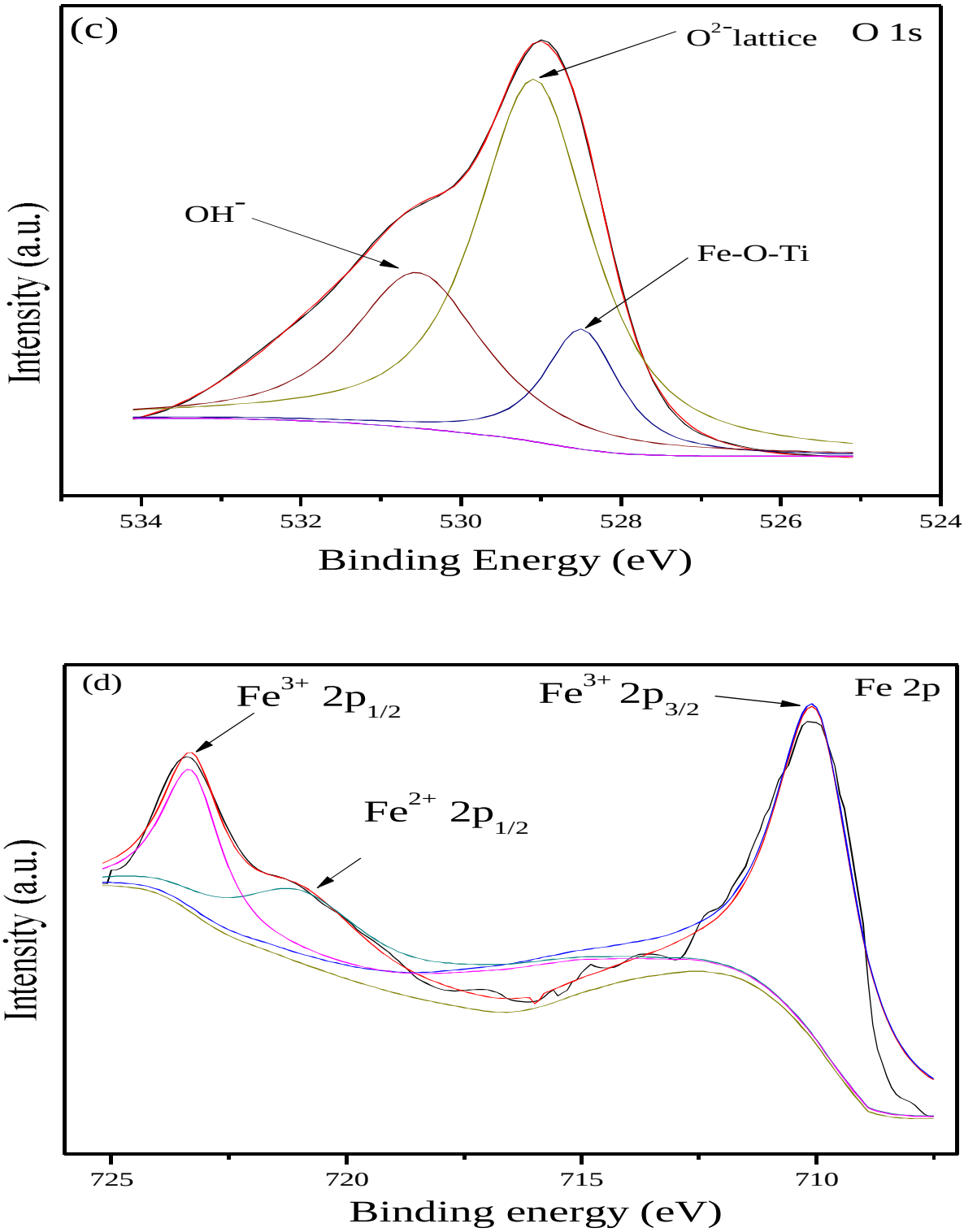

Fig 4.9. The XPS survey spectrum (a) and resolution scan over Ti 2p (b) O 1s (c) and Fe 2p (d) of 4% Fe doped TiO_2 photocatalyst.

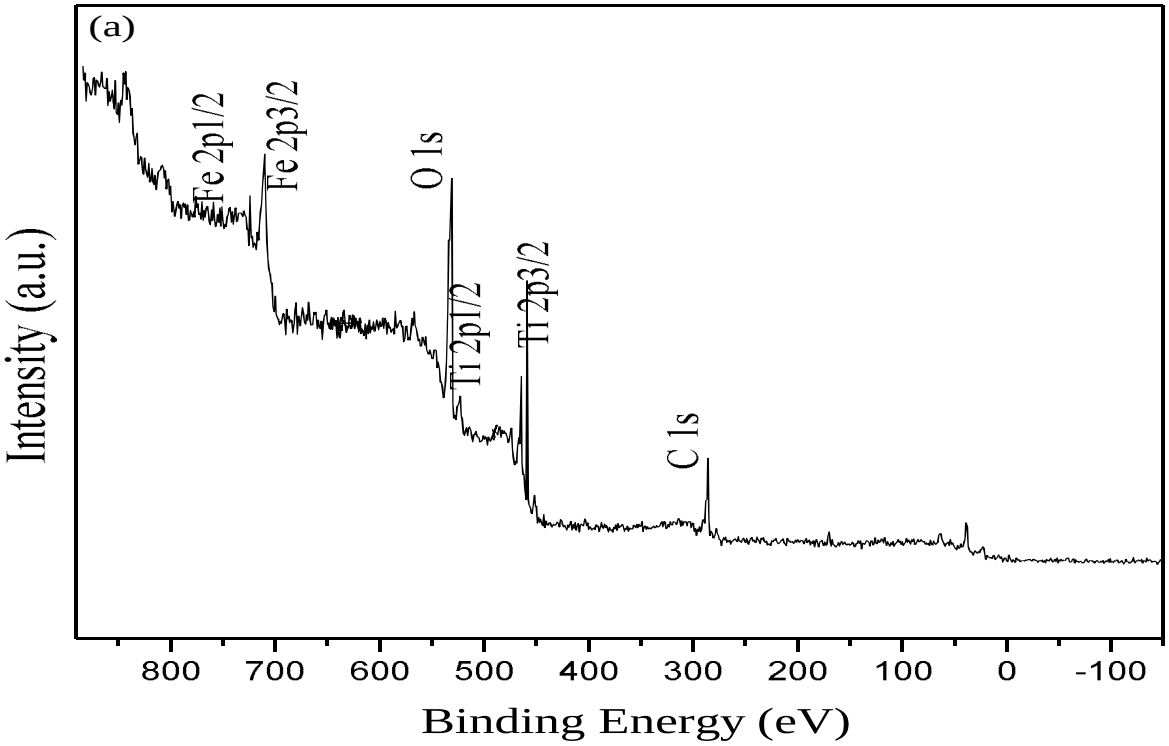
(a)
Fe 2p1/2
Fe 2p3/2
O 1s
Ti 2p1/2
Ti 2p3/2
C 1s
Intensity (a.u.)
800
700
600
500
400
300
200
100
0
-100
Binding Energy (eV)

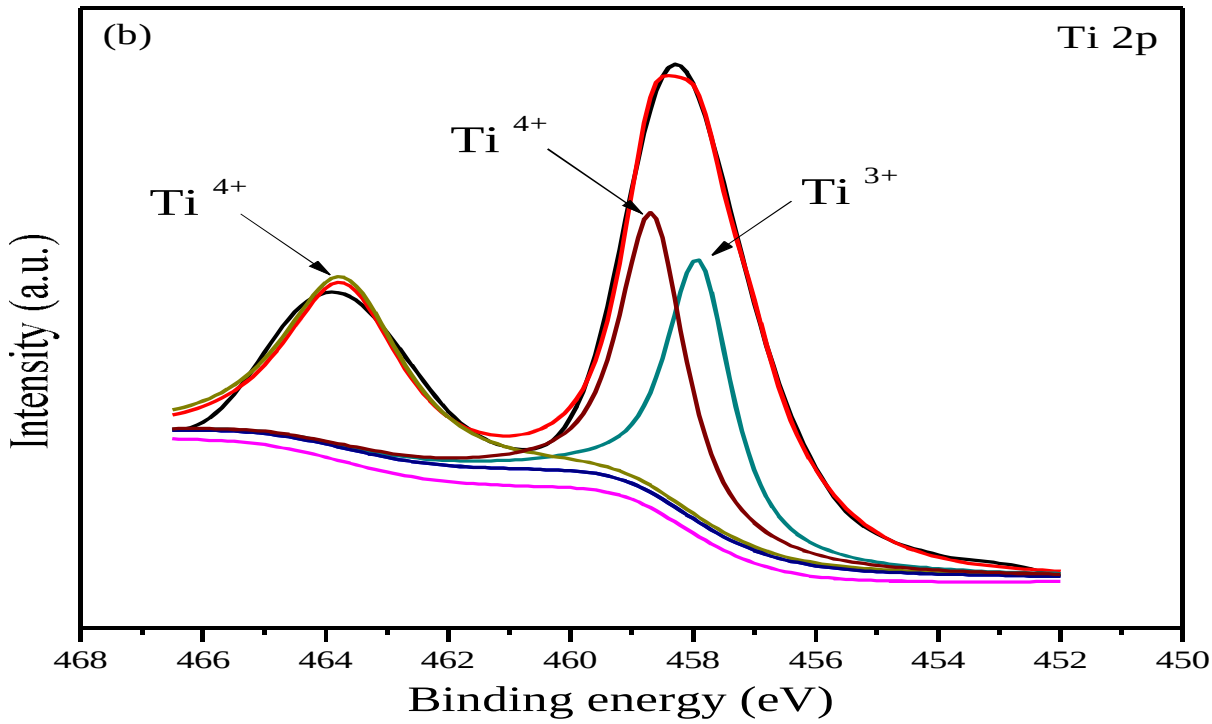
(b)
Ti 2p
Ti 4+
Ti 4+
Ti 3+
Intensity (a.u.)
468
466
464
462
460
458
456
454
452
450
Binding energy (eV)

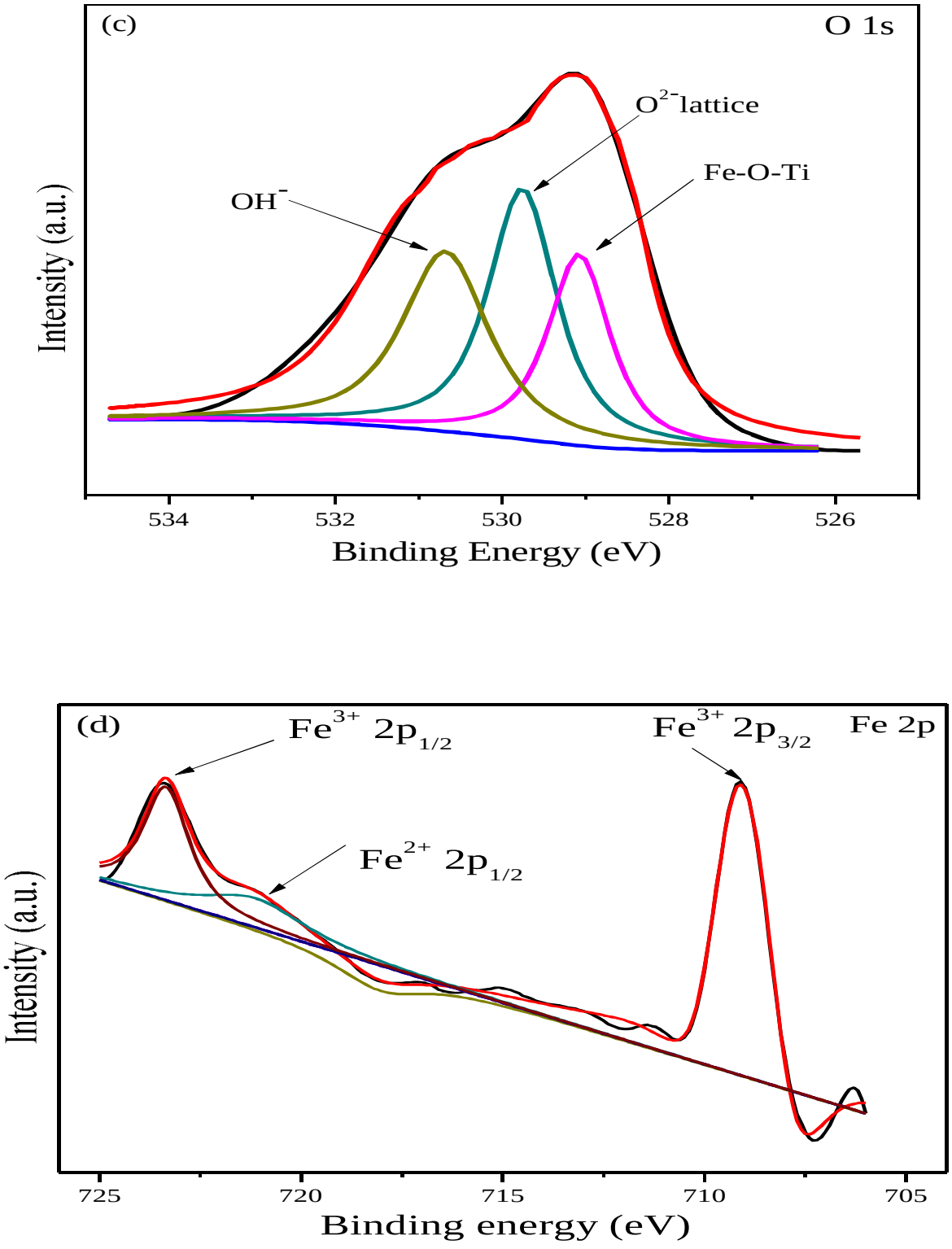

Fig 4.10. The XPS survey spectrum (a) and resolution scan over Ti 2p (b) O 1s (c) and Fe 2p (d) of 5% Fe doped TiO_2 photocatalyst.

4.2.5 Structural morphology

The structural morphology of undoped TiO_2 and $Ti_{0.96}Fe_{0.04}O_2$ photocatalysts was investigated using TEM analysis. The TEM and SAED images of these photocatalysts are shown in Fig 4.11 and Fig 4.12. The images show that the shape of synthesized photocatalysts is spherical. In Fig 4.12, the interplanar spacing (d_{hkl}) of the photocatalyst was measured from the SAED images and the values of interplanar spacing reveal that the both kind of catalysts (undoped and Fe doped TiO_2) have anatase phase which are in agreement with XRD results (JCPDS card number 21-1272).

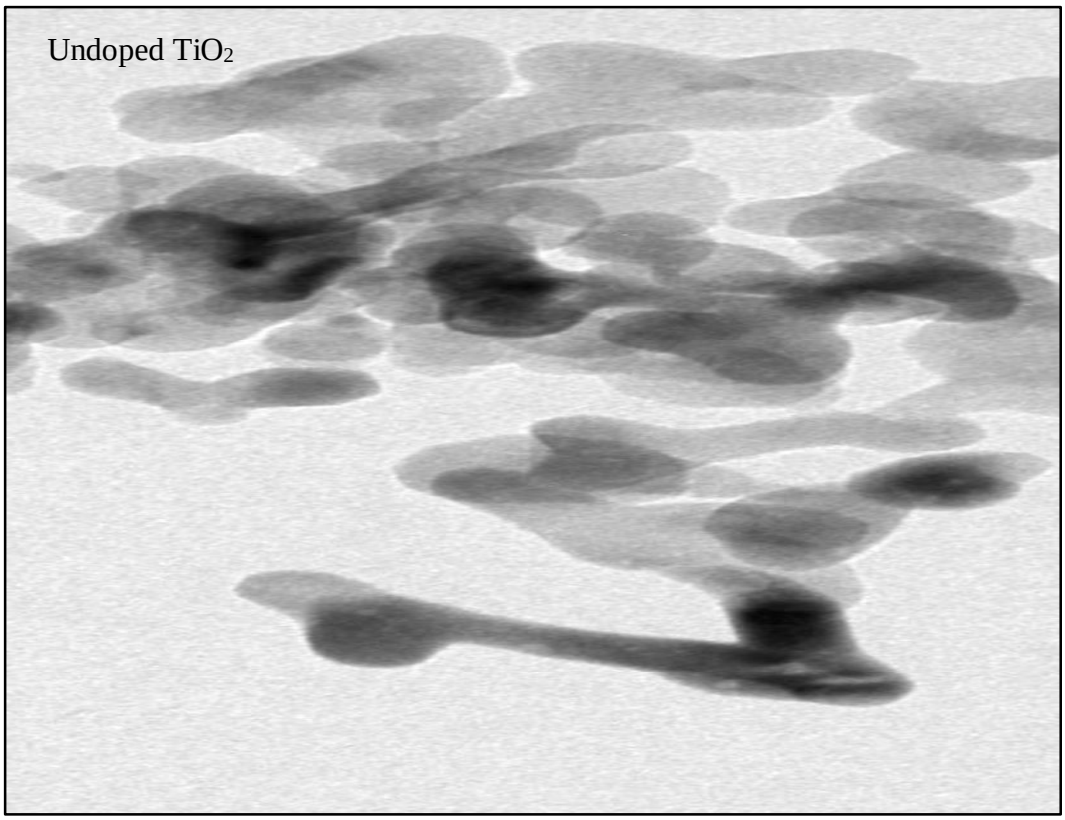

Fig 4.11. TEM image of undoped TiO_2 photocatalyst.

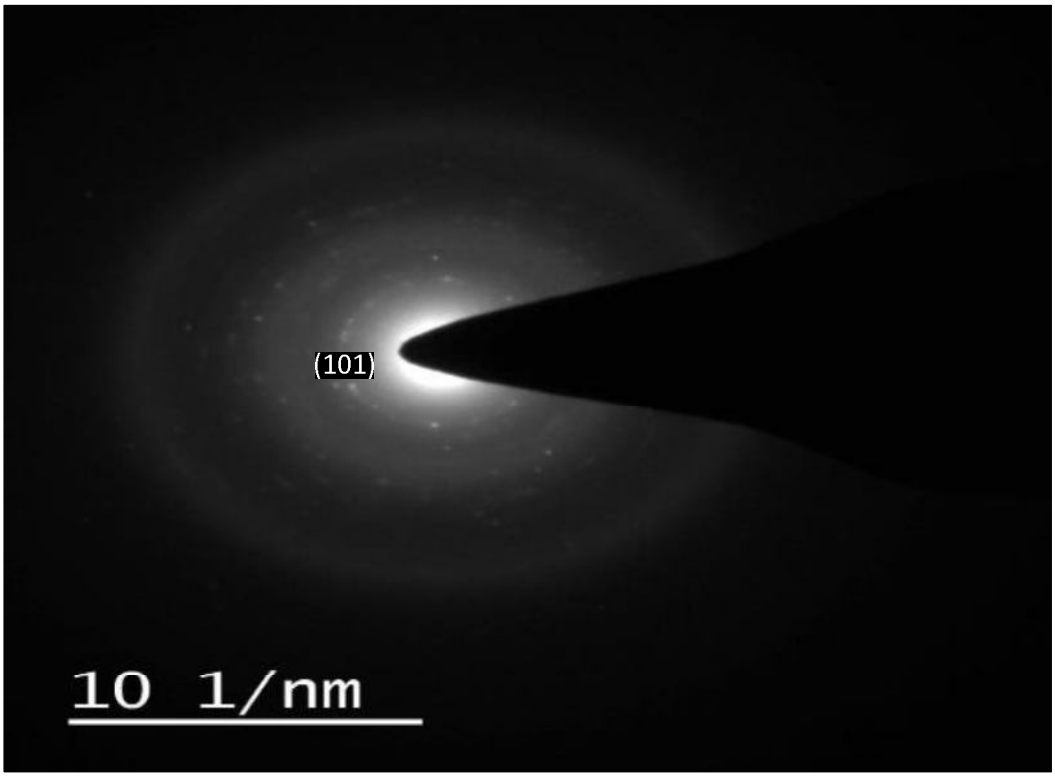

Fig 4.12. SAED image of undoped TiO_2 photocatalyst.

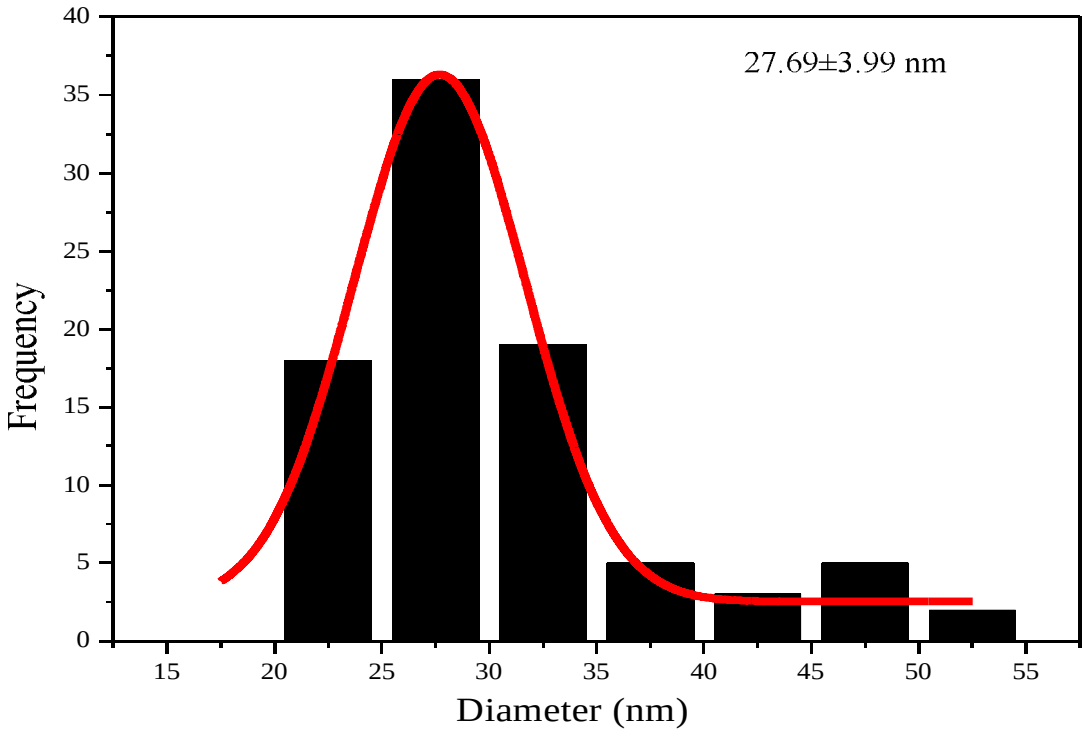

Fig 4.13. Particle size distribution of undoped TiO_2 photocatalysts.

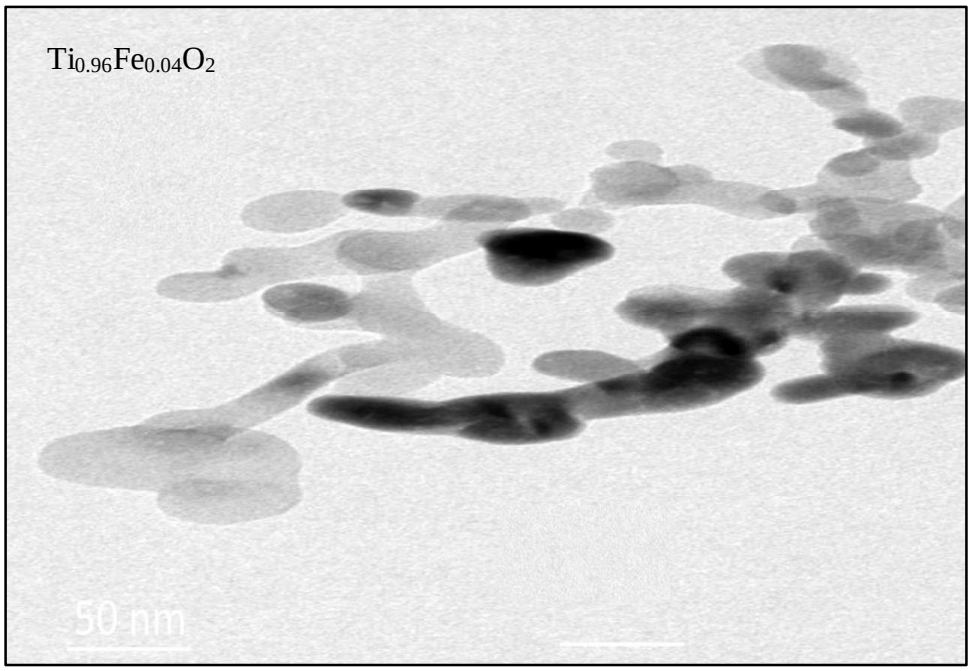

Fig 4.14. TEM image of $Ti_{0.96}Fe_{0.04}O_2$ photocatalyst.

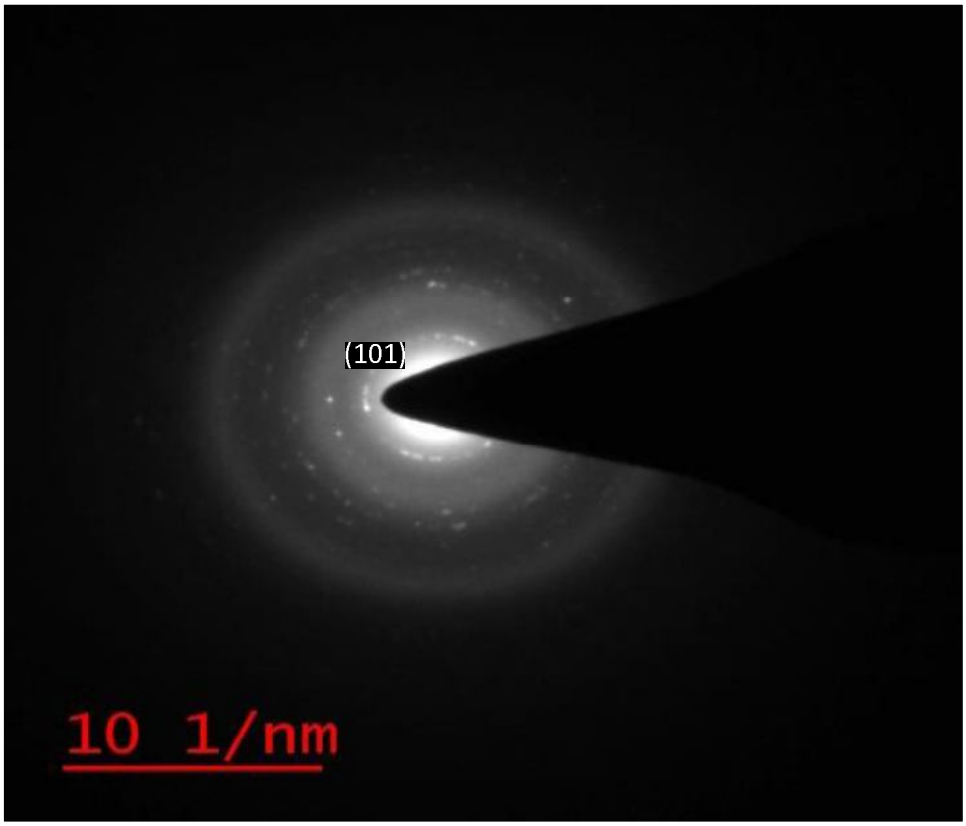

Fig 4.15. SAED image of $Ti_{0.96}Fe_{0.04}O_2$ photocatalyst.

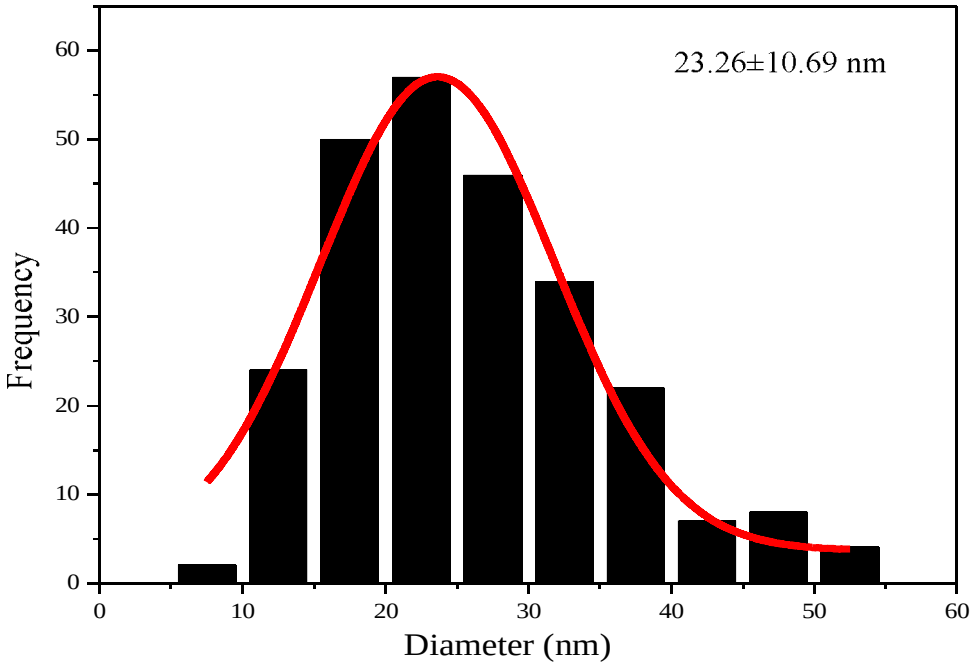

Fig 4.16. Particle size distribution of $Ti_{0.96}Fe_{0.04}O_2$ photocatalysts.

The particles size histograms of theses photocatalysts were shown in Fig 4.13 and Fig 4.16. The average particle sizes of these photocatalysts are 27.69±3.99 and 23.26±10.69 nm for undoped TiO_2 and $Ti_{0.96}Fe_{0.04}O_2$ respectively. The values of particles size were calculated from their particles size histogram. There is a good agreement between results of XRD analysis and histograms for average particles sizes calculation. The Fe doped TiO_2 nanoparticles synthesized via sol-gel route are reported to be spherical in shape with wide particles size range from 20-80nm (Singh et al. 2013).

EDX analysis was done to investigate the chemical composition and purity of the synthesized undoped and Fe doped TiO_2 photocatalysts (Fig 4.17). EDX analysis of undoped TiO_2 photocatalyst shows only the peaks of Ti and O element; there were no traces of any other impurity found except carbon. The carbon signals were detected by EDX instrument due to carbon tape or adventitious hydrocarbons.

Additional peaks of Fe were detected along with Ti and O peak in all the Fe doped TiO_2 samples.

Table 4.2a The EDX analysis of undoped and 1-4% Fe doped TiO_2 photocatalysts.

Photocatalyst	**Elements**	**Weight%**	**Atomic%**
(a) Pure TiO_2	C	4.35	10.63
	Ti	76.14	57.51
	O	19.51	31.86
(b) $Ti_{0.99}Fe_{0.01}O_2$	C	3.61	8.55
	Ti	69.84	35.78
	O	23.43	53.21
	Fe	3.12	2.46
(c) $Ti_{0.98}Fe_{0.02}O_2$	C	3.85	8.18
	Ti	66.41	78.45
	O	28.27	12.83
	Fe	1.47	0.54
(d) $Ti_{0.97}Fe_{0.03}O_2$	C	5.61	9.34
	Ti	63.10	42.69
	O	26.42	45.71
	Fe	3.59	2.64
(e) $Ti_{0.96}Fe_{0.04}O_2$	C	4.14	9.62
	Ti	64.64	77.39
	O	27.78	11.74
	Fe	3.44	1.25

Table 4.2b. The EDX analysis of 5-10% Fe doped TiO_2 photocatalysts.

Photocatalyst	Elements	Weight%	Atomic%
(f) $Ti_{0.95}Fe_{0.05}O_2$	C	4.22	7.69
	Ti	64.68	40.10
	O	27.51	49.57
	Fe	4.87	2.26
(g) $Ti_{0.94}Fe_{0.06}O_2$	C	4.31	8.40
	Ti	64.04	77.34
	O	27.25	12.63
	Fe	4.40	1.63
(h) $Ti_{0.93}Fe_{0.07}O_2$	C	3.15	7.44
	Ti	59.85	33.57
	O	31.88	55.35
	Fe	5.12	3.64
(i) $Ti_{0.92}Fe_{0.08}O_2$	C	4.42	7.98
	Ti	56.01	71.85
	O	34.39	17.94
	Fe	5.18	2.23
(j) $Ti_{0.91}Fe_{0.09}O_2$	C	4.12	8.25
	Ti	57.79	34.50
	O	31.56	52.62
	Fe	6.53	4.63
(k) $Ti_{0.90}Fe_{0.10}O_2$	C	5.08	9.35
	Ti	52.23	65.51
	O	36.32	22.65
	Fe	6.37	2.58

The results of EDX analysis are shown in Tables 4.2 (a-b). The EDX results confirm the presence of all the elements (Ti, O and Fe) in the synthesized Fe doped TiO_2 photocatalysts, which is consistent.

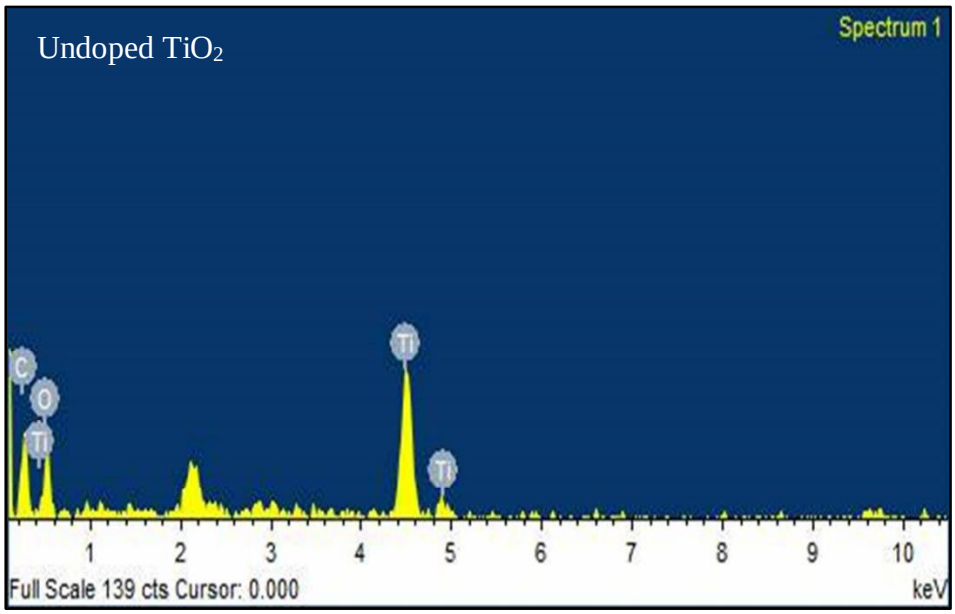
Undoped TiO_2
Spectrum 1
C
O
Ti
Ti
Ti
1 2 3 4 5 6 7 8 9 10
Full Scale 139 cts Cursor: 0.000
keV

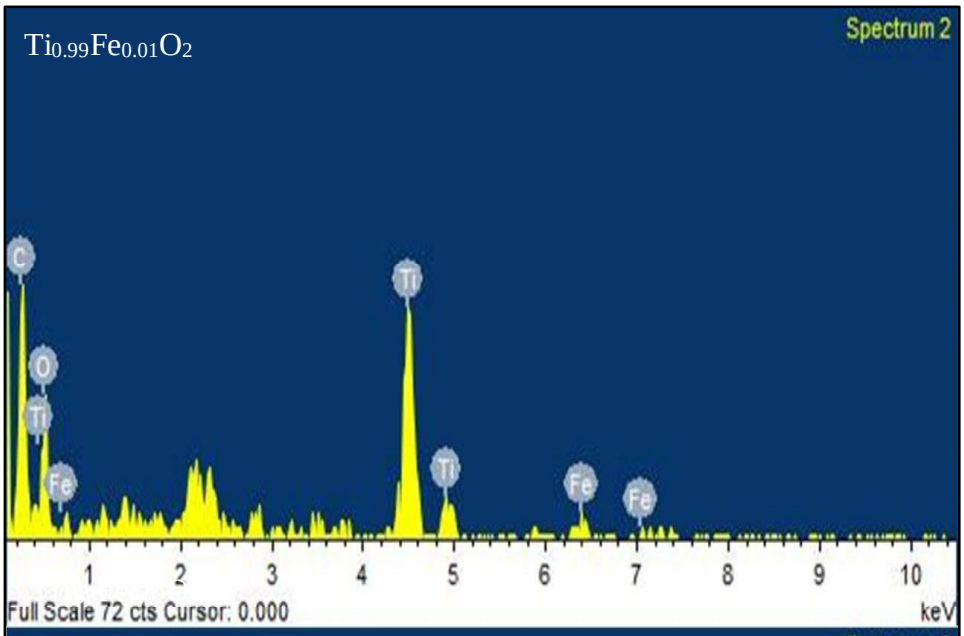
$Ti_{0.99}Fe_{0.01}O_2$
Spectrum 2
C
O
Ti
Fe
Ti
Fe
Fe
1 2 3 4 5 6 7 8 9 10
Full Scale 72 cts Cursor: 0.000
keV

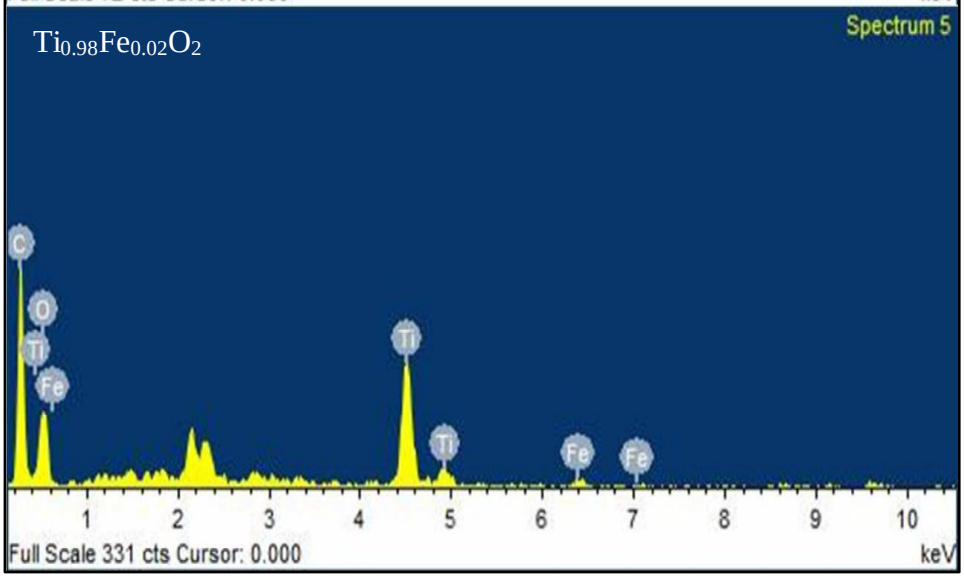
$Ti_{0.98}Fe_{0.02}O_2$
Spectrum 5
C
O
Ti
Fe
Ti
Fe
Fe
1 2 3 4 5 6 7 8 9 10
Full Scale 331 cts Cursor: 0.000
keV

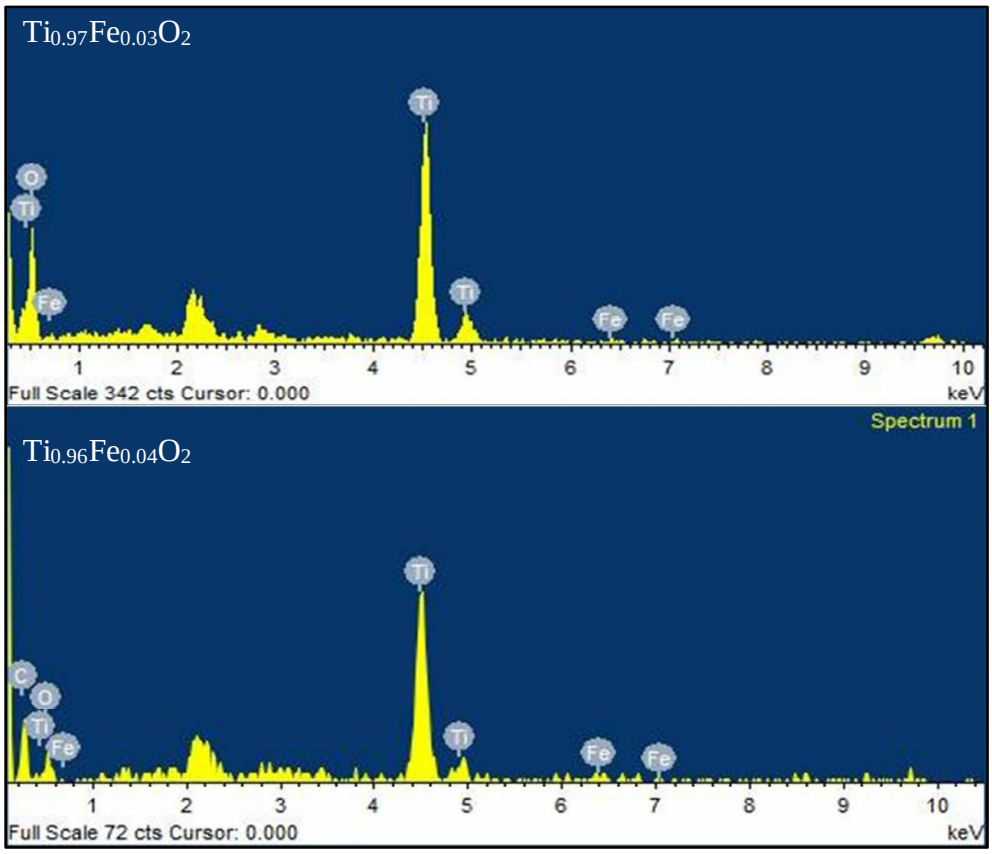
Ti0.97Fe0.03O2
O
Ti
Fe
Ti
Fe
Fe
1 2 3 4 5 6 7 8 9 10
Full Scale 342 cts Cursor: 0.000
keV
Spectrum 1
Ti0.96Fe0.04O2
C
O
Ti
Fe
Ti
Fe
Fe
1 2 3 4 5 6 7 8 9 10
Full Scale 72 cts Cursor: 0.000
keV

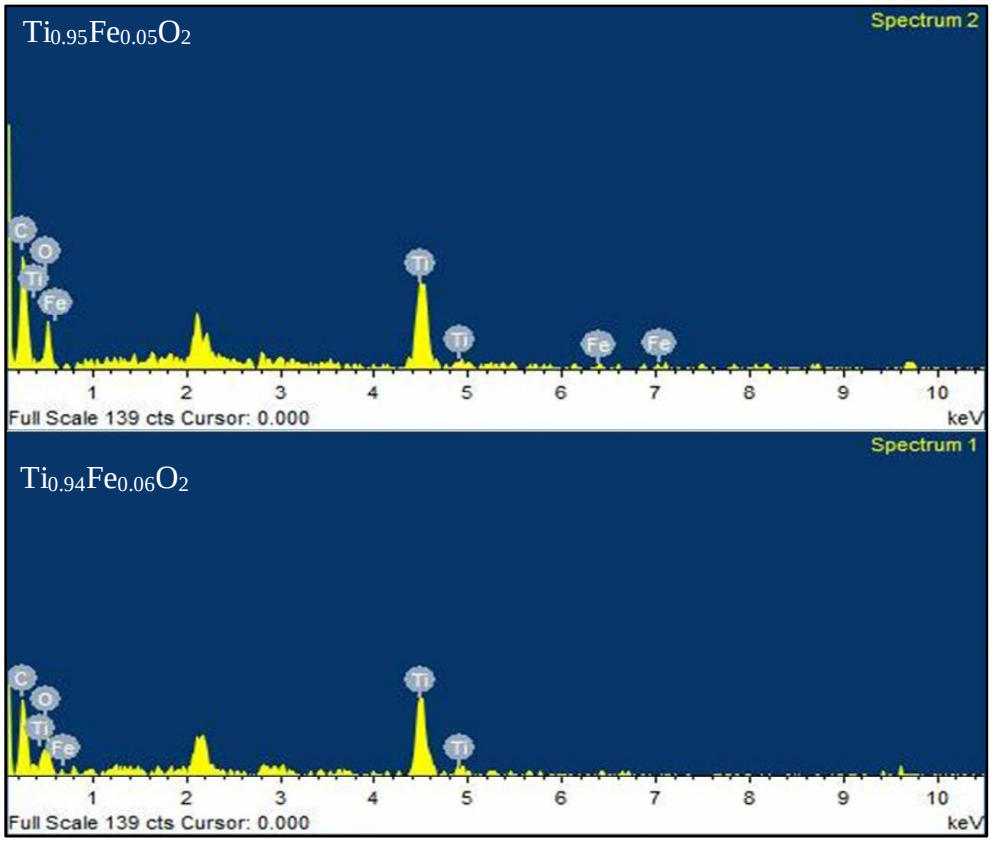
Ti0.95Fe0.05O2
Spectrum 2
C
O
Ti
Fe
Ti
Fe
Fe
1 2 3 4 5 6 7 8 9 10
Full Scale 139 cts Cursor: 0.000
keV
Spectrum 1
Ti0.94Fe0.06O2
C
O
Ti
Fe
Ti
1 2 3 4 5 6 7 8 9 10
Full Scale 139 cts Cursor: 0.000
keV

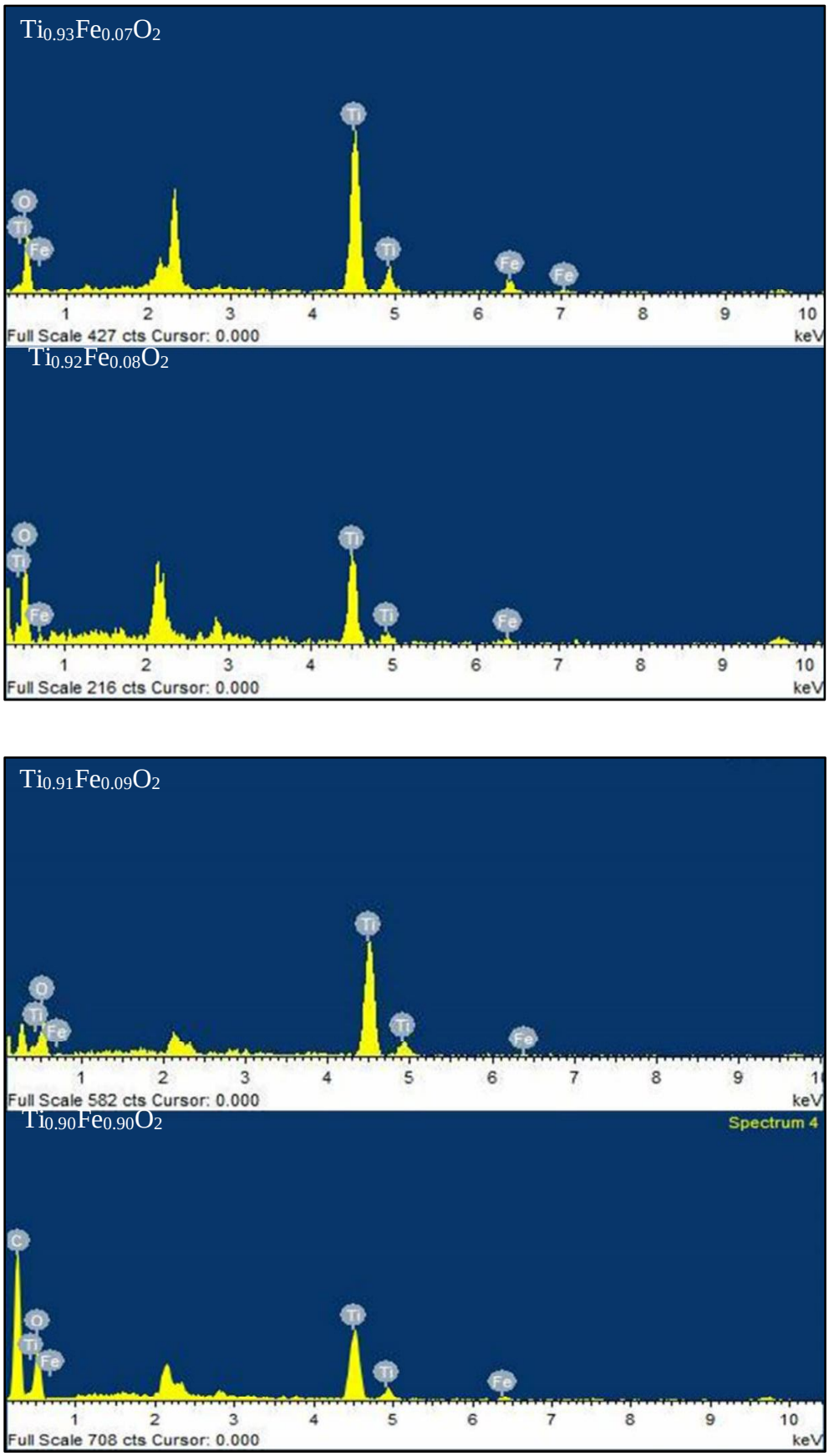

Fig 4.17. EDX analysis of undoped and (1-10%) Fe doped TiO_2 photocatalyst.

4.3 Mechanism of TiO_2 photocatalyst and enhancement of its activity by doping of Fe

The photocatalytic degradation of dye with TiO_2 occurs by photocatalytic oxidation. The detailed mechanism is available in previously reported works (Zhan and Tian 1998; Bandara et al. 1999; Tanaka et al. 2000; Galindo et al. 2000; Houas et al. 2001; Bianco Prevot et al. 2001; Daneshvar et al. 2003). When the TiO_2 suspension in water is exposed to radiation having energy greater than band gap energy, the conduction band electron and valance band holes are generated. The photogenerated conduction band electron and valance band holes can reduce and oxidize the dye, respectively. Alternatively electrons react with electron acceptor adsorbed O_2 on TiO_2 surface or dissolved in water to form superoxide anion $O_2^{-\bullet}$ radicals. However, valence band holes reacts with OH^- or H_2O and oxidize them into $OH^\bullet$ radicals; these radicals along with highly oxidizing species (peroxide radicals) are responsible for photo decomposition of the organic pollutant (dye) molecules. The substitution of Ti^{4+} with Fe^{3+} by doping in TiO_2 lattice leads to modified band structure as evidenced by UV-Vis DRS spectra. Narrowing of band gap is visible; which occurs due to d-d transition between Fe^{3+} and conduction band electron and interaction between Fe^{3+} ions to form Fe^{4+} and Fe^{2+} which are spread across TiO_2 band gap. The above Fe^{4+} and Fe^{2+} states may trap electrons or holes. This may result in decreases in the rate of recombination of electron-hole pair and hence improved photocatalytic activity in visible radiation. Fe^{3+} can act as trapper of holes and electrons. Since Fe^{3+}/Fe^{4+} energy level lies above valance band, Fe^{3+} can trap a holes ($Fe^{3+} + h^+ \rightarrow Fe^{4+}$). The holes trapped in Fe^{4+} group reacts with OH^- to produce hydroxyl radicals ($Fe^{4+} + OH^- \rightarrow Fe^{3+} + OH^\bullet$). Fe^{3+} can trap both types of electrons, photogenerated or released from the conduction band and get

reduced to Fe^{2+} ($Fe^{3+} + e^- \rightarrow Fe^{2+}$). Fe^{2+} is relatively unstable and hence it is oxidized to Fe^{3+} ($Fe^{2+} \rightarrow Fe^{3+} + e^-$). The electron liberated is transferred to the adsorbed O_2 molecule on catalyst surface ($O_{2(ads)} + e^- \rightarrow O_2^-$). In the above reaction, the O_2^- species have high power to break the chemical bonds of pollutant, while hydroxyl radicals are powerful oxidizing agents to oxidize the organic compounds (Moradi et al. 2016). The $O_2^{-\bullet}$ can easily trap holes and produce hydroxyl ion OH^- and hydroxyl radicals $OH^\bullet$ with water adsorbed on catalyst surface. ($O_2^{-\bullet} + h^+ \rightarrow O^{-\bullet}$; $O^{-\bullet} + H_2O \rightarrow OH^- + OH^\bullet$). The energy levels of Fe^{2+}/Fe^{3+} and Ti^{3+}/Ti^{4+} are close, therefore the electron liberated from Fe^{2+} oxidation can be transferred to surface Ti^{4+}, reducing it to Ti^{3+} which reacts with adsorbed oxygen and produce anions radicals. ($Fe^{2+} + Ti^{4+} \rightarrow Ti^{3+} + Fe^{3+}$; $Ti^{3+} + O_2 \rightarrow O_2^{-\bullet} + Ti^{4+}$). Also, Fe^{3+} ions at surface with trapped electron/hole can directly react with oxygen molecule (Fe-O_2) or with hydroxyl group (Fe-OH), this leads to the formation of $O_2^{-\bullet}$ and $OH^\bullet$ radicals, these also contribute an important role in photocatalysis (Wen et al. 2012). The presence of Ti^{3+} centers and oxygen vacancies (F^+ (shallow trap), F^{+2} (deep traps)) were identified using XPS. The formation of Ti^{3+} ions takes place by Ti^{4+} by the electrons of conduction band or transferred from oxygen vacancies ($Ti^{4+} + e^- \rightarrow Ti^{3+}$). Theses Ti^{3+} species can have interaction with surface adsorbed oxygen as mentioned earlier. The oxygen vacancies carry following two functions (i) trapping of valance band electron or (ii) promoting the trapped electrons to conduction band under visible light irradiation and thus reduce the recombination phenomena. In addition, the trapped electron in the oxygen vacancy (F^+ or F^{+2} trap) may also jump to OH acceptor levels and form hydroxyl radicals.

In summary, the doping of Fe on TiO_2 decreases band gap, consequently enhances adsorption of large number photon having energy between bandgap of

doped materials and undoped material. The charge carriers are trapped by following sites the Fe^{3+}, Fe^{2+} and Fe^{4+} as well the Ti^{3+} centers and oxygen vacancies; this leads to significant decreases in carriers recombination rate as a result the catalytic activity is enhanced. In our study, the combined effect of the two phenomena, trapping of electrons and reduction of e^-/h^+ recombination, was maximum at 4% Fe doping and hence maximum catalytic activity was observed at this concentration. The pictorial representation of dye degradation mechanism by synthesized Fe doped TiO_2 photocatalyst is shown in Fig 4.18.

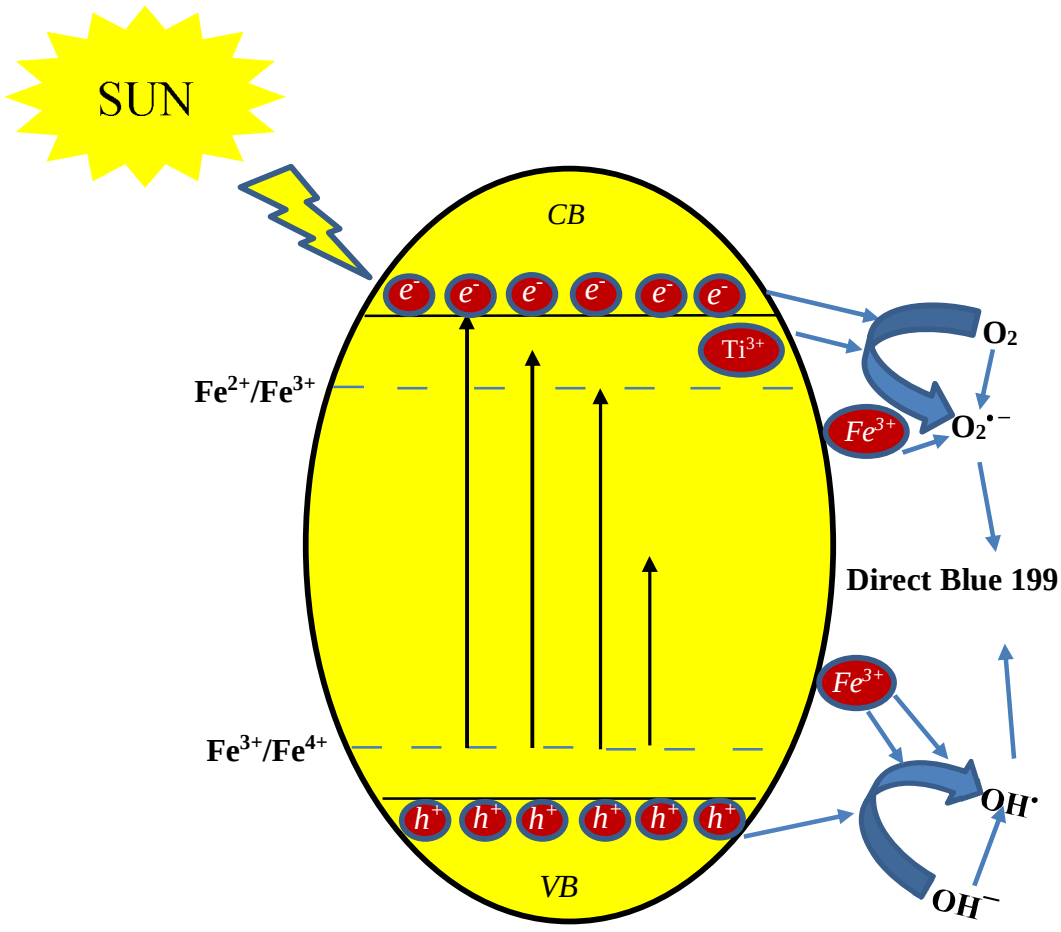

Fig 4.18. Pictorial representation of dye degradation mechanism by synthesized Fe doped TiO_2 photocatalysts.

4.4 FTIR analysis of treated simulated dye solution by $Ti_{0.96}Fe_{0.04}O_2$ photocatalysts

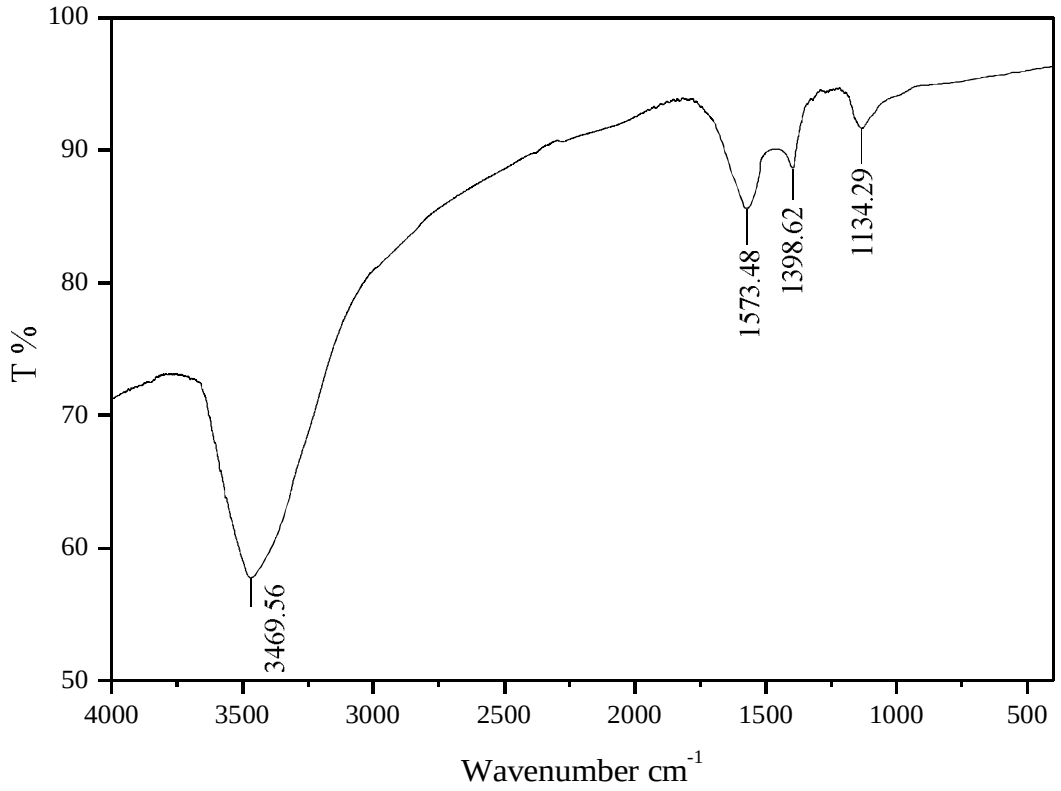

Fig. 4.19 FTIR analysis of photodegraded simulated dye solution.

FTIR spectrum of photodegraded simulated dye solution by $Ti_{0.96}Fe_{0.04}O_2$ photocatalyst is shown in Fig 4.19. The peak at 3469.56 cm^{-1} shows the presence of -NH-NH_2- stretch whereas the peaks at 1573.48 and 1134.29 cm^{-1} confirm the remaining amount of –SO_3Na- after the degradation of the dye. The absorption peak at 1398.62 cm^{-1} represents the C-H deformation. The peaks of -N=N- stretch (1577.6 cm^{-1}), C-H stretch (2945.4 cm^{-1}), –SO_3Na- (617.8 cm^{-1}) and Cu-N stretch (461.2 cm^{-1}) (as discussed in section 4.1) are eliminated from the simulated solution of dye and converted into the simpler compound such as H_2O, CO_2, SO_2 and CuO etc.

4.5 Kinetic studies of degradation of dye with Fe doped TiO_2 photocatalysts

The adsorption study of dye on undoped and Fe doped TiO_2 photocatalysts shows that only 2-3% of the dye was adsorbed on all the synthesized photocatalysts. The negligible photodegradation of dye was noticed in the absence of photocatalyst in UV-PCR and OPR.

The kinetic studies of all the thirty-three systems were done and one of them (system 16) is presented in Fig 4.20. The data obtained from all the systems (Table B1-B33) were well fitted with pseudo-first-order kinetics equation (4.1).

$$-\frac{dC}{dt} = K_{app}C \tag{4.1}$$

Where, C = the concentration of the dye solution at any time t, C_o = the initial concentration of the dye solution and K_{app} = apparent first-order rate constant. The values of K_{app} for every system were determined from $-\ln(C/C_o)$ vs. t graph and given in Table C1-C4.

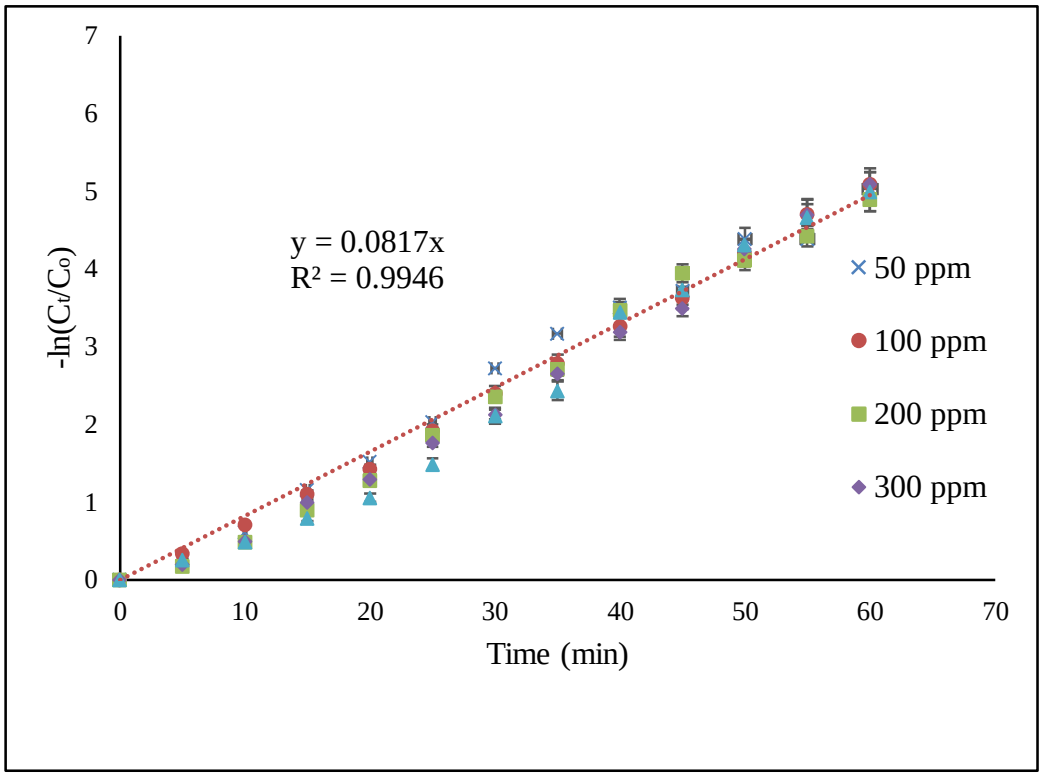

Fig 4.20. Kinetic study of dye degradation for system 16.

The data obtained from all the kinetic studies, it was observed from the data that the $Ti_{0.96}Fe_{0.04}O_2$ photocatalyst showed maximum photodegradation ability among all the undoped and Fe doped TiO_2 photocatalysts for the degradation of dye in simulated dye solution and industrial wastewater (Table C1-C4). The reaction rate constants (K*app*) of all the thirty-three systems (1-33) are given in Table C1-C4. The $Ti_{0.96}Fe_{0.04}O_2$ photocatalyst shows the maximum reaction rate constant $Kapp=8.17\times10^{-2}\ min^{-1}$ for system 16 in UV-PCR with quartz tube. The photocatalytic degradation of different dyes like Methyl Orange (MO) (Ghorai et al. 2008), Thymol Blue (TB) (Ghorai et al. 2008), Bromocresol Green (BG) (Ghorai et al. 2008), Rhodamine B (RB)(Ghorai et al. 2008; Fiorenza et al. 2018) and Malachite Green (Asiltürk et al. 2009) using Fe(III) doped TiO_2 photocatalysts has reported and all the above studies followed the pseudo-first-order kinetics. The

enhancement of photocatalytic activity of the Fe doped TiO_2 photocatalysts has been discussed in section 4.3. It was observed in the present study that at high doping concentration (5-10% Fe doped TiO_2) the photodegradation efficiency of Fe doped TiO_2 photocatalysts reduced for all the fifteen systems (7-11), (18-22) and (29-33) which indicates that doping concentration must be optimum. The reduction in photocatalytic activity at high doping concentration may be due to the multiple trapping of charge carrier and enhanced probability of electrons-holes recombination.

4.6 Activity of regenerated photocatalysts

The activity of regenerated $Ti_{0.96}Fe_{0.04}O_2$ photocatalyst was checked by the photodegradation of the industrial wastewater and shown in Fig 4.21. From the Fig 4.21, it was observed that the activity of regenerated photocatalyst decreases with the number of regeneration of the photocatalyst. The photodegraded and adsorbed dye (Direct blue 199) on the photocatalyst surface is the main cause of decreased photocatalytic activity of photocatalyst since the dye molecule has copper in its structure which fill the pore of the photocatalyst by forming the copper oxide (CuO). The presence of copper oxide peak in regenerated photocatalyst at Bragg's angle of 35.2 in XRD pattern reveals the existence of copper in regenerated photocatalyst (Fig 4.22). The copper oxide peak in XRD was approximately at same 2θ value in Cu doped TiO_2 (Sahu and Biswas 2011).

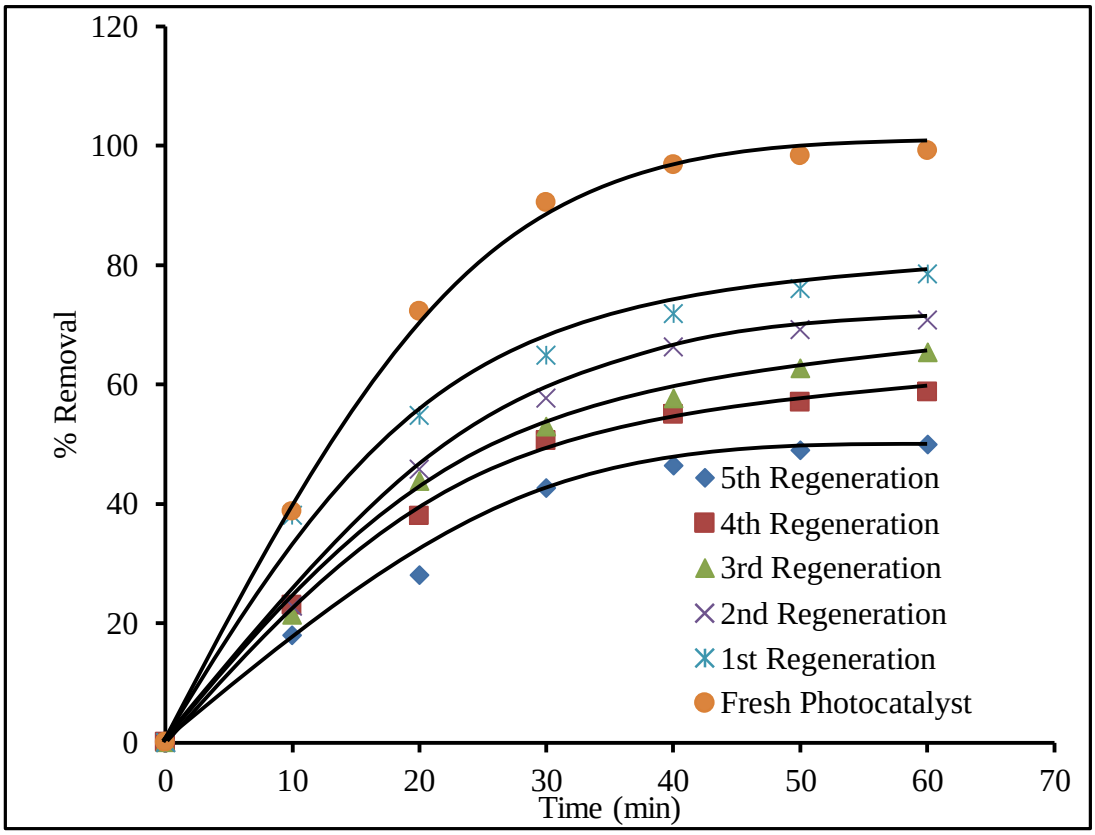

Fig 4.21. Performance of regenerated $Ti_{0.96}Fe_{0.04}O_2$ photocatalyst for photodegradation of wastewater (Direct Blue 199) in photocatalyst reactor with quartz tube.

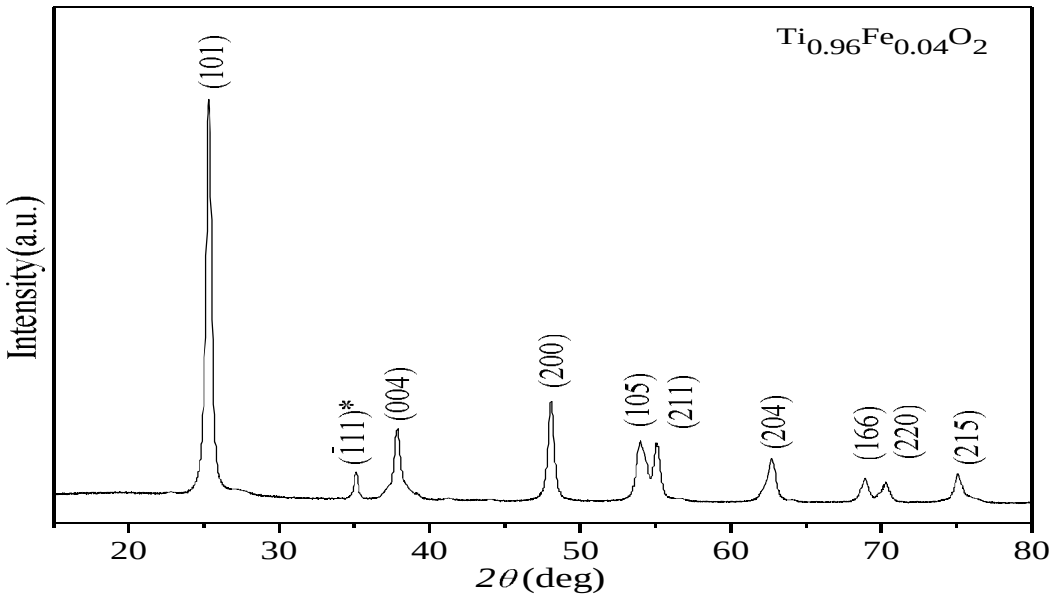

Fig 4.22. XRD spectra of regenerated $Ti_{0.96}Fe_{0.04}O_2$ photocatalyst.

Photodegradation of dye with regenerated $Ti_{0.96}Fe_{0.04}O_2$ photocatalyst in quartz tube is shown in Fig 4.23b; where R_1 represents the regeneration of catalyst first time, R_2 represents the regeneration second time after use of R_1 and similarly, R_3, R_4 and R_5 represent the regeneration the same catalyst third, fourth and fifth time respectively. The photodegradation of the dye (Direct Blue 199) in the UV-PCR by the best photocatalyst ($Ti_{0.96}Fe_{0.04}O_2$) in the quartz tube (A), the glass tube (B) and untreated sample (C) are shown in Fig 4.23a. Similarly, the regeneration of many photocatalysts, TiO_2 photocatalyst (Fiorenza et al. 2018), TiO_2 composites (Bougarrani et al. 2018; Meng et al. 2018), $CuCr_2O_4$ nanoparticles (Akhundi and Habibi-Yangjeh 2017) is reported in literature. These photocatalysts have been used to degrade different dyes such as Rhodamine B, Methylene Blue, Methyl Orange and Crystal Violet.

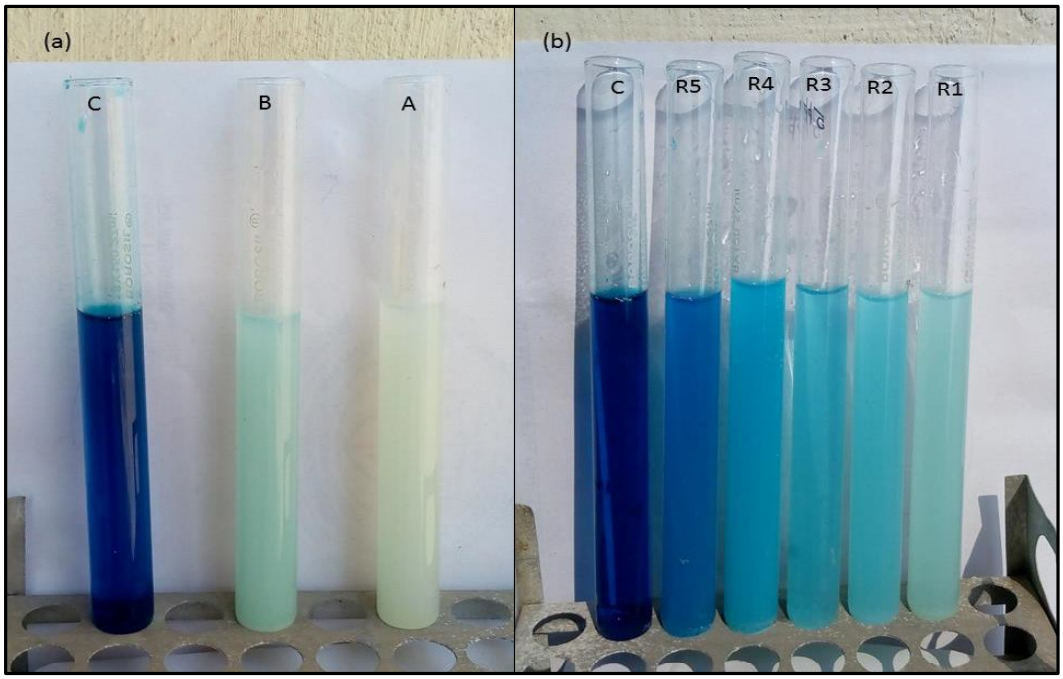

Fig 4.23. Digital Coloured pictures are proving the photodegradation of industrial wastewater in the photochemical reactor in quartz tube using (a) fresh $Ti_{0.96}Fe_{0.04}O_2$ photocatalyst (b) regenerated $Ti_{0.96}Fe_{0.04}O_2$ photocatalyst.

4.7 Activity of used photocatalysts without regeneration

The photocatalyst without regeneration shows only 6.67% of dye degradation ability, which in not significant for photocatalysis purpose. Hence, the photocatalyst without regeneration shows very less activity as compared to the regenerated photocatalyst.

4.8 Comparative study among the undoped, Fe doped TiO_2 and P-25 photocatalysts

Comparative study of the prepared undoped TiO_2 and best among the Fe doped TiO_2, i.e. $Ti_{0.96}Fe_{0.04}O_2$ and Aeroxide P-25 was done for degradation of wastewater and result is shown in Fig 4.24. As shown in Fig 30, the best photocatalytic activity was found in 4% Fe doped TiO_2 ($Ti_{0.96}Fe_{0.04}O_2$) photocatalyst among all the photocatalyst.

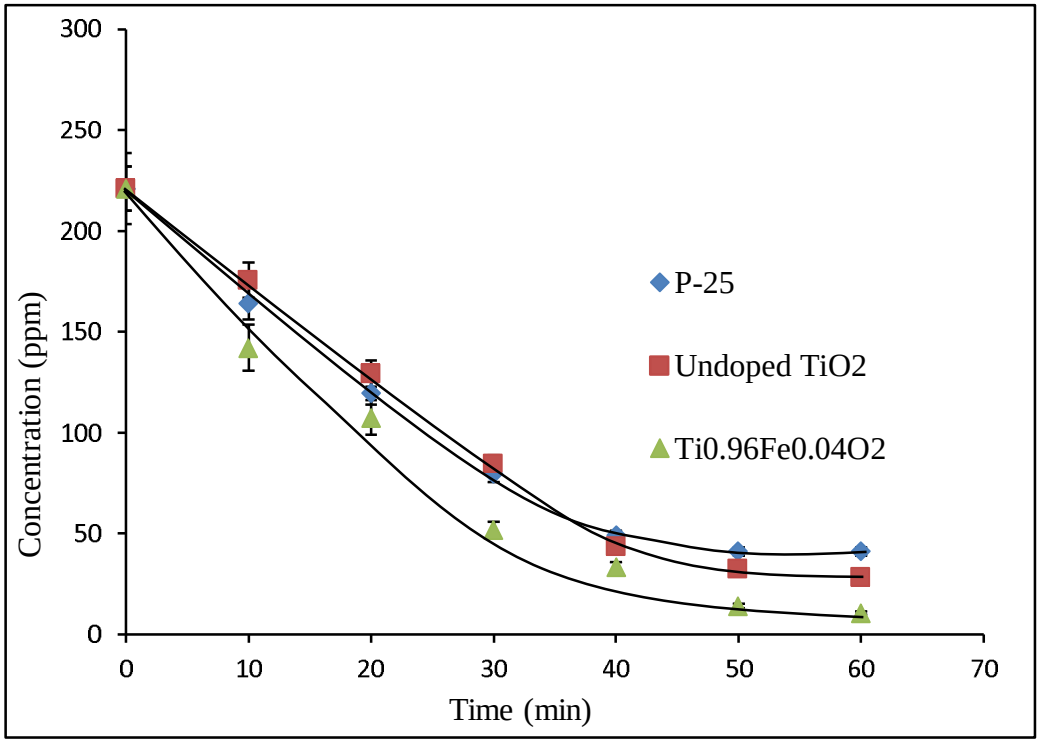

Fig 4.24. Comparison for best photocatalyst among synthesized undoped TiO_2, $Ti_{0.96}Fe_{0.04}O_2$ and P-25 for photodegradation of industrial wastewater.

I DOPED TiO_2

4.9 Characterization of I doped TiO_2 photocatalysts

I doped TiO_2 catalysts were prepared as per procedure given in section 3.2.3.1 (c). These were characterized by XRD, DRS, FTIR, XPS, HR-TEM and EDX. The results and discussion are given below.

3.5.1 X-Ray Diffraction Analysis (XRD)

The crystal structure and phases of the synthesized photocatalysts were determined by XRD analysis and shown in Fig 4.25. Fig 4.25 indicates that the synthesized catalysts have tetragonal structure and possess only anatase phase of TiO_2 (JCPDS card number 21-1272). Hou et al. (2011) synthesized the iodine doped TiO_2 nanoparticles via sol-gel route and obtained only the anatase phase of TiO_2 for dye-sensitized solar cell. As a photocatalysts, the most suitable phase of TiO_2 is anatase phase since it has extended electron-hole life than other phase of TiO_2 that makes it more appropriate for charge carrier to participate in surface reaction (Luttrell et al. 2014). Absence of iodine peak in XRD analysis at any concentration of iodine indicates that I^{5+} ions are successfully incorporated into the TiO_2 lattice.

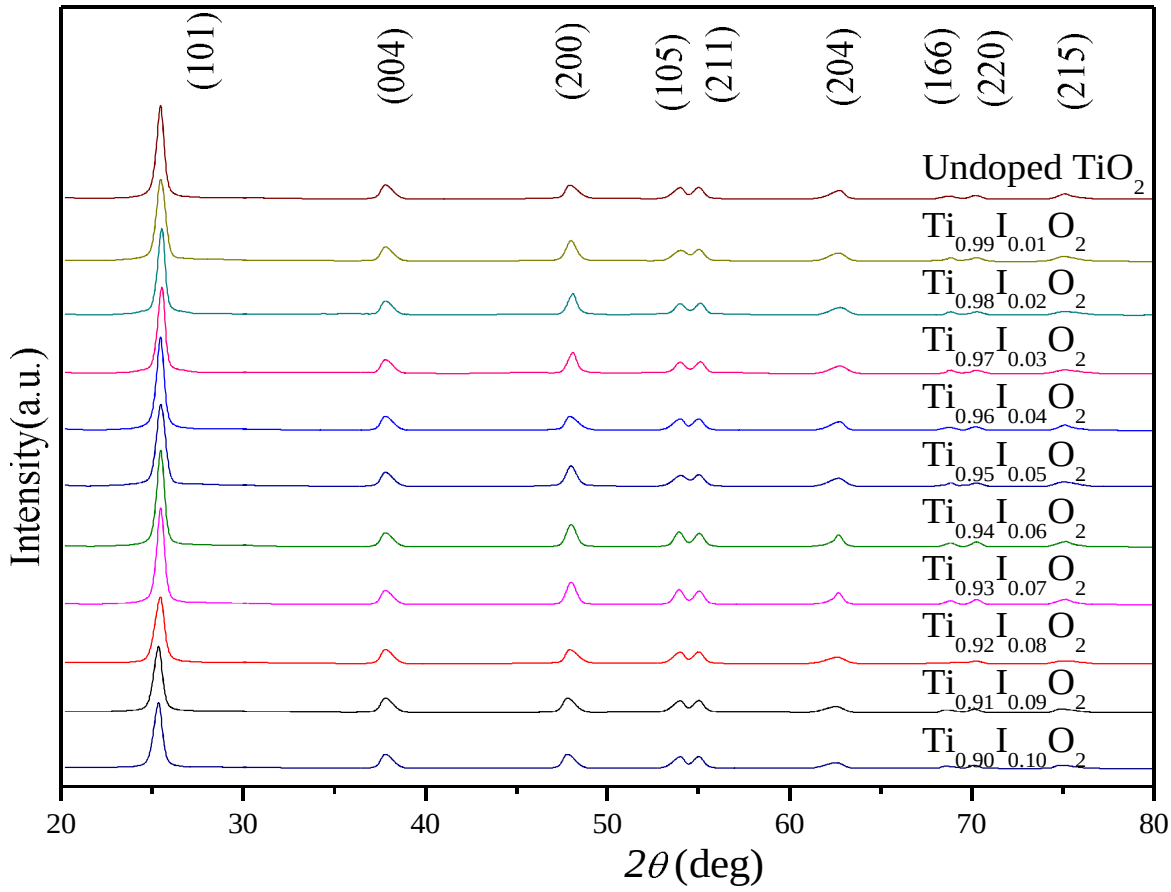

Fig 4.25 XRD spectra of undoped and 1-10% Fe doped TiO_2 photocatalysts

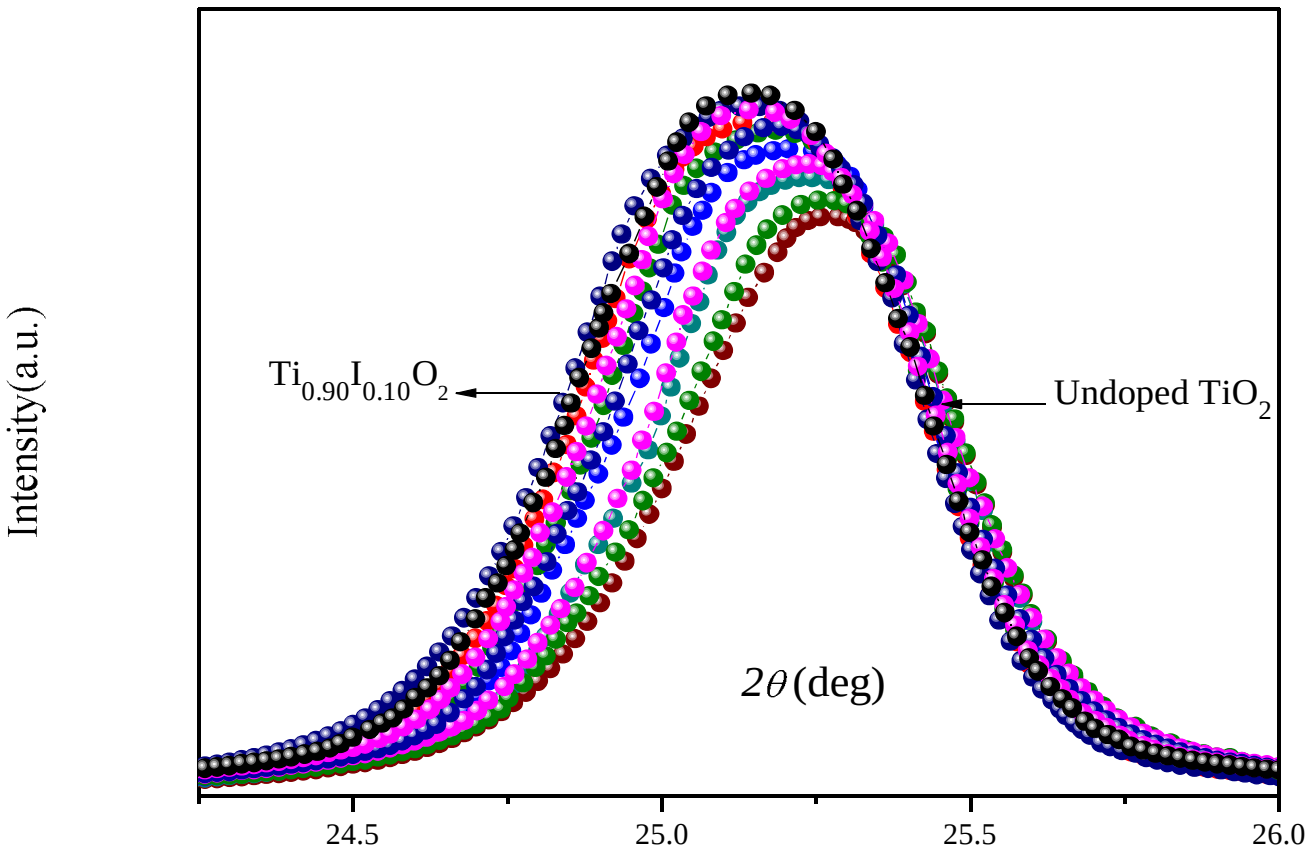

Fig 4.26 Characteristics peak (101) of anatase of TiO_2

Fig 4.26 shows the anatase characteristic peak (101) of the synthesized catalysts. The Fig 4.26 indicates that with increasing the iodine concentration in TiO_2, the peak (101) shifted towered the lower 2θ value and the peaks of doped catalysts become wider than undoped TiO_2. The behavior of peak (101) indicates some expansion in interplanar spacing between parallel crystallographic planes after the iodine doping in TiO_2 (Hou et al. 2011). Lu et al. (2010) also reported the shifting of (101) peak in his study of dye-sensitized solar cells using Nb-doped TiO_2 electrode .

The average crystallite size of the synthesized photocatalysts was determined using the Scherrer's formula (equation 3.4) and given in Fig 4.27. The Fig 4.27 indicates that iodine doping in TiO_2 increases the crystallite size of the synthesized catalysts and the size increases with increasing the doping concentration. The incorporation of iodine in TiO_2 lattice is the main cause of the crystal growth since atomic radius of iodine (198 pm) is larger than that of oxygen (152 pm) (Bondi 1964). Barkul et al. (2017) synthesized undoped and iodine doped TiO_2 photocatalysts by sol-gel method with particles size of 8.45 nm and 11.23 nm respectively for degradation of Rhodamine B from textile effluent.

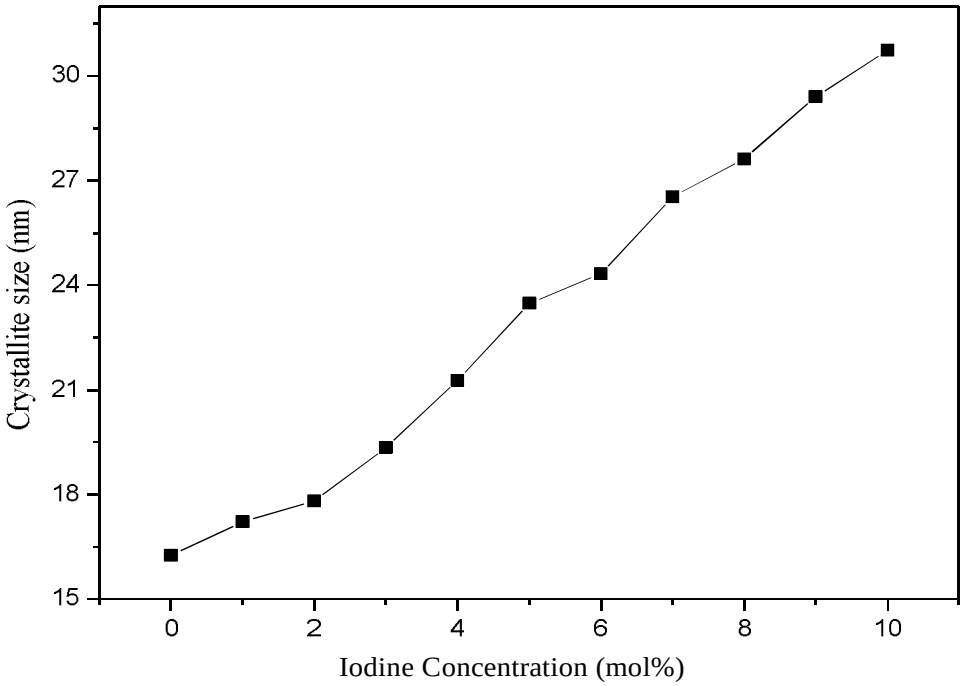

Fig 4.27. The effect of I concentration on crystallite size.

4.9.2 UV-Vis Diffuse Reflectance Spectroscopy (DRS)

The optical properties of undoped and iodine doped TiO_2 photocatalysts were determined using DRS analysis and shown in Fig 4.28 and Fig 4.29. The UV-Vis absorbance spectra of the synthesized photocatalysts recorded in the range of

200-800nm and shown in figure of Fig 4.28. Due to the doping of iodine in TiO_2, a shifting of absorption bands from UV to visible region can be observed in Fig 4.29 which indicates that all the iodine doped TiO_2 photocatalyst are active in visible light region.

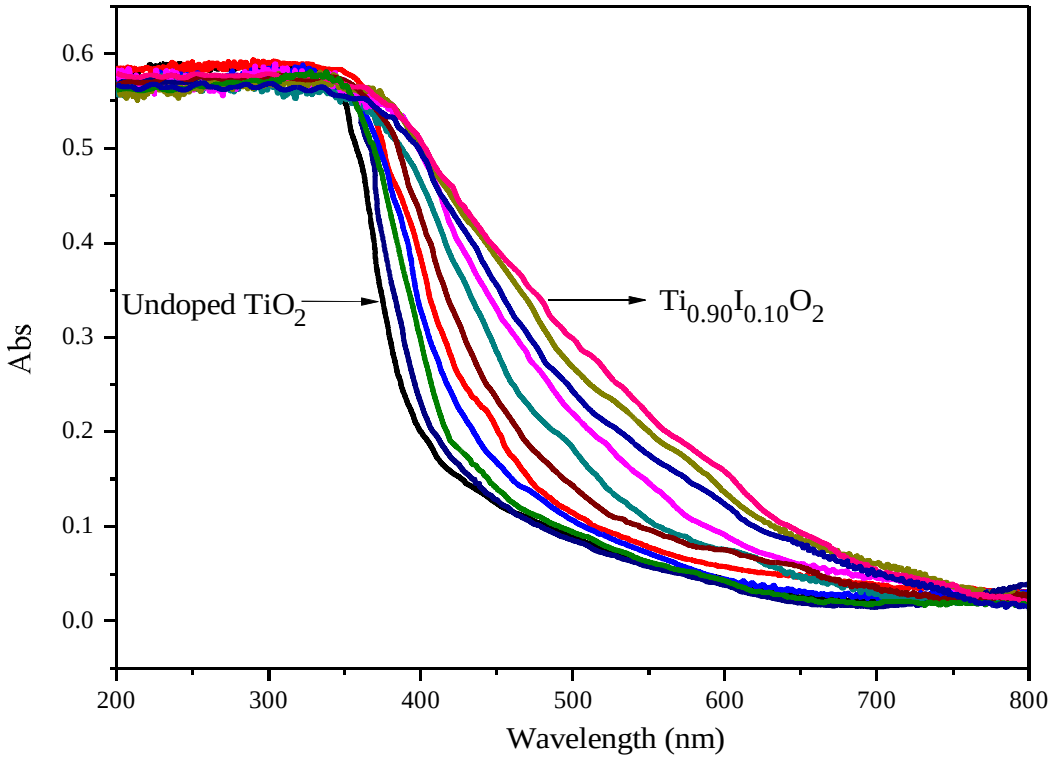

Fig 4.28 The UV-Vis diffuse spectra undoped and (1-10% I doped TiO_2).

With the help of $[F(R_\alpha)hv]^{1/2}$ vs. *hv* plot, the band gap energy of the synthesized samples was calculated using absorbance-wavelength data where the symbol $F(R_\alpha)$ is Kubelka-Munk function and it is given by equation (3.5).

$$F(R_\alpha) = (1 - R_\alpha)^2/2R_\alpha \qquad (3.5)$$

Where $R_\alpha = 10^{-A}$, the reflectance coefficient is calculated from A, A is the absorbance of the sample. As shown in the Fig 4.29, a continuous shifting in band

gap energy was observed in TiO_2 based photocatalyst after the doping of iodine in TiO_2.

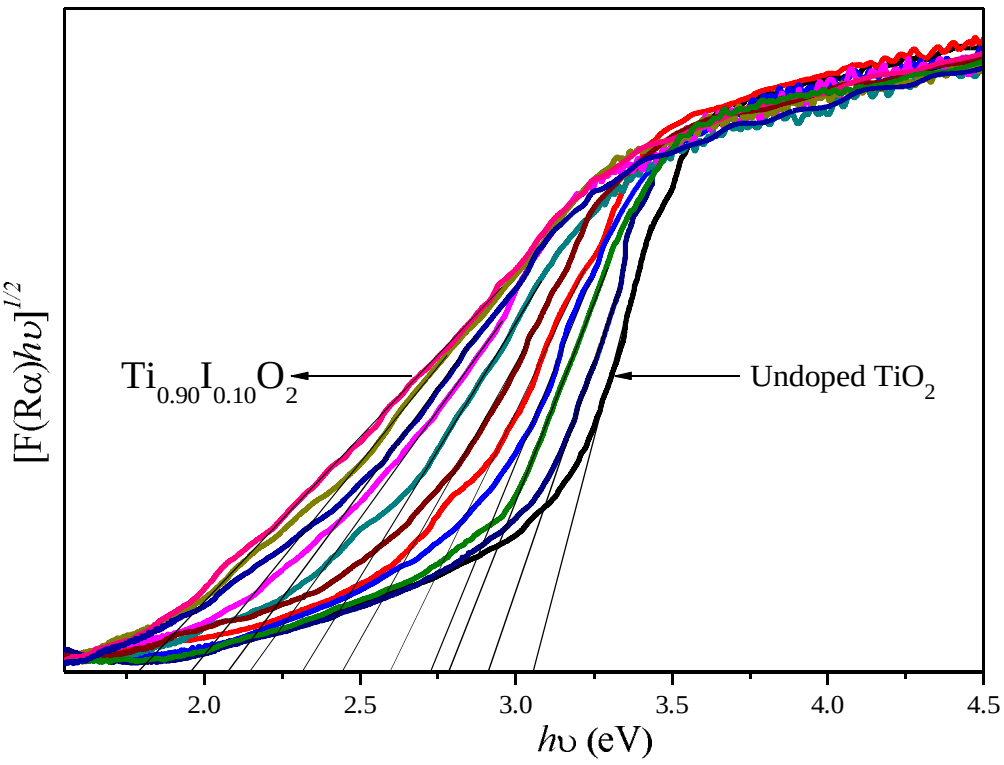

Fig 4.29 The plots of $[F(R\alpha)h\upsilon]^{1/2}$ vs. photon energy.

The Kubelka-Munk method was applied to calculate the indirect band gap energy of the synthesized photocatalyst and given in Fig 4.29. As observed in the Fig 4.30, the band gap energy was found to reduce with the increase of doping concentration into TiO_2 which reveals successful doping of I^{5+} into the lattice of TiO_2 (Ali et al. 2017). The absorption band shifts from UV to visible region is reported with doping of other transitional metal ions such as V, Cr, Mn, Co, Ni, and Cu etc. in TiO_2 lattice (Anpo 1997; Anpo et al. 1998, 1999) and the results of the present study have good agreement with these articles.

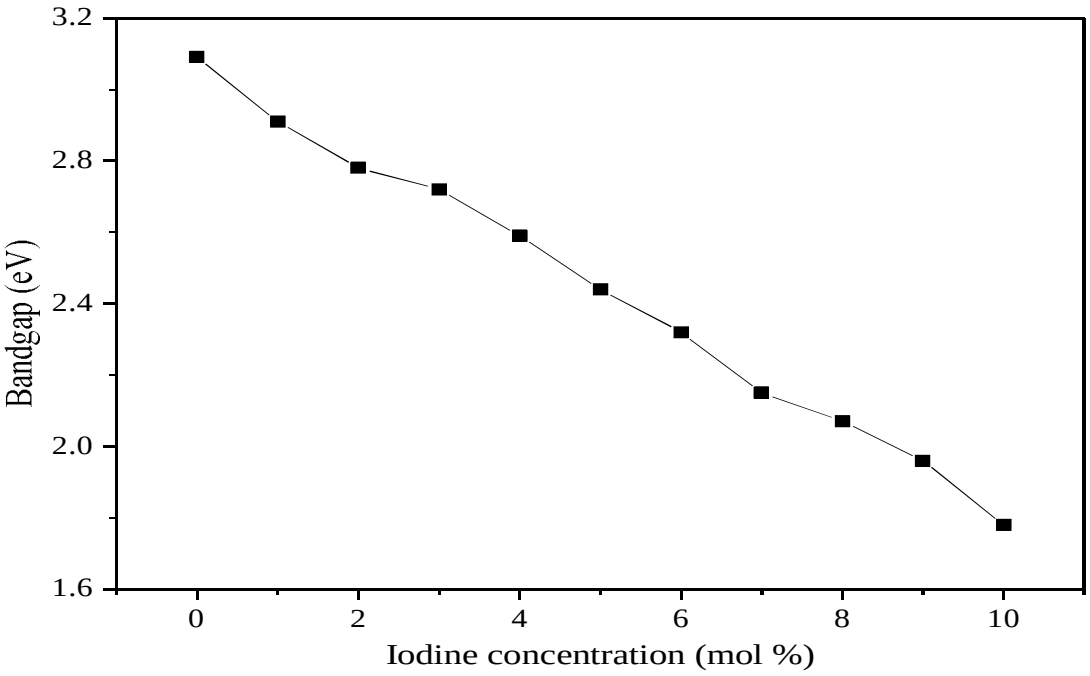

Fig 4.30 Variation of band gap energy with I concentration.

4.9.3 Fourier Transform Infrared Spectroscopy (FTIR)

The functional groups which are present in iodine-doped TiO_2 photocatalysts were determined by FTIR spectra and shown in Fig 4.31. The strong broad absorption peaks about 3500-300 cm^{-1} corresponds to the OH of physio-sorbed water on the TiO_2 surface while the weak bands about at 1550-1425 cm^{-1} are assigned to OH bending modes of water molecules (Li et al. 2009). The presence of a large number of OH groups in synthesized photocatalysts ensures its better photocatalytic activity since the main scavenging of the photogenerated charge carrier is carried by OH groups, this leads to the generation of hydroxyl radical ($OH^{\bullet}$) which is necessary for the photodegradation of the dye.

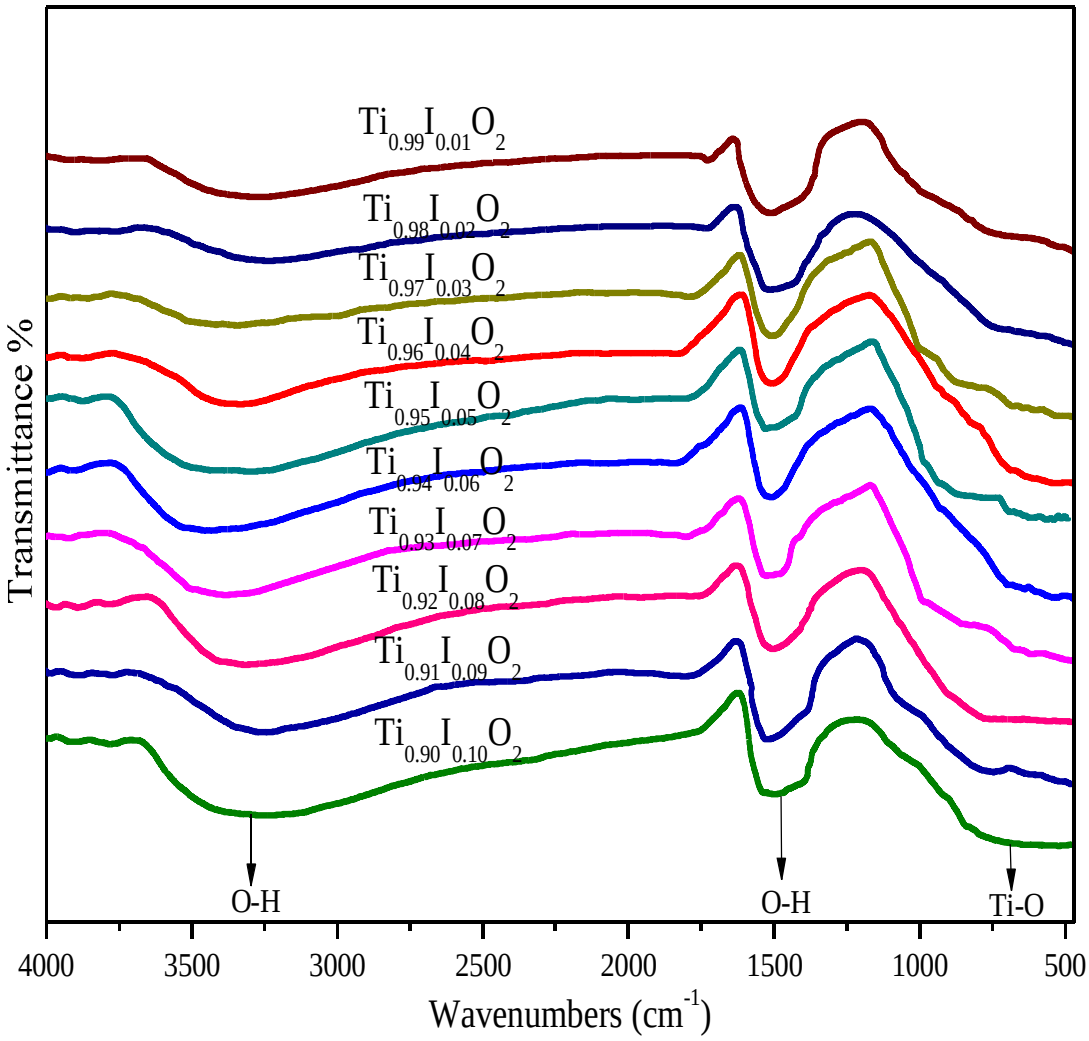

Fig 4.31. The FTIR spectra of undoped and I doped (0-10%) TiO_2 photocatalyst.

From the Fig 4.31, it is noticed that the absorbance intensity of the surface hydroxyl group enhances with increasing the iodine concentration in TiO_2 which confirms that incorporation of iodine in TiO_2 enriches its surface with hydroxyl group. Barkul et al. (2017) reported the enhancement of hydroxyl group due to the iodine doping in TiO_2. The strong absorption observed in the range of 900-500 cm^{-1} is attributed to lattice vibrations of anatase O-Ti-O bonding in TiO_2. Štengl and Grygar (2011) reported the O-Ti-O vibration above the 500 cm^{-1} range. In the Fig

4.31, no other peak was observed, which indicates that the iodine atoms could substitute Ti atoms in all the synthesized photocatalysts.

4.9.4 X-Ray Photoelectron Spectroscopy (XPS)

The XPS survey spectra of the synthesized 3% and 4% iodine doped TiO_2 photocatalyst is shown in Fig 4.32 (a) and 4.33 (a). The both survey spectra reveals the presence of Ti, O, I and C elements in the sample. The following binding energy areas were analyzed for both catalysts (1) Ti 2p region from 452-467 eV (2) O 1s region from 529-537 eV and (3) I 3d region from 617-638 eV. Figure 4.32 (b) and 4.33 (b) shows XPS peaks of Ti in 3% and 4% I doped TiO_2, where two high peaks of Ti^{4+} and two low peaks of Ti^{3+} were detected in both Fig 4.32 (b) and 4.33 (b). The Ti^{4+} peaks at 458.3, 458.5 and 463.9, 463.4 eV are correspond to Ti 2p3/2 and Ti 2p1/2 respectively. The small peaks at 457.2, 457.4 eV (Ti 2p3/2) and 462.9, 462.7 eV (Ti 2p1/2) are recognized as peaks of Ti^{3+} that is generated to maintain the electro-neutrality due to the substitution of I^{5+} at the place of Ti^{4+} into TiO_2 lattice (Zhang et al. 2011; He et al. 2008; Kaixi et al. 2008).

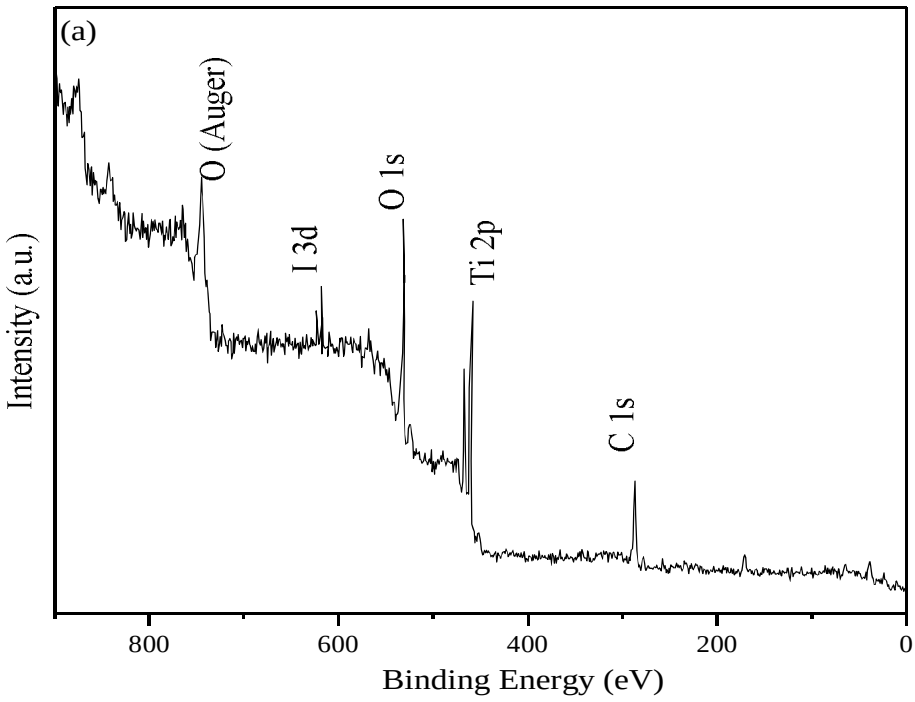
(a)
O (Auger)
I 3d
O 1s
Ti 2p
C 1s
Intensity (a.u.)
800
600
400
200
0
Binding Energy (eV)

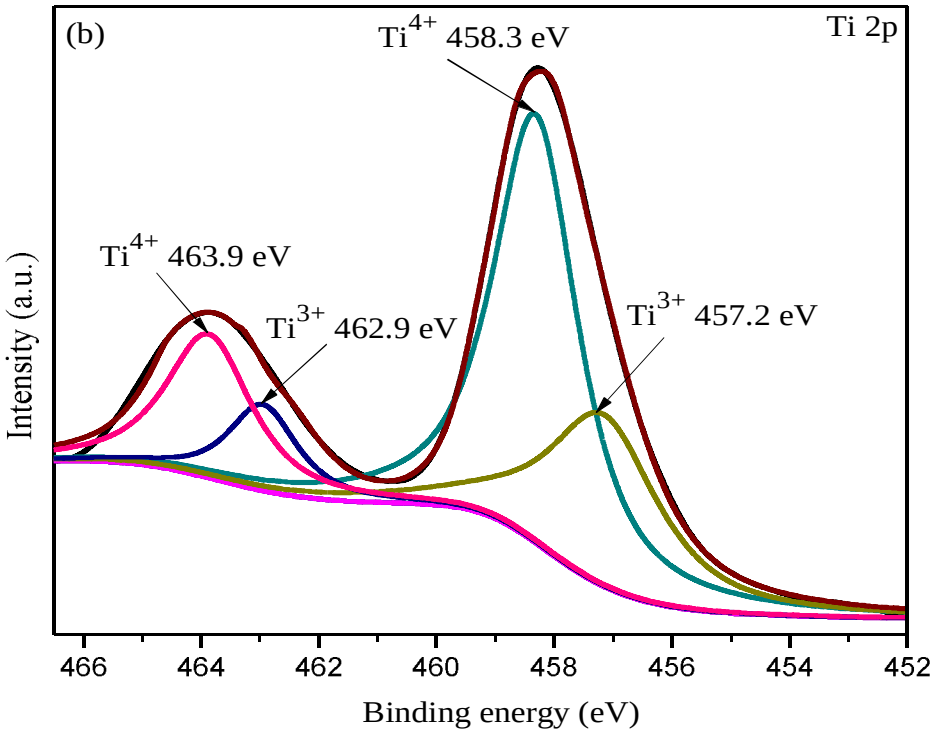
(b)
Ti 2p
Ti4+ 458.3 eV
Ti4+ 463.9 eV
Ti3+ 462.9 eV
Ti3+ 457.2 eV
Intensity (a.u.)
466
464
462
460
458
456
454
452
Binding energy (eV)

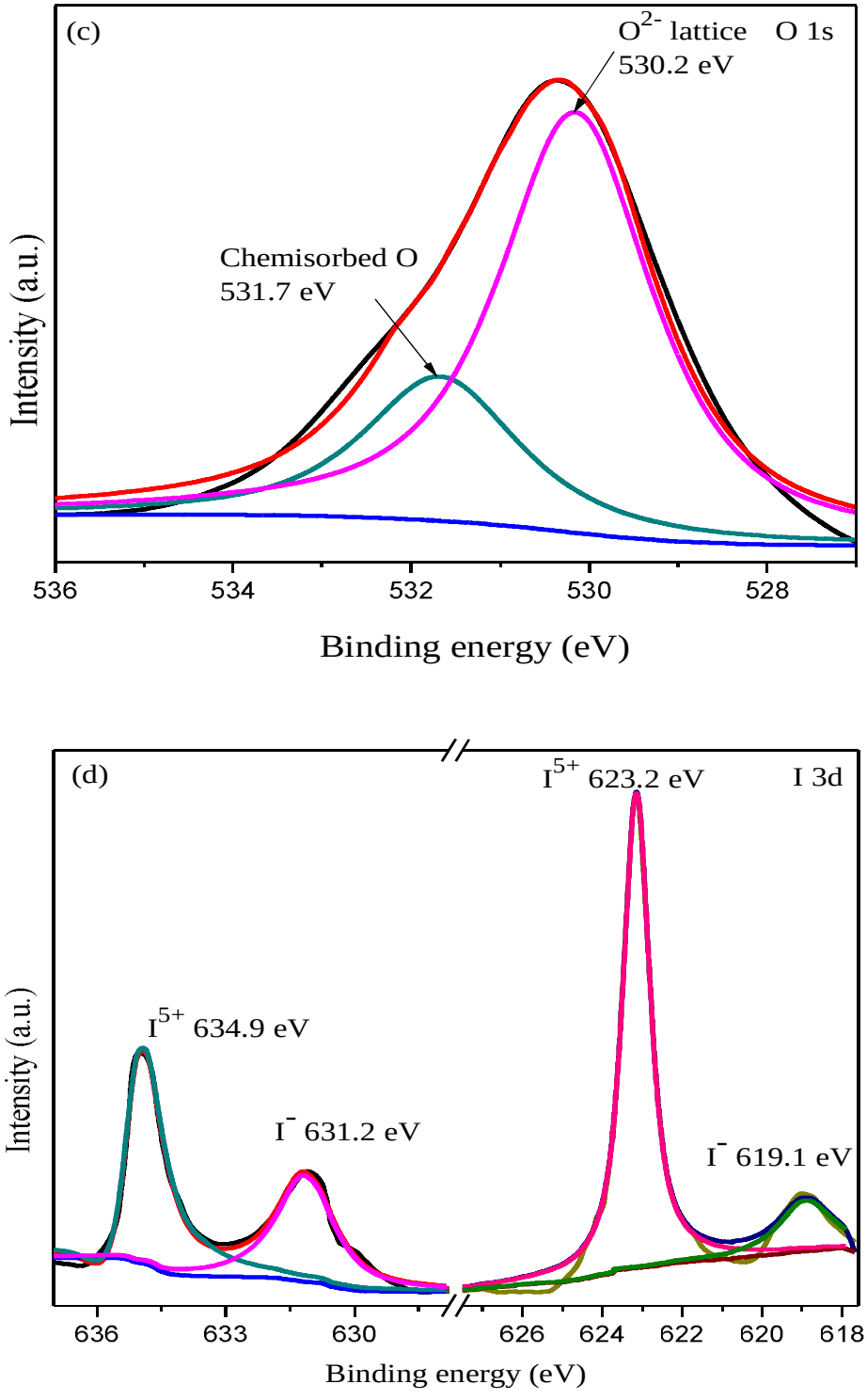

Fig 4.32. The XPS survey spectrum (a) and resolution scan over Ti 2p (b) O 1s (c) and I 3d (d) of 3% I doped TiO_2 photocatalyst.

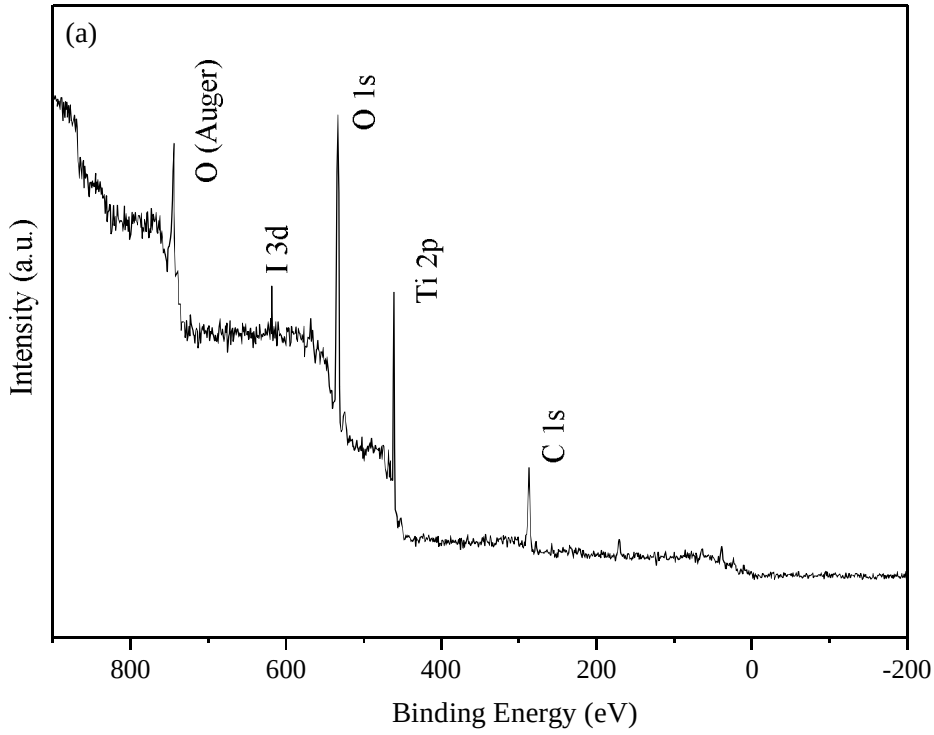
(a)
O (Auger)
I 3d
O 1s
Ti 2p
C 1s
Intensity (a.u.)
800
600
400
200
0
-200
Binding Energy (eV)

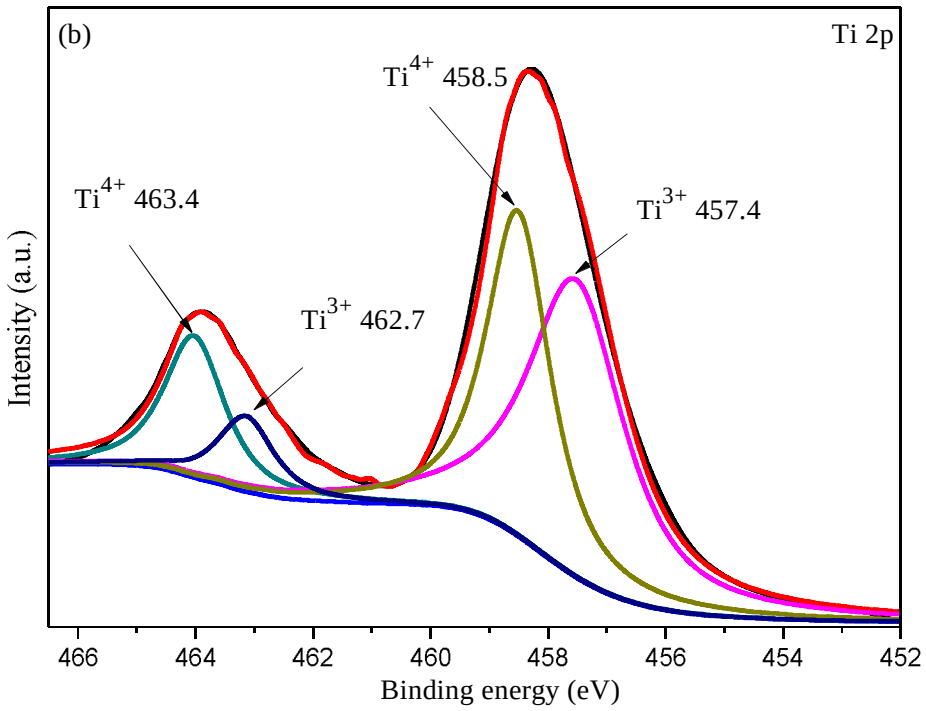
(b)
Ti 2p
Ti4+ 458.5
Ti4+ 463.4
Ti3+ 457.4
Ti3+ 462.7
Intensity (a.u.)
466
464
462
460
458
456
454
452
Binding energy (eV)

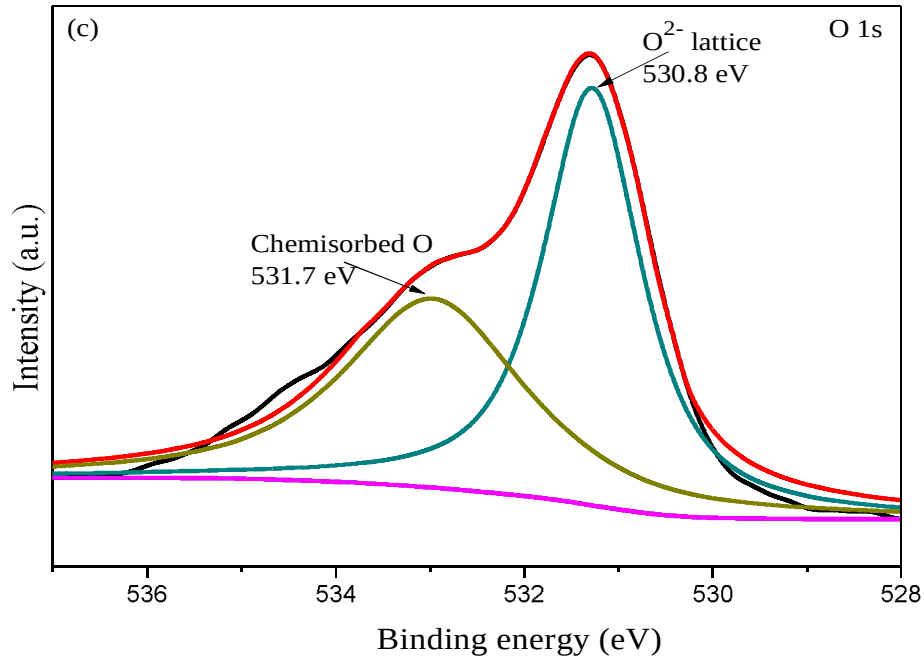

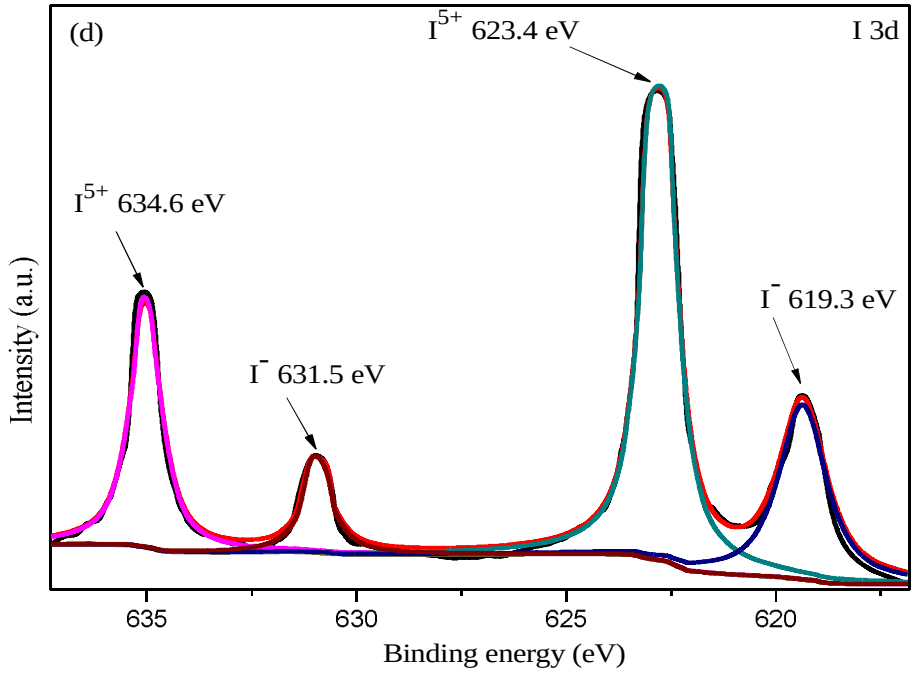

Fig 4.33 The XPS survey spectrum (a) and resolution scan over Ti 2p (b) O 1s (c) and I 3d (d) of 4% I doped TiO_2 photocatalyst.

Figure 4.32 (c) and 4.33 (c) represent the 3% and 4% I doped TiO_2 XPS spectrum of O 1s region that shows two peaks of oxygen, one of them is crystal lattice oxygen ($O^{2-}_{lattice}$) and other is chemisorbed hydroxyl oxygen peak (OH^-) (Ren et al. 2013). The peaks at 530.2 and 530.8 eV are attributed to crystal lattice oxygen ($O^{2-}_{lattice}$) whereas the peak at 531.7 and 531.5 eV represent chemisorbed hydroxyl oxygen peak (OH^-). These hydroxyl oxygen ions are extremely reactive and unstable, which can react with other atoms or group (dye in present case) to become stable (Xin et al. 2005). Kuo et al. (2013) reported that the hydroxyl oxygen plays an important role in photodegradation of Bisphenol A by carbon-doped TiO_2 photocatalyst. The XPS spectra of 3% and 4% I doped TiO_2 is shown in Figure 4.32 (d) and 4.33 (d). As shown in both figure, there are two duplets peaks of iodine. The main peaks at 623.2, 623.4 and 634.9, 634.6 eV indicate that the oxidation state of iodine is I^{5+}. Zhang et al. (2011) reported I^{5+} oxidation state of iodine in similar range. The weak satellite peaks at 619.1, 619.3 eV and 631.2, 631.5 eV infer that iodine also exist in I^- form in the synthesized photocatalyst. The presence of both ions (I^{5+}/I^-) of iodine in the synthesized photocatalyst has agreement with literature and represents the formation of I-O-Ti bond by substitution of I^{5+} for Ti^{4+} ions. In the present study, XPS analysis did not recognize any peak of I^{7+} peak at 624.0 eV, which was reported by (Su et al. 2008).

4.9.5. Structural morphology

In order to determine the structural morphology of the synthesized photocatalysts $Ti_{0.97}I_{0.03}O_2$, the TEM analysis was done. Fig 4.34 represents TEM image of photocatalysts. The TEM image indicates that the photocatalysts have spherical shape. With the help of SAED image, interplanar spacing (d_{hkl}) of diffraction rings were calculated and shown on the rings in Fig 4.35. The interplanar

spacing also indicates that the synthesized photocatalysts have anatase phase of TiO_2 as confirmed by XRD analysis.

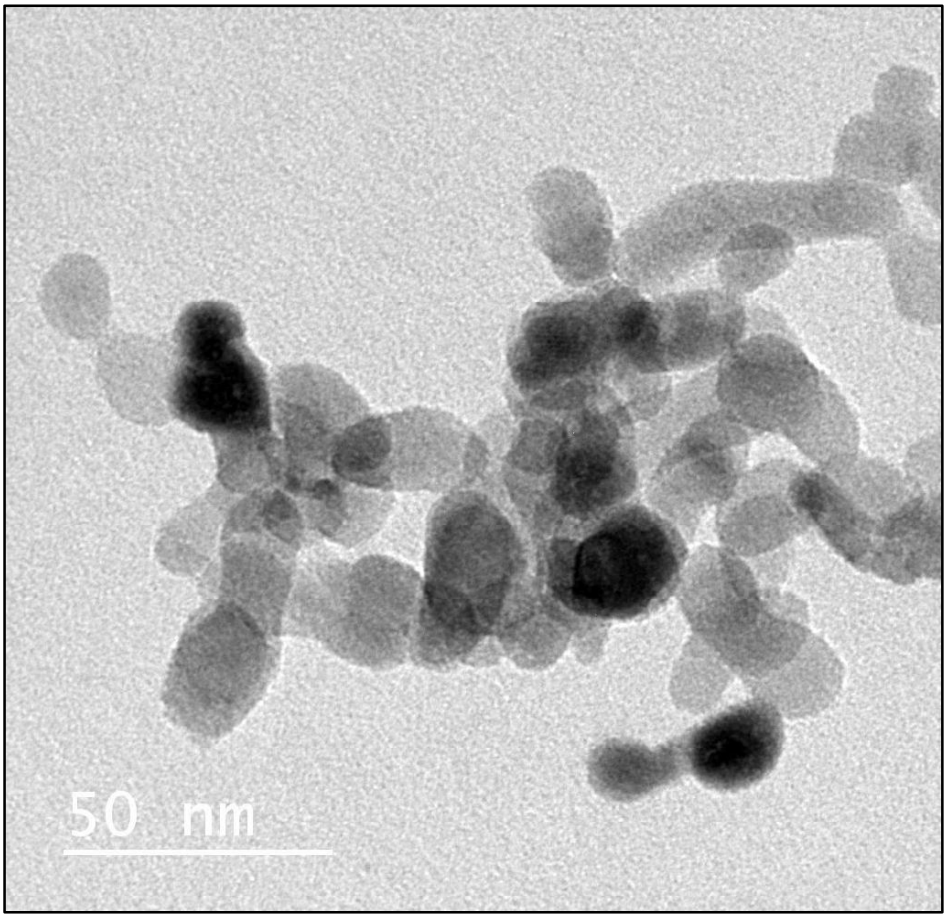

Fig 4.34 TEM image of $Ti_{0.97}I_{0.03}O_2$ photocatalyst.

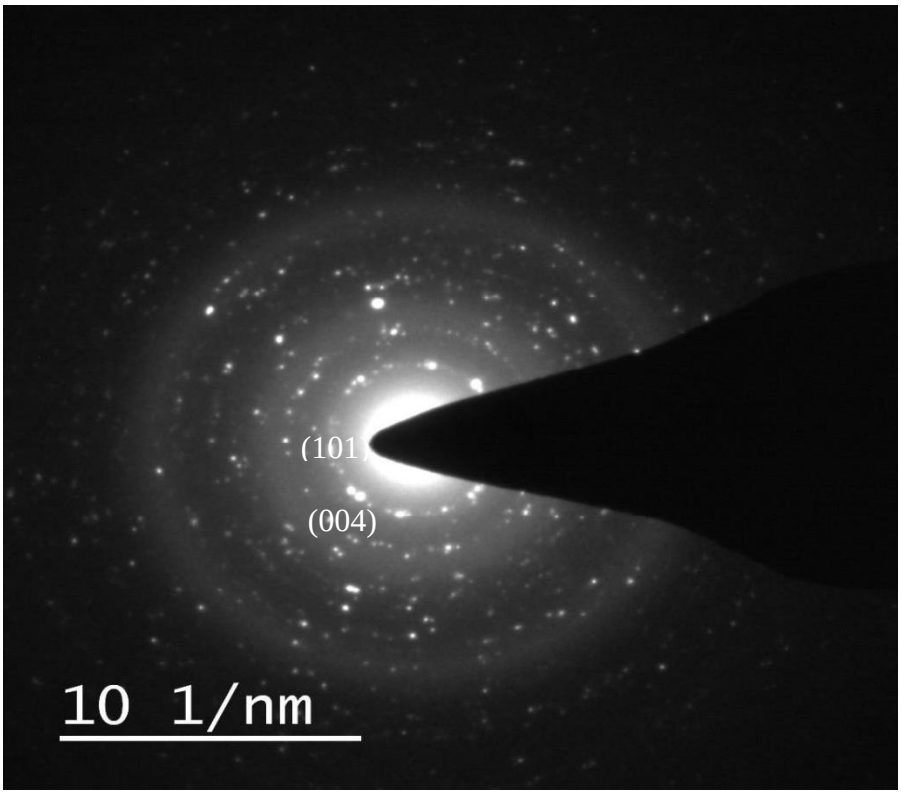

Fig 4.35 SAED image of $Ti_{0.97}I_{0.03}O_2$ photocatalyst.

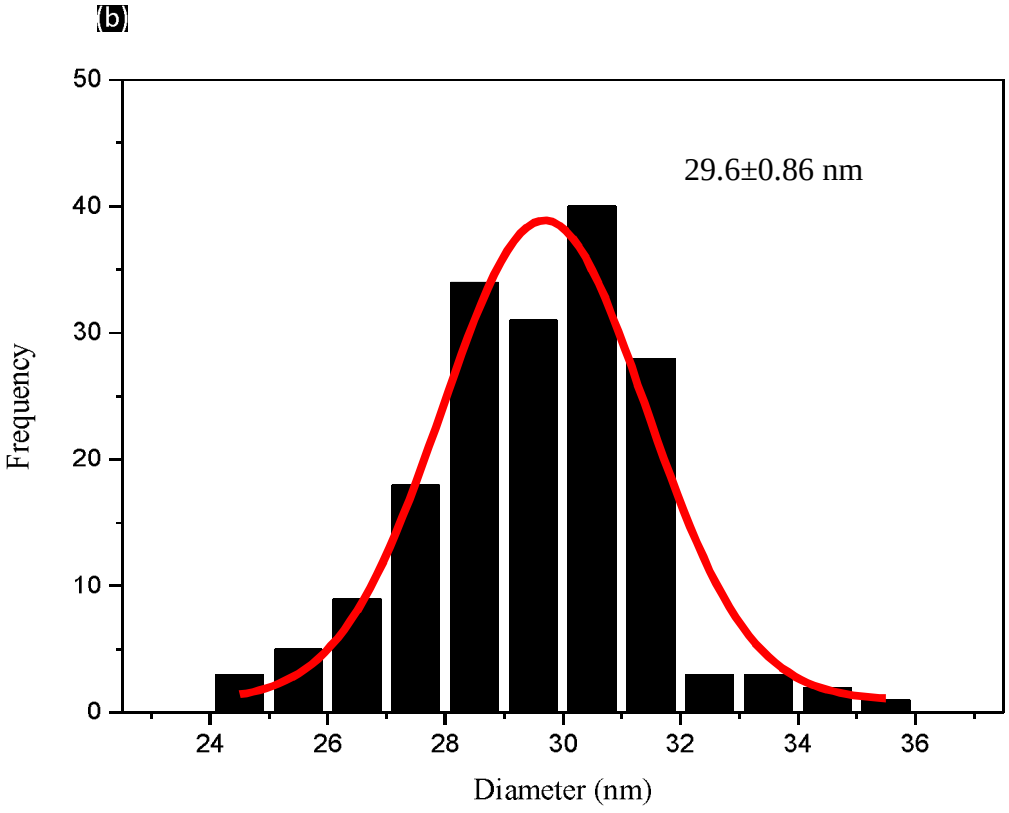

Fig 4.36 Particle size distribution of $Ti_{0.97}I_{0.03}O_2$ photocatalyst.

Fig 4.36 represents the particles size histogram of the synthesized ($Ti_{0.97}I_{0.03}O_2$) photocatalyst. With the help of histogram data, average particles sizes of photocatalysts were calculated and found that $Ti_{0.97}I_{0.03}O_2$ photocatalysts has average particles size of 29.6±0.86 nm. The $Ti_{0.97}I_{0.03}O_2$ has larger particles than undoped TiO_2 since iodine has greater atomic radius that of titanium which makes I doped TiO_2 particles bigger than undoped TiO_2.

The purity and composition of the synthesized photocatalysts were investigated by EDS analysis and shown in Fig 4.37. The EDS analysis of I doped TiO_2 found Ti, O and I peaks in the EDS analysis for all the synthesized I doped TiO_2 photocatalysts. The carbon signals were detected by EDX instrument due to carbon tape or adventitious hydrocarbons. Table 4.3 represent the results of EDS analysis.

Table 4.3. The EDX analysis of undoped and 1-10% I doped TiO_2 photocatalysts.

Photocatalysts	Elements	Weight%	Atomic %
(a) $Ti_{0.99}I_{0.01}O_2$	C	3.36	10.59
	Ti	56.61	27.98
	O	39.32	61.27
	I	0.71	0.16
(b) $Ti_{0.98}I_{0.02}O_2$	C	3.48	10.57
	Ti	61.57	32.62
	O	33.17	56.43
	I	1.78	0.38
(c) $Ti_{0.97}I_{0.03}O_2$	C	4.26	11.32
	Ti	65.79	38.50
	O	27.83	49.45
	I	2.12	0.73
(d) $Ti_{0.96}I_{0.04}O_2$	C	3.94	10.13
	Ti	62.54	35.03
	O	29.62	53.21
	I	3.90	1.63
(e) $Ti_{0.95}I_{0.05}O_2$	C	3.42	11.25
	Ti	58.04	31.13
	O	35.01	55.69
	I	3.53	1.93
(f) $Ti_{0.94}I_{0.06}O_2$	C	3.76	10.62
	Ti	61.59	29.83
	O	30.12	57.21
	I	4.53	2.34
(g) $Ti_{0.93}I_{0.07}O_2$	C	4.12	10.41
	Ti	65.19	36.40
	O	26.42	50.48
	I	4.27	2.71
(h) $Ti_{0.92}I_{0.08}O_2$	C	4.04	10.17
	Ti	63.24	29.02
	O	27.05	57.19
	I	5.67	3.62
(i) $Ti_{0.91}I_{0.09}O_2$	C	3.68	10.54
	Ti	58.52	25.27
	O	30.69	59.54
	I	7.11	4.65
(j) $Ti_{0.90}I_{0.10}O_2$	C	4.10	10.25
	Ti	56.34	27.40
	O	31.37	56.11
	I	8.19	6.24

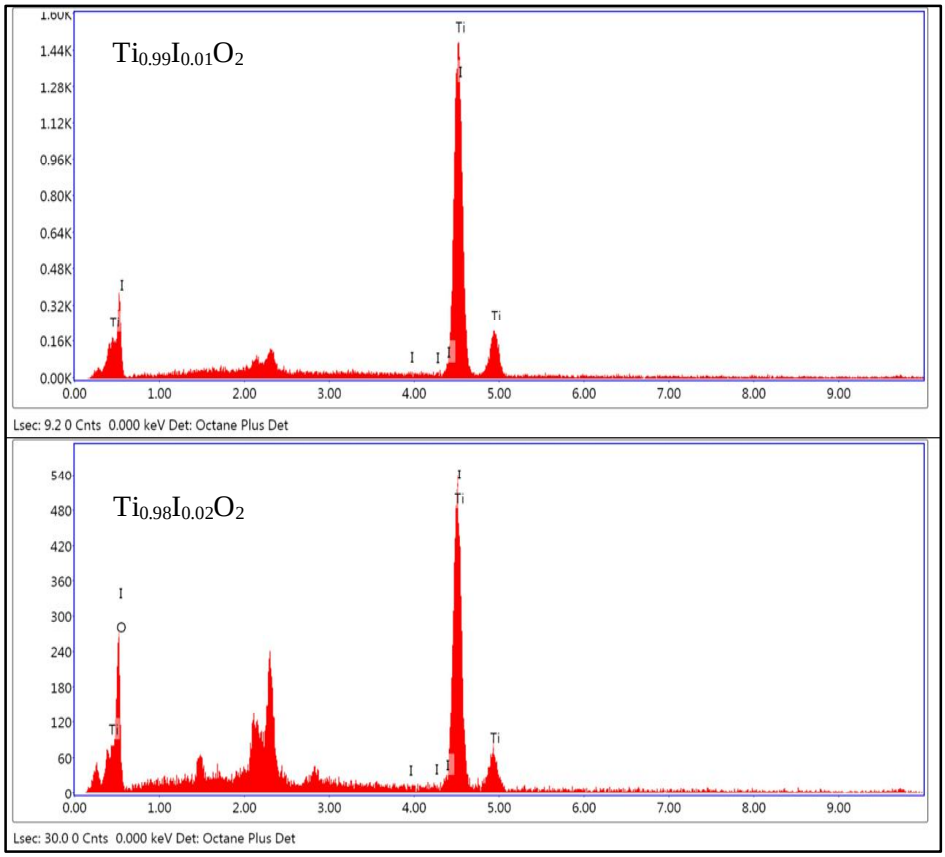
Ti0.99I0.01O2
1.44K
1.28K
1.12K
0.96K
0.80K
0.64K
0.48K
0.32K
0.16K
0.00K
0.00 1.00 2.00 3.00 4.00 5.00 6.00 7.00 8.00 9.00
Lsec: 9.2 0 Cnts 0.000 keV Det: Octane Plus Det
Ti0.98I0.02O2
540
480
420
360
300
240
180
120
60
0
0.00 1.00 2.00 3.00 4.00 5.00 6.00 7.00 8.00 9.00
Lsec: 30.0 0 Cnts 0.000 keV Det: Octane Plus Det

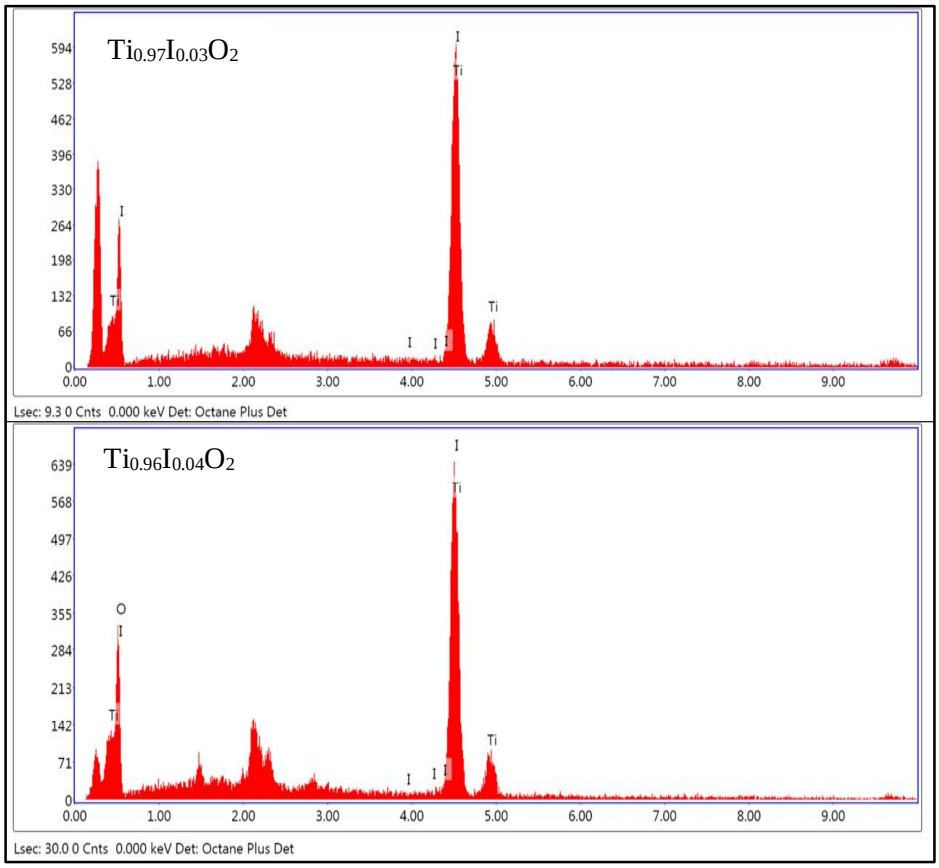
Ti0.97I0.03O2
594
528
462
396
330
264
198
132
66
0
0.00 1.00 2.00 3.00 4.00 5.00 6.00 7.00 8.00 9.00
Lsec: 9.3 0 Cnts 0.000 keV Det: Octane Plus Det
Ti0.96I0.04O2
639
568
497
426
355
284
213
142
71
0
0.00 1.00 2.00 3.00 4.00 5.00 6.00 7.00 8.00 9.00
Lsec: 30.0 0 Cnts 0.000 keV Det: Octane Plus Det

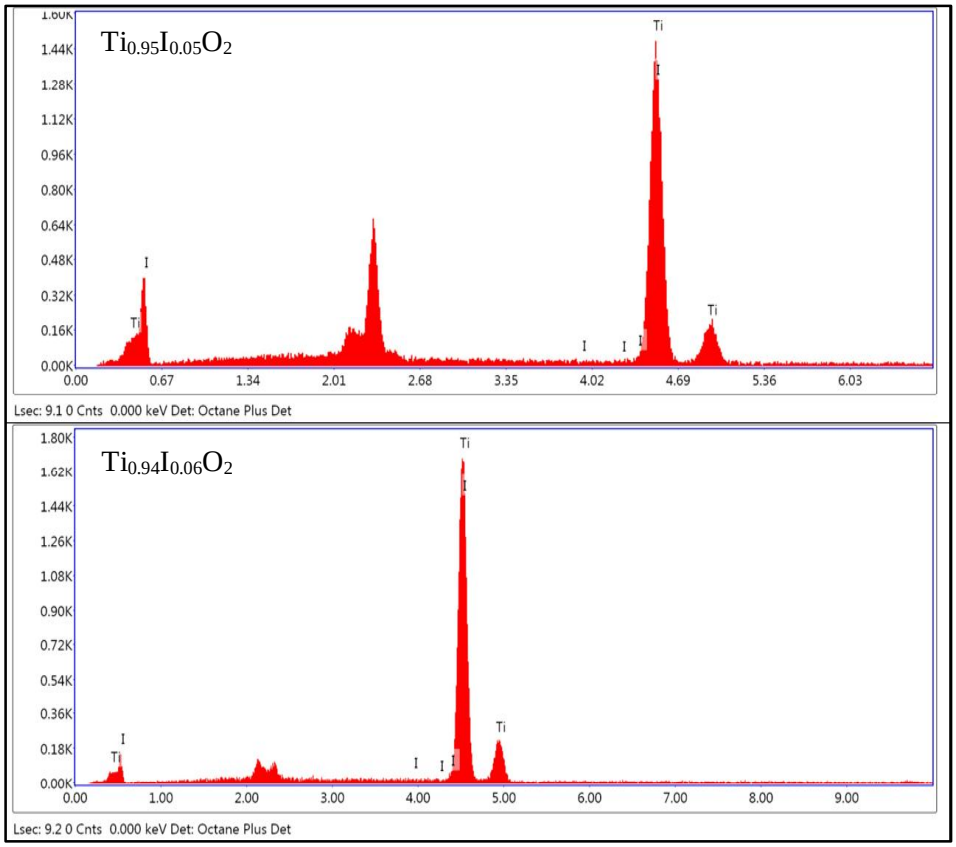
Ti0.95I0.05O2
Lsec: 9.1 0 Cnts 0.000 keV Det: Octane Plus Det
Ti0.94I0.06O2
Lsec: 9.2 0 Cnts 0.000 keV Det: Octane Plus Det

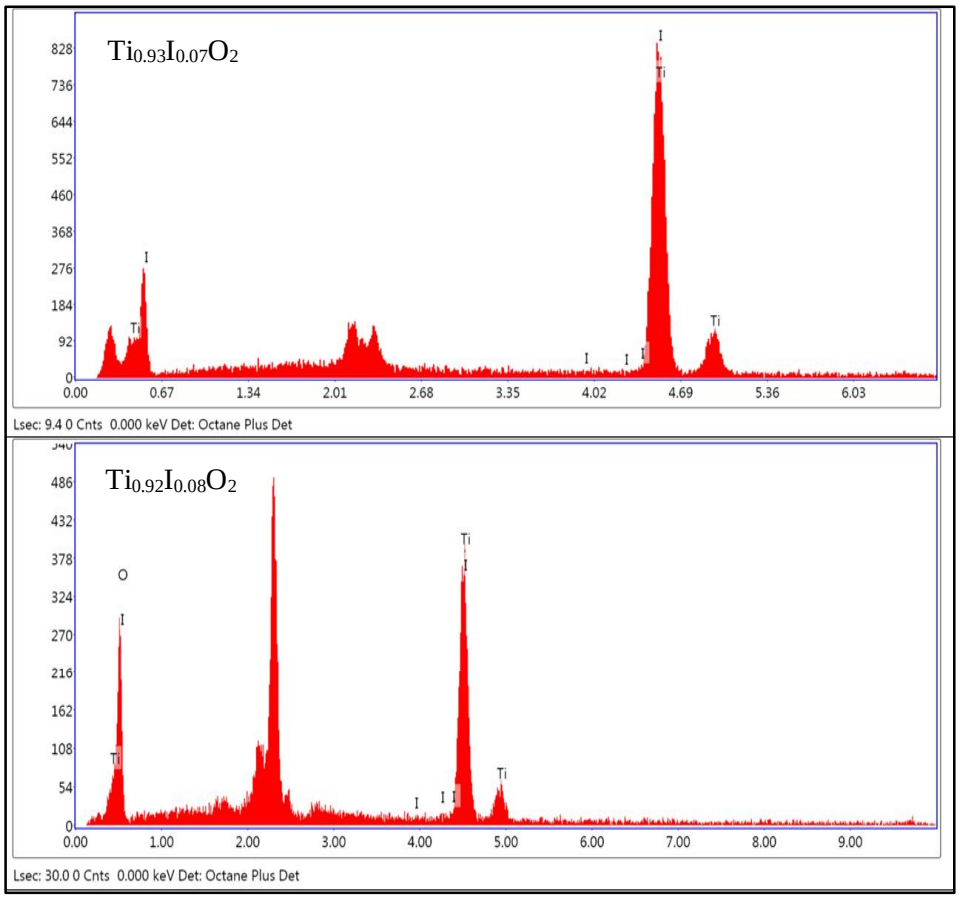
Ti0.93I0.07O2
Lsec: 9.4 0 Cnts 0.000 keV Det: Octane Plus Det
Ti0.92I0.08O2
Lsec: 30.0 0 Cnts 0.000 keV Det: Octane Plus Det

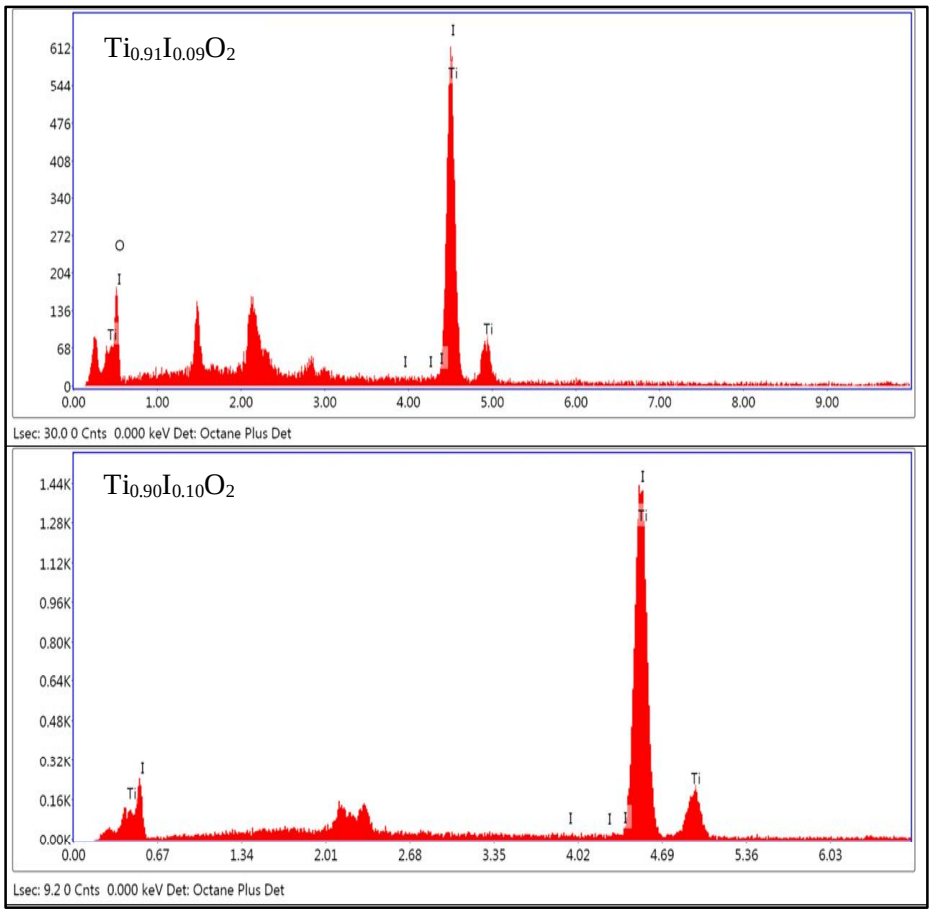

Fig 4.37 EDX analysis of (1-10%) I doped TiO_2 photocatalyst.

4.10 Mechanism of TiO_2 photocatalyst and enhancement of its activity by I doping

The photocatalytic activities of I doped TiO_2 photocatalysts were evaluated in terms of dye degradation in the both types of reactors under their respective light. The dye was degraded by the synthesized photocatalysts in given period of time. The mechanism behind the photodegradation of dye and the role of iodine in photocatalysis process can represented by the equations (4.2-4.10) (Su et al. 2008; Bagwasi et al. 2012; Eskandarloo et al. 2015). The doping of iodine in TiO_2 forms $IO_4^-/IO_3^-/I^-$ species in TiO_2. These species have a significant role in enhancement of photocatalytic activity of TiO_2 since IO_4^- and IO_3^- intermediates form highly reactive $IO_3^{\bullet}$ and $IO_4^{\bullet}$ radicals which are responsible for oxidation of dye. The

presence of other iodine state (I^{5+}) in synthesized photocatalysts as confirmed in XPS analysis indicates the separation of electron-hole pairs and inhibition of their fast recombination since I^{5+} acts as electron acceptors. The generated holes can combine directly with surface adsorbed hydroxyl group that results the formation of $OH^{\bullet}$ radicals which also plays a key role in photodegradation of the dye. A pictorial representation of dye degradation mechanism by synthesized I doped TiO_2 photocatalysts is shown in Fig 4.38.

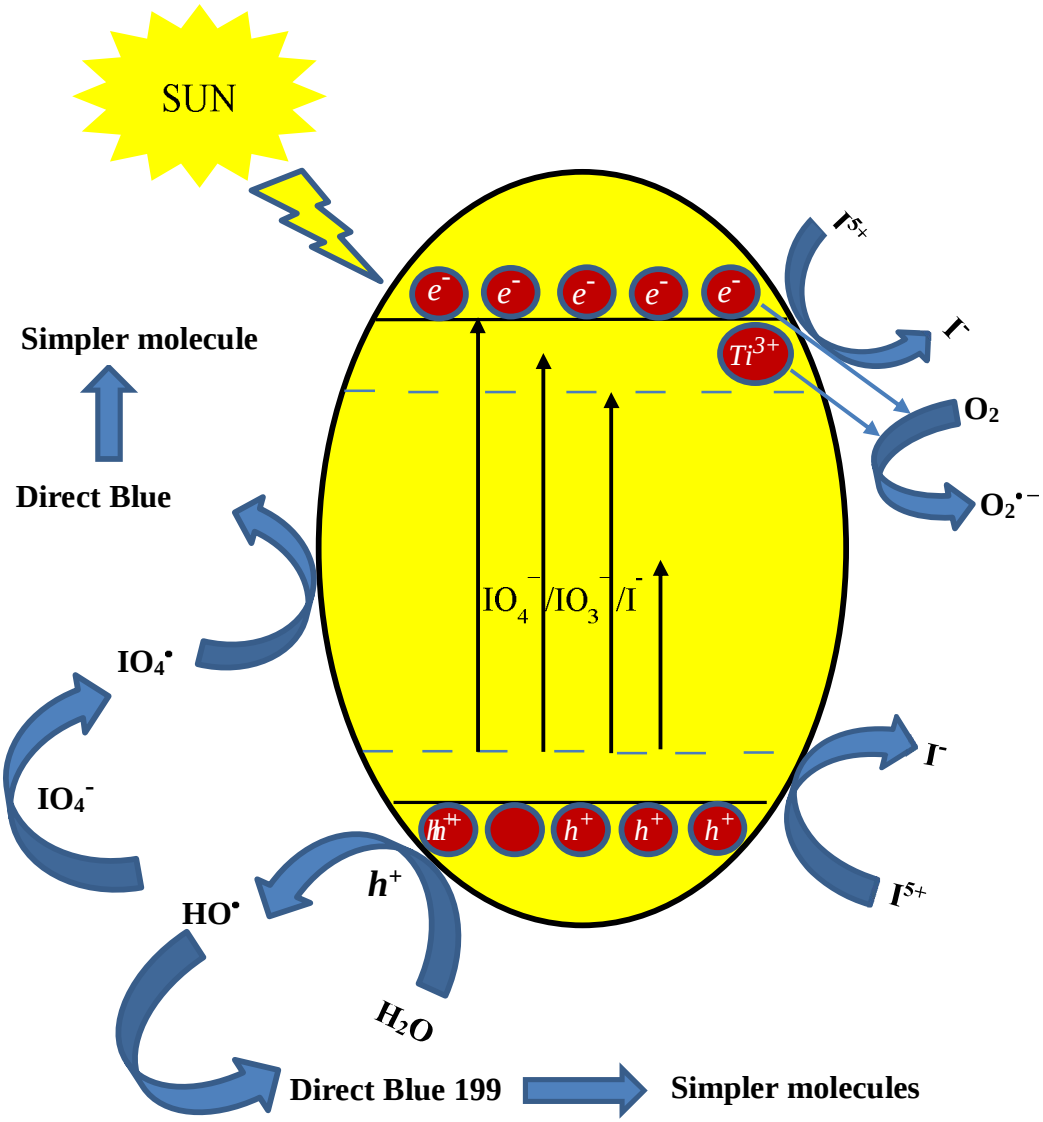

Fig 4.38 Pictorial representation of dye degradation mechanism by synthesized I doped TiO_2 photocatalysts.

$$IO_3^- + \text{heat} \rightarrow HIO_3 \quad (4.2)$$

$$2HIO_3 + \text{heat} \rightarrow I_2O_5 + H_2O \quad (4.3)$$

$$I_2O_5 + H_2O + O_2 \rightarrow 2HIO_4 \quad (4.4)$$

$$HIO_4 \rightarrow IO_4^- + H^+ \quad (4.5)$$

$$IO_4^- + \text{UV light} \rightarrow IO_3^{\bullet} + O^{\bullet -} \quad (4.6)$$

$$O^{\bullet -} + H^+ \rightarrow OH^{\bullet} \quad (4.7)$$

$$OH^{\bullet} + IO_4^- \rightarrow OH^- + IO_4^{\bullet} \quad (4.8)$$

$$OH^{\bullet} + \text{Pollutant} \rightarrow \text{Product} + H_2O + O_2 \quad (4.9)$$

$$IO_4^{\bullet} + \text{Pollutant} \rightarrow \text{Product} + H_2O + O_2 \quad (4.10)$$

Above reactions indicates that the formation of highly reactive radicals ($O^{\bullet -}$, $OH^{\bullet}$, $IO_3^{\bullet}$ and $IO_4^{\bullet}$) and non-radical intermediates (IO_4^- and IO_3^-) responsible for the degradation of dye (Direct Blue 199).

4.11 FTIR analysis of degraded simulated solution/wastewater by I doped TiO_2 photocatalysts

FTIR spectrum of photodegraded industrial wastewater by $Ti_{0.97}I_{0.03}O_2$ photocatalyst is shown in Fig 4.39. The peak at 3492.23 cm^{-1} represent the -NH-NH_2- stretch while the peaks at 1592.36 and 1138.63 cm^{-1} confirm the remaining amount of –SO_3Na- after the degradation of the dye. The absorption peak at 1395.52 cm^{-1} represents the C-H deformation. The peaks of -N=N- stretch (1577.6 cm^{-1}), C-H stretch (2945.4 cm^{-1}), –SO_3Na- (617.8 cm^{-1}) and Cu-N stretch (as discussed in section 4.1) are eliminated from the wastewater and converted into the simpler compound such as H_2O, CO_2, SO_2 and CuO etc.

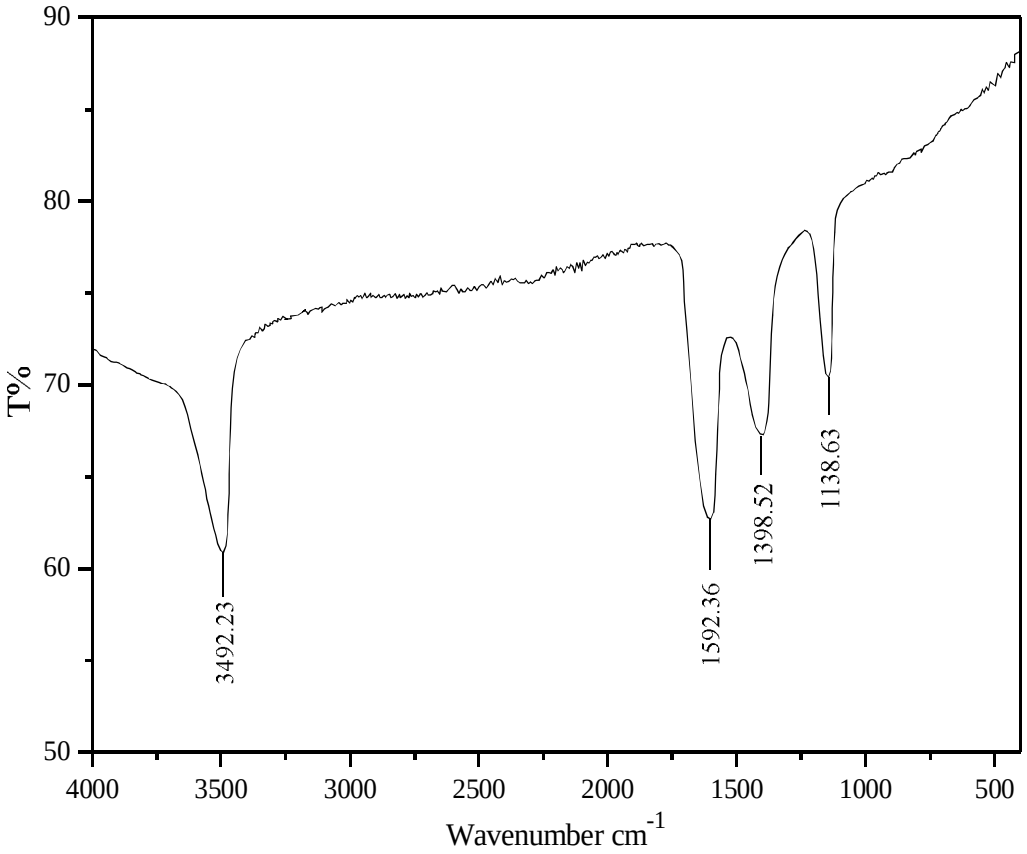

Fig. 4.39 FTIR analysis of treated industrial wastewater.

4.12 Kinetic Study of dye degradation with I doped TiO_2 photocatalysts

The adsorption studies which was done before the kinetic studies show that only 3-3.5% of the dye was adsorbed on the photocatalysts while the self-degradation study of dye shows negligible amount of dye was degraded in both kind of reactors.

The data obtained from the kinetic studies (Table B34-B63) of all the thirty systems (system 34 - system 63) were fitted well with pseudo-first-order kinetics (equation 4.1) and one of them (system 46) shown in Fig 4.40.

$$-\frac{dC}{dt} = K_{app}C \qquad (4.1)$$

Where, C = the concentration of the dye at any time t and K_{app} = apparent first-order rate constant. The rate constant (K_{app}) for each system were evaluated from $-\ln(C/C_o)$ vs. t plot and given in Table C4-C7. The $Ti_{0.97}I_{0.03}O_2$ photocatalyst has shown highest rate constant (8.61×10^{-2} min^{-1}) for system 46 among all the systems. The kinetic data of photodegradation of other dye like Orange II (Štengl and Grygar 2011), Rhodamine B (Barkul et al. 2017), Methylene blue (Wang et al. 2011c; Liu et al. 2006) with I doped TiO_2 photocatalyst also followed the pseudo-first order kinetics.

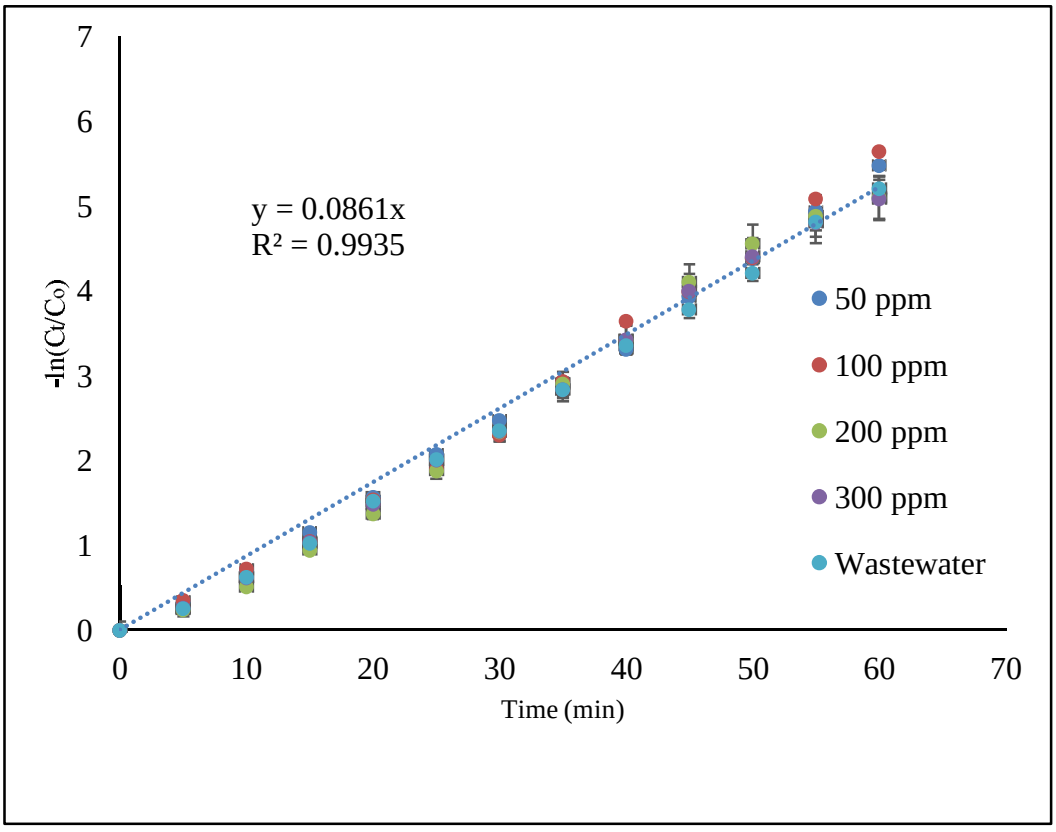

Fig 4.40. Kinetic study of dye degradation for system 46.

The dye degradation results in Table C4-C7 shows that the activity of catalysts (I doped TiO_2) is better at lower concentration (1-3%) of doping than higher concentration (4-10%) systems (37-43), (47-53) and (57-63) system. The

generation of recombination center and/or shielding of TiO_2 surface from light irradiation at higher doping concentration can be the possible reason behind the activity reduction (Zhang et al. 2011). The $Ti_{0.97}I_{0.03}O_2$ catalyst had the best activity among all the synthesized photocatalysts since at 3% of iodine doping in TiO_2, the trapping of electrons and inhibition of e^-/h^+ pair recombination was maximum. The studies about optimal doping concentration are reported previously for metal and non-metal doped TiO_2 (Li et al. 2010; Song et al. 2010; Bagwasi et al. 2012; Zhang et al. 2011).

4.13 Activity of used photocatalysts without regeneration:

The photocatalyst without regeneration shows very less activity as compared to the regenerated photocatalyst. The photocatalyst without regeneration shows only 6.85% of dye degradation ability, which in not significant for photocatalysis purpose.

4.14 Activity of regenerated photocatalysts

The activity of regenerated $Ti_{0.97}I_{0.3}O_2$ catalyst was evaluated by degradation of the dye in industrial wastewater in photochemical reactor and results are shown in Fig 4.41. A decrement in activity of photocatalysts was noticed with number of regeneration (Fig 4.41). The degraded dye residue and adsorbed dye on the catalysts surface can be the main cause behind the activity decrement since in molecular structure of dye, copper was present which form CuO during the degradation of dye that occupy the pore of catalysts particles and decreases their activity. The XRD analysis of regenerated catalysts supports the existence of CuO peak at (35.1) 2θ angle and validate the above statement (Fig 4.42). At same 2θ value, copper oxide peak was reported (Yang et al. 2015; Sahu and Biswas 2011).

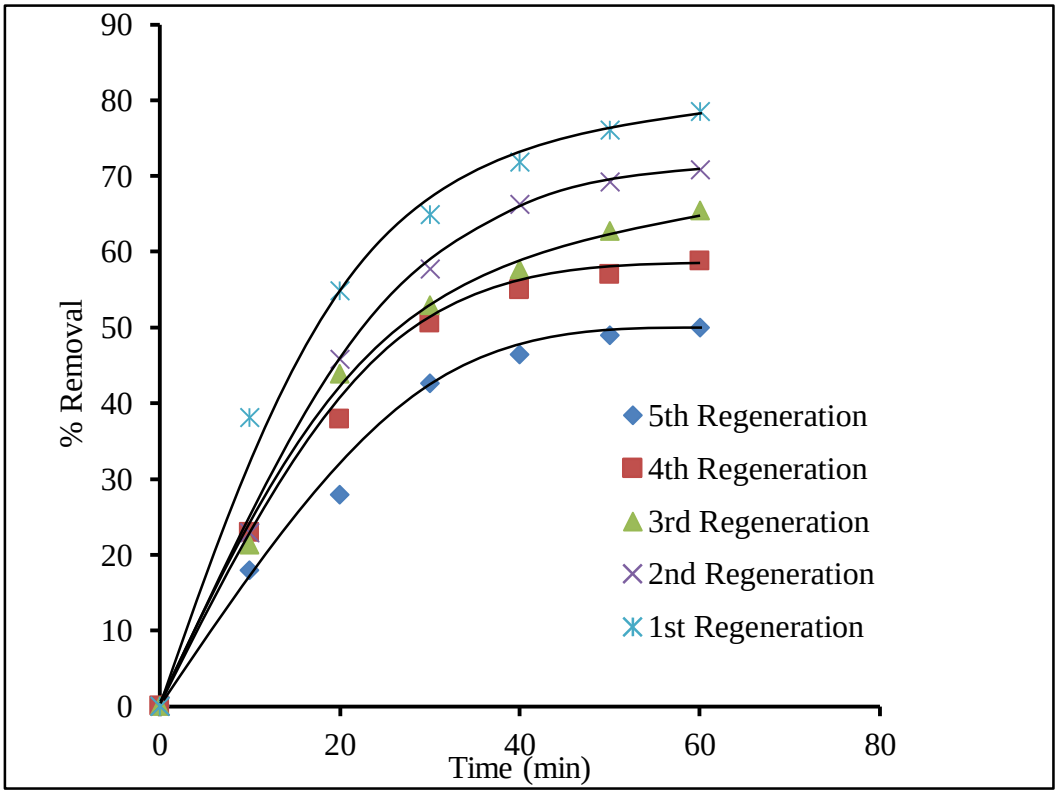

Fig 4.41. Performance of regenerated $Ti_{0.96}I_{0.03}O_2$ photocatalyst for photodegradation of wastewater.

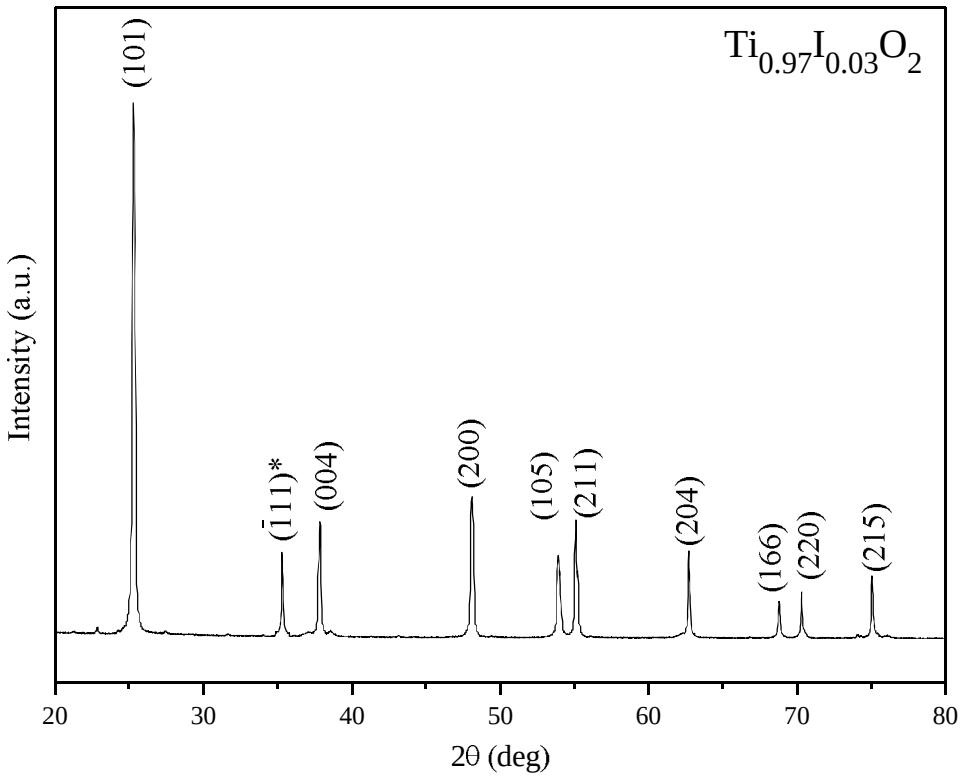

Fig 4.42. XRD spectra of the regenerated $Ti_{0.97}I_{0.03}O_2$ photocatalyst.

The degradation of dye in wastewater in photochemical reactor (with quartz tube) with regenerated $Ti_{0.97}I_{0.03}O_2$ catalysts is shown in Fig 4.43. In Fig 4.43, R_1 is the regeneration of catalyst first time, R_2 is the regeneration 2nd time after use of R_1 and similarly, R_n (n = 3, 4 and 5) is the regeneration the same catalyst n^{th} time. The degradation of the dye by best catalysts ($Ti_{0.97}I_{0.03}O_2$) was done in photochemical reactor and shown in Fig 4.43.

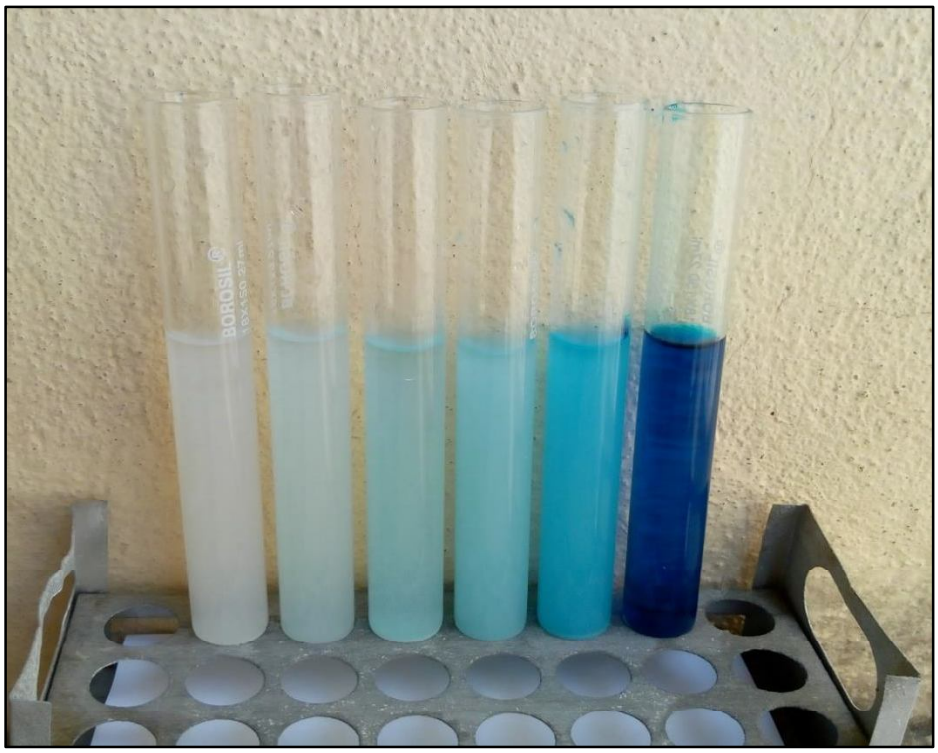

Fig 4.43. Digital Coloured pictures are proving the photodegradation of wastewater (Direct Blue 199) in the photochemical reactor in quartz tube using regenerated $Ti_{0.97}I_{0.03}O_2$ photocatalyst.

4.15 Comparative study among the undoped, I doped TiO_2 and Aeroxide P-25 photocatalysts

Fig 4.44 shows the comparison among the synthesized catalysts i.e. undoped TiO_2, $Ti_{0.97}I_{0.03}O_2$ and Aeroxide P-25 for best catalytic activity in terms of dye degradation in industrial wastewater. As shown in Fig 4.44, the $Ti_{0.97}I_{0.03}O_2$ photocatalyst has the better photocatalytic activity among all the three.

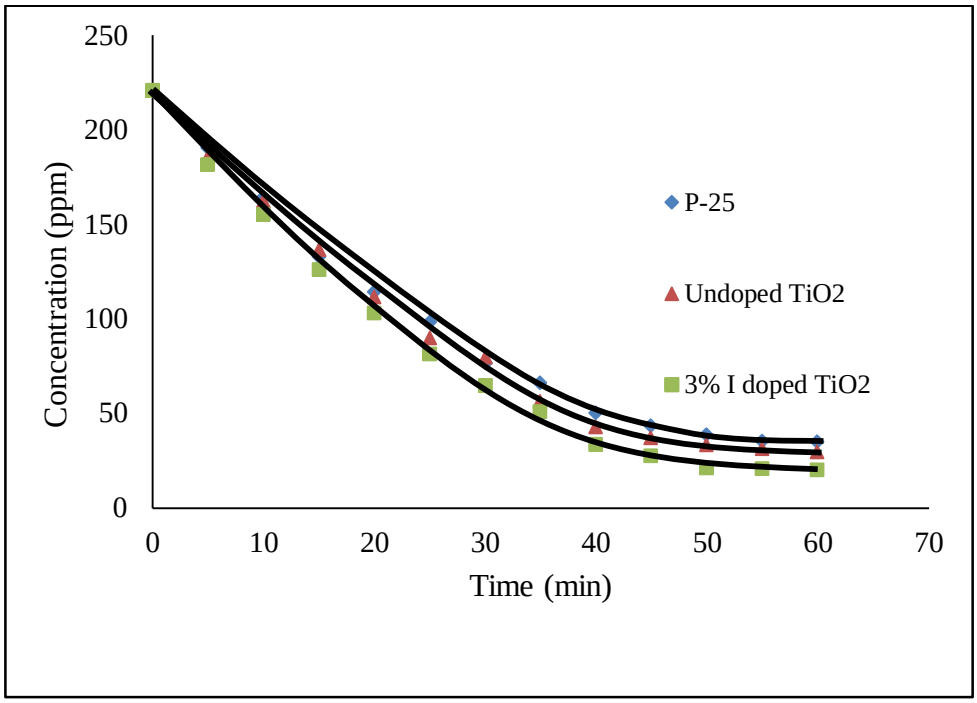

Fig 4.44. Comparison for best photocatalyst among synthesized undoped TiO_2, $Ti_{0.97}I_{0.03}O_2$ and P-25 for photodegradation of industrial wastewater.

4.16 Concluding remarks

Cations and anion doped TiO_2 photocatalysts were synthesized successfully by sol-gel method. In cations doping, the maximum photocatalytic activity among the (1-10%) Fe doped TiO_2 photocatalysts was observed at 4% of Fe doping in TiO_2 while in anion doping it was observed at 3% of I doping in TiO_2. The dye degradation process by both synthesized photocatalysts (Fe doped TiO_2 and I doped TiO_2) follow pseudo-first order kinetics and approximately 80% of dye was degraded in first half an hour in UV photochemical reactor while it took 2 h in open pan reactor. The photodegradation rate of dye was higher in UV photochemical reactor than open pan reactor. Kinetic studies with regenerated photocatalysts reveals that the activity of catalysts decreases with number of regeneration.